Università degli Studi di Cagliari

PHD DEGREE

ELECTRONIC AND COMPUTER ENGINEERING

Cycle XXXIII

TITLE OF THE PHD THESIS

INTEGRATED ELECTRONICS FOR MOLECULAR BIOSENSING

Scientific Disciplinary Sector(s)

ING-INF/01 ELETTRONICA

PhD Student: STEFANO SONEDDA

Supervisor MASSIMO BARBARO

Final exam. Academic Year 2019 – 2020

Thesis defence: March 2021 Session

University of Cagliari

Faculty of engineering

PhD Program in Electronic and Computer Engineering

Integrated Electronics for Molecular Biosensing

Stefano Sonedda

Supervisor:
Prof. Massimo Barbaro

REGIONE AUTÒNOMA DE SARDIGNA
REGIONE AUTONOMA DELLA SARDEGNA

Abstract

This work focuses on different approaches to sense the presence and activity of a specific analyte by using integrated electronic platforms. The first integrated platform here presented has been designed to detect the enzyme telomerase. Telomerase causes the elongation of telomeres, which are part of the chromosomes, and determines the lifespan of cells. Telomerase expression is a marker of malignity in tumoral cells and its evaluation can be exploited for early diagnosis of many types of cancer cells. To detect the telomerase enzyme, a CMOS biosensor based on CMFET (Charge-Modulated Field Effect Transistor) able to measure kinetics of DNA replication and telomerase reaction was developed. The sensor can be functionalized by immobilizing single strands of DNA that contain the telomeric sequence, used as probes. If telomerase is present, the probes will be elongated by the enzyme and the charge on the sensing area will change, which reflects in a variation of the output current or voltage. The chip includes three different readout schemes (voltage, current- and time-based), each of which has different measuring ranges and operating conditions. The measured data is then digitized, stored, and can be sent off-chip through SPI (Serial Peripheral Interface) protocol. A total of 1024 biosensors have been integrated in a single chip with a size of 10x10mm^2. Each sensor can be independently addressed and functionalized by an electrochemical procedure using an integrated potentiostat, thus requiring no external equipment.

The second part of this work rises from the idea that bacteria, like Escherichia coli, can detect analytes in solution even at extremely low concentrations and change their movement through a process called chemotaxis, to move towards chemical gradients in the solution. E. coli moves by rotating its flagella either clockwise (for random tumbles) or counterclockwise (for straight runs, when it senses a chemical it is attracted to). Therefore, observing bacteria flagellar rotation can give enough information on the presence of a specific analyte in the solution. To electronically detect bacteria movement, an active surface covered in electrodes has been designed. By measuring the impedance between each pair of electrodes through an integrated LIA (lock-in amplifier), it is possible to know how a single bacterium is moving. By that, the presence or absence of the analyte can be deduced, thus effectively turning bacteria into chemical sensors. A total of 64 sensing sites have been integrated in a 1.3x1.6mm^2 chip.

Acknowledgements

Stefano Sonedda gratefully acknowledges Sardinian Regional Government for the financial support of his PhD scholarship (P.O.R. Sardegna F.S.E. - Operational Programme of the Autonomous Region of Sardinia, European Social Fund 2014-2020 - Axis III Education and training, Thematic goal 10, Investment Priority 10ii), Specific goal 10.5.

Contents

I CMOS Lab-on-Chip for telomerase activity detection

1 The role of telomerase **1**
- 1.1 DNA replication . . . 1
- 1.2 Telomeres and telomerase . . . 2
- 1.3 Telomerase detection techniques . . . 5
  - 1.3.1 Telomeric repeat amplification protocol . . . 5
  - 1.3.2 Electrochemical and optical biosensors for telomerase activity detection . . . 7
  - 1.3.3 Electronic biosensors for telomerase activity detection . . . 11

2 CMOS Lab-on-Chip for telomerase detection **17**
- 2.1 CMFET . . . 18
  - 2.1.1 CMFET working principle . . . 18
  - 2.1.2 CMFET as a DNA sensor . . . 20
- 2.2 Telomerase activity detection process . . . 22
- 2.3 Chip architecture . . . 24
  - 2.3.1 Sensor array . . . 24
  - 2.3.2 Read-out circuitry . . . 25
  - 2.3.3 Integrated potentiostat . . . 26
  - 2.3.4 Temperature control system . . . 26
  - 2.3.5 Digital logic . . . 26

3 CMFET-based biosensor for telomerase detection **27**
- 3.1 Refining CMFET model for telomerase activity detection . . . 27
  - 3.1.1 Charge variation model . . . 28
  - 3.1.2 Capacitance model . . . 30
- 3.2 CMFET implementation . . . 31
  - 3.2.1 Planar version . . . 31
  - 3.2.2 Circuit-under-pad version . . . 32
  - 3.2.3 Definition of the active pixel . . . 33
- 3.3 Layout design . . . 35
  - 3.3.1 CMFET sensing unit layout design . . . 35
  - 3.3.2 Sensor array . . . 37
- 3.4 Simulation of sensor characterization during telomerase activity . . . 38

4 Readout schemes **43**
4.1 Level shifter . . . 43
4.2 Current reference circuit . . . 46
4.3 Analog-to-digital converter . . . 46
4.4 Current-starved ring oscillator . . . 47
4.5 Temperature sensor . . . 49
4.6 Potentiostat . . . 50
4.6.1 Self-calibrating current mirror . . . 51
4.7 Results . . . 54

II Bacterial sensing **58**

5 Bacterial biosensing **59**
5.1 A slower response: transcription . . . 59
5.2 A fater response: chemotaxis . . . 60
5.2.1 Bacterial flagellar motor . . . 61
5.2.2 Chemoreceptors and signaling pathway . . . 62
5.3 Methods for assaying bacterial chemotaxis . . . 63
5.3.1 Capillary assay . . . 64
5.3.2 Microfluidic assay . . . 64
5.3.3 Tethered cells assay . . . 65

6 Electronic bacteria flagellar motor detection **67**
6.1 BFM sensing . . . 67
6.1.1 Electrochemical impedance measurements . . . 68
6.1.2 Impedance measurement principle . . . 70
6.2 System architecture . . . 72
6.3 Electrochemical cell design . . . 73
6.4 Electronic front-end . . . 76
6.4.1 Transimpedance amplifier . . . 76
6.4.2 Lock-in amplifier . . . 78
6.5 Results . . . 80

7 Conclusions **85**

List of Figures

1.1.1 Double helix DNA structure 1
1.1.2 Replication fork and DNA polymerase activity 2
1.2.1 Telomere structure and location in a chromosome. 3
1.2.2 Telomerase activity process. 4
1.3.1 Scheme for TRAP assay. 6
1.3.2 Electrochemical cell and potentiostat. 8
1.3.3 Randles circuit schematic. 8
1.3.4 Comparison of current increase for different types of samples with ECTA. 10
1.3.5 Two different silicon nanowires modified with different antibody receptors. 12
1.3.6 qPCR Lab-on-chip implementation. 14
1.3.7 Flow cytometry device 15

2.0.1 MOSFET vs ISFET 18
2.1.1 CMFET structure as presented in [50] 19
2.1.2 A microphotograph of the chip. 21
2.1.3 Threshold voltage variation in [54] 23
2.3.1 A block diagram of the chip architecture. 25

3.1.1 A basic schematic of the sensor with an NMOS-PMOS pair. 28
3.1.2 A schematic of the sensor that includes parasitic capacitances. 30
3.2.1 Section of planar CMFET structure (NMOS). 32
3.2.2 Section of circuit-under-pad CMFET structure (NMOS). 33
3.3.1 Standard planar version of the CMFET layout. 36
3.3.2 Circuit-under-pad version of the CMFET sensor with a $25\,\mu m \times 25\,\mu m$ capacitor. 37
3.3.3 Sensor with DMOS for potentiostat usage. 38
3.3.4 Cluster layout. 39
3.3.5 Layout of the complete chip. 41
3.4.1 Effective threshold voltage variation as a function of telomerase efficiency β 42
3.4.2 ΔV_{TH} induced by telomeres elongation. 42

4.1.1 Schematic of the N-type level shifter. 44
4.1.2 Level shifter output for both NMOS and PMOS, with $V_{FG} = 0.9\,V$. . 45

4.1.3 Level shifter output for both NMOS and PMOS, with $V_{FG} = 0\,\mathrm{V}$ and $V_{FG} = 1.8\,\mathrm{V}$ respectively. . . . 45
4.2.1 Current reference readout scheme. . . . 46
4.3.1 Schematic representation of the implemented dual-slope ADC. . . . 47
4.3.2 Ring oscillator circuit 48
4.4.1 Ring oscillator circuit 49
4.4.2 Simulation of the ring oscillator for different β values. . . . 49
4.5.1 Implemented PTAT circuit and simulation. . . . 50
4.6.1 Implementation of the potentiostat 51
4.6.2 Level-shifted low-voltage cascode current mirror schematic. . . . 52
4.6.3 Schematic of the integrated potentiostat. . . . 53
4.6.4 Schematic of the current comparator. . . . 53
4.6.5 Complete layout of the potentiostat 54
4.6.6 Implemented PTAT circuit and simulation. . . . 56
4.7.1 Chip-level simulation of a data conversion. . . . 57

5.2.1 Chemotaxis in *E. coli*. . . . 60
5.2.2 Flagellar motor schematic representation. . . . 61
5.2.3 The chemoreceptor signaling pathway. . . . 63
5.3.1 Capillary assay. . . . 64
5.3.2 Device for microfluidic chemotaxis assay. . . . 65
5.3.3 Microfluidic device for dual chemical gradient generation. . . . 66

6.1.1 Double-layer structure. . . . 68
6.1.2 Schematic representation of the proposed BFM monitoring principle. 69
6.1.3 Coplanar electrodes equivalent circuit 70
6.1.4 Auto-balancing bridge scheme. . . . 71
6.2.1 Implemented impedance measurement scheme. . . . 72
6.4.1 Current amplifier schematic 77
6.4.2 Two-stages transimpedance amplifier. . . . 78
6.4.3 Lock-in amplifier schematic. . . . 79
6.4.4 Switching mixer schematic. . . . 80
6.4.5 Low-pass filter schematic 81
6.4.6 Low-pass filter cut-off frequency. . . . 82
6.5.1 Layout and photograph of the chip 83
6.5.2 Simulation schematic. . . . 84
6.5.3 Output simulation. . . . 84

List of Tables

3.1 Area occupation for different sensor implementations. 33
3.2 Sensitivities for different control capacitors. 35

4.1 Number of devices on chip 54

6.1 Different electrode types. 73
6.2 Double layer capacitance for different electrode geometries. 73
6.3 Cell constant for different geometries. 75
6.4 R_{sol} variation due to a cell between the electrodes. 75
6.5 R_{sol} variation due to a bead between the electrodes. 76

Introduction

Bioelectronics is the application of electronic engineering principles to biology, chemistry, medicine or health. Biosensors make this union possible: they are analytical devices that convert a biological response into a signal of different type, such as an optical, piezoelectric or electrochemical signal, which can be measured and quantified.

During the last 60 years, the interest in biosensors has quickly risen. In 1956 L. Clark, considered by many "the father of biosensors", presented an oxygen probes which, later, was used to monitor the glucose level in blood [1]. From this first biosensoristic implementation, the field of biosensors found many new approaches based on the innovations introduced in technology. The target of the biosensor detection is called analyte: for example, organic compounds, gases, ions, proteins and bacteria all can be used as analytes. The specific biochemical reactions that takes place can be mediated by isolated enzymes, immunosystems, tissues, organelles or whole cells. Analytes are usually detected by electrical, thermal or optical signals [2]. The main focus of a biosensor can be directed towards detecting the concentration of a specific component or the total composition of the analyte.
A typical biosensor comprises two main elements: a bioreceptor and a transducer. The bioreceptor is a sensitive biological element that interacts with the analyte under test and produces a response measurable by the transducer. Biosensors can be categorized by the chosen receptor. As mentioned before, commonly used biosensors may utilize:

- nuleic acids: biosensors in this category are referred to as genosensors [3, 4]. The recognition process is based on the principle of complementary base pairing, adenine:thymine and cytosine:guanine in DNA. If the target nucleic acid sequence is known, complementary sequences can be synthesized, labeled, and then immobilized on the sensor. The bonding between the analyte and the receptor, which happens due to hybridization, can be detected by both direct and indirect means. Nucleic acid biosensors can detect a wide range of target molecules or complex targets like cells and viruses.

- enzymes, which are popular bioreceptors because they are able to catalyze a number of reaction and are suitable with a wide variety of transduction methods. Enzymes also allow a lower limit of detection compared to other binding techniques [5, 6].

- antibodies, which give rise to immunosensors. They utilize the capability of antibodies to bind to a very specific compound or antigen, creating an antigen-

antibody complex. A signal is then generated when the binding event happen. Immunosensors are known to be highly sensitive and can detect nanomolar to femtomolar concentrations of biomolecules [7, 8].

- cells, which are often used as bioreceptors because they are sensitive to surrounding environment and they can respond to all kinds of stimulants [9, 10]. Moreover, complex immobilization techniques are not required since they tend to attach to the surface. Thanks to technologies based on synthetic biology, microorganisms can also be programmed with specific signal outputs, sensitivity, and selectivity.

Moreover, the biosensor needs a transducer, or detector element, which converts the response of the interaction between analyte and receptor into a different type of signal that can be easily measured.
Depending on the type of transducer, biosensor can fall into different categories:

- electrochemical sensors, based on reactions that produce or consume electrons (redox), which often use electrodes of different materials and utilize a transducer that can detect variations in current, potential, conductivity or impedance;

- optical sensors, which detect changes in light absorption between reagents and products of a specific reaction or the light output of a luminescent process. These sensors commonly employ photodiodes to measure light variations;

- gravimetric and piezoelectric sensors, which can measure variation in mass or elastic deformations in response to a biological process;

- electronic sensors, which make use of field effect transistors and are capable of detecting biological process characteristics through variation in voltages or currents across the transistor channel.

This thesis focuses on the design of electronic biosensors in CMOS technology, which make use of different receptors (respectively nucleic acids and bacteria). CMOS (Complementary Metal–Oxide–Semiconductor) is the most common MOSFET (Metal–Oxide–Semiconductor Field-Effect Transistor) fabrication technology and it can offer an important advantage in biosciences: the low cost and large-scale integration allow to design complete systems in a small area. For example, electrodes can be fabricated with similar or smaller size as cells or bacteria, and all the necessary instrumentation (i.e. transducers, amplifiers, filters, converters...) can be fitted inside a single chip. Moreover, electrical signals are easy to measure compared to other biosensor transducer outputs.
The first part of this work concerns the development of a LoC (Lab-on-a-Chip) for telomerase activity detection. In the first chapter an overview on telomeres and telomerase is given, together with the analysis of some existing techniques to perform telomerase detection. The proposed LoC working principle and architecture are presented in the second chapter, while a more detailed view on the sensor's design is given in the third chapter. The fourth chapter finally describes the readout schemes and presents some results.

The second part of this work focuses on the development of a biosensor for bacterial flagellar motor detection. After a brief description of bacteria sensing mechanisms, some common assays are presented in the fifth chapter. The sixth chapter shows the CMOS chip design process, from the modeling of the electrodes to the design of the analog read-out schemes. Finally, the last chapter presents some conclusions and future outlooks.

Part I

CMOS Lab-on-Chip for telomerase activity detection

1 | The role of telomerase

1.1 DNA replication

Nucleic acid are large biomolecules whose purpose is to carry all the genetic information of all living organisms and viruses. Deoxyribonucleic acid (DNA), when hybridized, is often found in the shape of a double helix composed of two strands of biopolymers, called polynucleotides. Each strand is composed of a base unit, a monomer called *"nucleotide"*, which comprises three subunits: a nitrogenous base - adenine (A), guanine (G), thymine (T), cytosine (C) -, a five-carbon sugar and at least one phosphate group. DNA contains the biological and genetic information encoded in the sequence of nucleobases.
The backbone of the DNA strand is made of alternate phosphate and sugar residues, bonded asymmetrically. This causes the DNA strands to have a direction, which is anti-parallel in a double helix. The asymmetric ends of the strands can have a directionality of 5' (five prime) if there is a terminal phosphate group or 3' (three prime) if there is terminal a hydroxyl group, as displayed in Fig. 1.1.1.

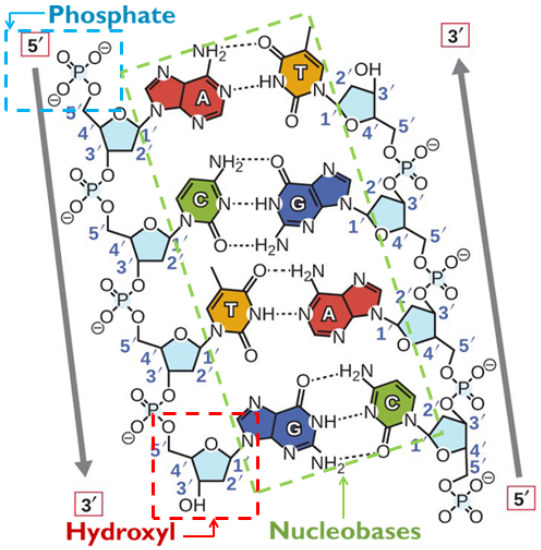

Figure 1.1.1: Double helix DNA structure. By numbering the carbons (1 through 5) in each sugar molecule, the direction of each strand is identified . The 5' end is found where carbon no. 5 is not bound to another nucleotide; the 3' end is found where carbon no. 3 is not bound to another nucleotide.

DNA replication is carried out by DNA polymerases, a family of enzymes.

Usually the replication process can't generate a new DNA strand, but can only extend already existing strands. To start the DNA replication, the complementary strands that compose the double helix need to be separated into two single strands, creating a structure called "replication fork".
Directionality has an impact during DNA replication, because DNA polymerase can synthesize DNA only toward one direction, by adding nucleotides to the 3' end of the strand. As shown in Fig. 1.1.2, the two strands at the replication fork have opposite direction. Polymerase will extend continuously the strand being synthesized in the same direction as the growing replication fork, while the replication of the opposite strand will be slower and more complex. The former is called leading strand, the latter the lagging strand. In the lagging strand, a short complementary primer of RNA is synthesized first. RNA (ribonucleic acid) structure is more often found as a single-strand and utilizes a different nitrogenous base than DNA, uracil (U), in place of thymine. RNA is involved in protein synthesis, DNA replication and gene regulation.
After the RNA primer synthesis, a DNA polymerase extends the primer giving rise to Okazaki fragments [11].
Finally, the RNA primers are replaced with DNA and all the fragments are bound together by DNA ligase.

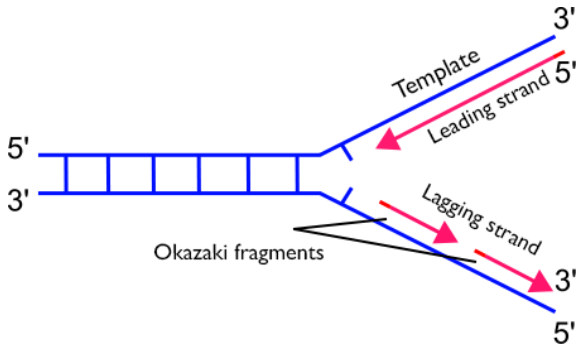

Figure 1.1.2: Replication fork and DNA polymerase activity

In order to replace RNA with DNA, DNA ligase needs another DNA strand in front of the RNA primer. This happens everywhere during the replication, with the exception of the last RNA segment, that eventually gets eliminated. Hence, during each replication, the terminal part of a chromosome is lost. To prevent any damage caused by replication, the terminal part is constituted of noncoding DNA sequences called *"telomeres"*.

1.2 Telomeres and telomerase

In eukaryotic organisms, during cell division each DNA molecule is tightly packed with histone proteins into a thread-like structure called chromosome, which are passed down from parent to offspring. A telomere is the terminal region of each chromosome, which protects the chromosome itself from deterioration or fusion with neighbouring chromosomes. In particular, chromosome fusion can lead to the

translocation of genetic material between non-homologous chromosomes, resulting in carcinogenesis.

The existence of telomeres was first hypothesized by Barbara McClintock in 1933 and the term "telomere" were first used by Hermann Muller in 1938. Blackburn, Greider and Szostak, with their studies starting in the '80s, won Nobel Prize in 2009 by explaining the working principles of telomeres and telomerase [12, 13, 14].

Telomeres are made of repetitive nucleotides sequences. In vertebrates telomeres are constituted of the TTAGGG sequence, repeated about 2,500 times in humans.

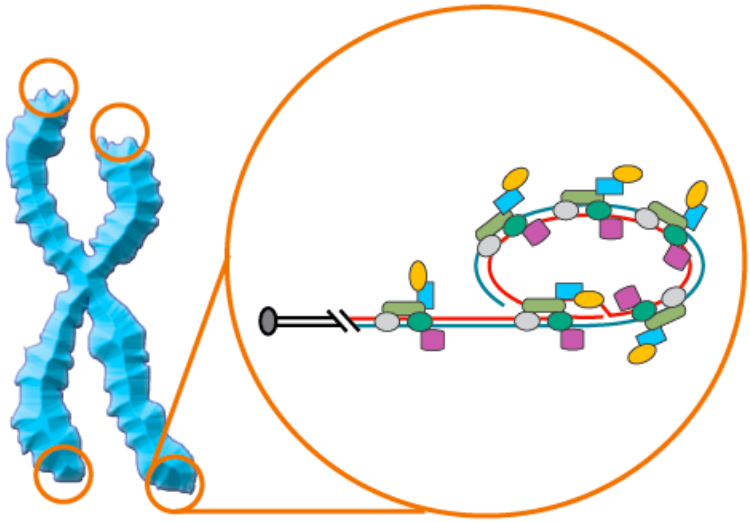

Figure 1.2.1: Telomere structure and location in a chromosome.

The DNA replication is not able to reach the extreme 3' end of the chromosome, but ends in the telomere region. Thus, at each replication, the telomere region of the new DNA strand will be shortened. This process causes the cell to have a limited number of replication, until the telomeres reach a critical length.
In human somatic cells, the number of times a cell can divide is identified with the Hayflick limit [15] and it is believed to be between 50 and 70 cell divisions. Once the telomeres reach their critical length, the cell begins the process of apoptosis, or programmed cell death, to avoid replication errors and prevent DNA mutation. As the telomere is progressively shortened because of the incomplete replication due to the problem related to the lagging strand mentioned above, it can also be elongated by the activity of an enzyme called *"telomerase"*.

Telomerase, also known as terminal transferase, is a ribonucleoprotein that causes the elongation of a telomere. In humans, the telomerase enzyme complex is composed of two molecule each of human telomerase reverse transcriptase (TERT), telomerase RNA (TR or TERC), and dyskerin (DKC1), as shown by Cohen et al. [16]. TERT is a reverse transcriptase (RT), i.e. an enzyme whose purpose is to generate a complementary DNA (cDNA) from an RNA template.
TERT can add the six-nucleotide repeating sequence (5'-TTAGGG) to the 3'

strand of the chromosome, using the telomerase RNA as a complementary template as shown in Fig. 1.2.2 (B). After the bases have been added (C), telomerase shifts forward (D) until is aligned with the ending 3'-telomere and the same process is repeated. Eventually, when the strand is long enough, DNA polymerase can complete the complementary strand, producing double strand DNA.

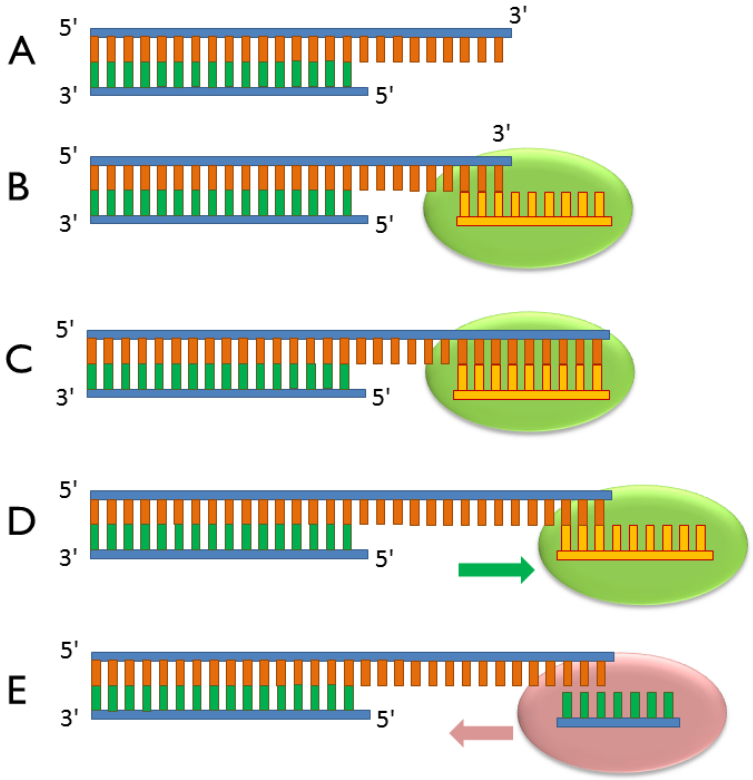

Figure 1.2.2: (A) Telomeres before elongation. (B) Telomerase binds to the 3' end of the telomere. (C) Using RNA as template, complementary bases are added. (D) Telomerase relocates and the process is repeated from (B) again. (E) DNA polymerase completes the lagging strand.

In humans, in normal conditions telomerase expression appears to be limited to germ cells and stem cells; otherwise it is absent from normal somatic tissues [17]. It has been observed that the absence of this enzyme indicates a finite lifespan of the cells, while its presence is bound to an unlimited proliferation, which is a requirement to maintain tumor growth.
Shay and Bacchetti [18] evaluated the role of telomerase in over 3500 human tumors, finding that telomerase activity had been detected in the vast majority of cases. Other studies [19] also show a correlation between the presence of telomerase activity and the onset of tumor and malignant cells and estimate a difference in telomerase activity between mortal and immortal cells of at least 1000 times, strongly supporting the link between telomerase and cancerous cells and suggesting that telomerase detection could lead to diagnostic and therapeutic applications.

In addition to its role in the diagnosis and treatment of cancer, telomerase was demonstrated to play a role in age-related [20, 21] and neurodegenerative diseases [22, 23] as well. In particular, preliminary results seem to confirm the first hypothesis of correlation between the insurgence of these pathologies and a down-regulation of the enzyme [20], suggesting that its catalytic subunit assumes a protective function in adult human brains [23], thus shedding new light on the role of telomerase in this field of research.

1.3 Telomerase detection techniques

Due to the importance of telomerase activity, the development of detection techniques becomes critical. Since the discovery of telomeres and telomerase (the former in the first half of the 20th century, the latter in the second half), great progresses in the study of DNA-related subjects have been made. To allow the analysis of biological processes, the development of appropriate assays is essential. Moreover, as telomerase relevance has quickly risen up in the past two decades, new techniques have been presented and applied, which allowed to achieve higher precision and ease of use compared to the past.

1.3.1 Telomeric repeat amplification protocol

In the early 90s, right after the discovery of telomerase, its activity was measured in vitro by a primer extension assay in which telomerase synthesisez telomeric repeats onto oligonucleotide primers [12]. Previous methods, which extracted telomerase from cells by hypotonic swelling and physical disruption, required up to 10^8 cells to get reliable telomerase extraction.
To increase sensitivity, speed and efficiency of the detection process, Kim et al. [19, 24] developed a polymerase chain reaction (PCR)-base assay called TRAP (telomeric repeat amplification protocol). PCR is a common technique used to amplify a DNA segment and thus generating thousands to millions of copies of a particular DNA sequence.

TRAP assay includes three main steps:

- extension, in which telomerase add telomeric repeats to the substrate;
- amplification, in which the extension products are amplified by PCR. PCR consists on the application of thermal cycles to allow different temperature-dependent reactions, such as DNA melting to obtain single-stranded DNA and enzyme-driven DNA replication. As the reaction progresses, the new copies of DNA generated by PCR are used as primers; this gives start to a chain reaction in which the original DNA primer is exponentially amplified;
- detection, in which, by using gel electrophoresis, the presence or absence of telomerase activity is determined.

Despite being the most common telomerase detection technique, TRAP as all PCR-based methods suffers from amplification related error and there is the possibility that the analyte contains PCR inhibitors, hindering the process. Furthermore, it is complicated to perform and requires electrophoresis to visualize results, so it is not suitable for a fast and easy cancer screening system.
Many variants of TRAP have been developed in the years following TRAP introduction, in order to obtain higher sensitivity, easier evaluation of the results or allow *in situ* analysis [25].

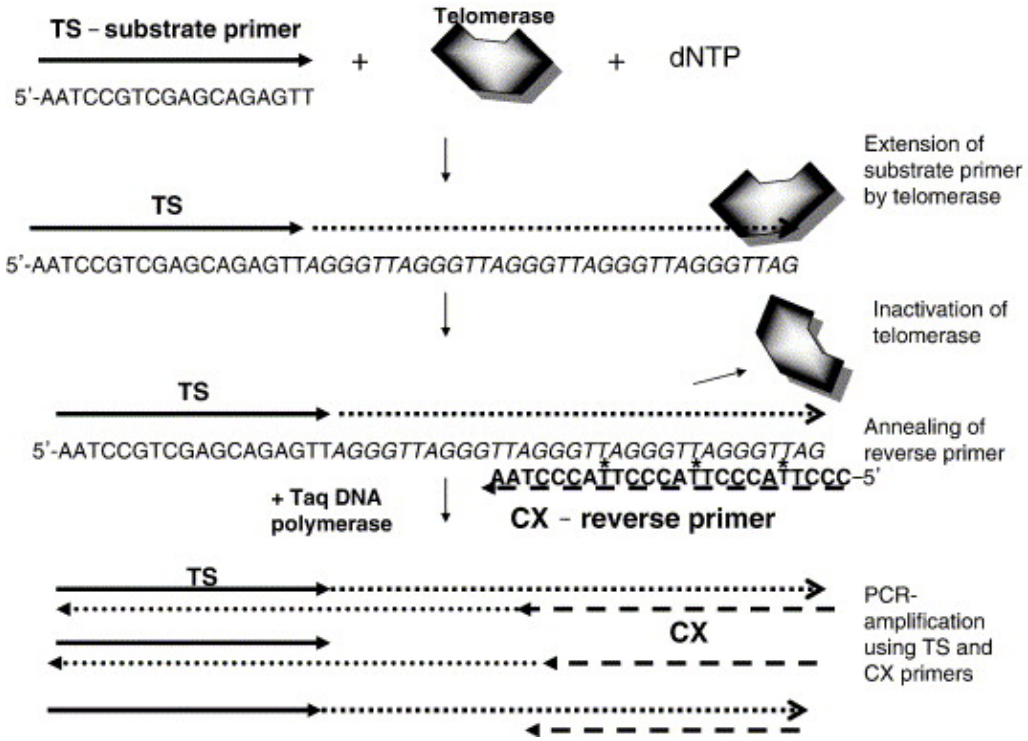

Figure 1.3.1: Scheme for TRAP assay from [25]. Telomerase first extends substrate primer TS on non-telomeric sequence with telomeric repeats. These products are then amplified by PCR using TS and CX primers.

One of the possible modifications of the TRAP assay involves the detection by means of fluorescence instead of the detection through electrophoresis. A technique has been developed [26] which requires the use of primers with energy transfer (amplifluors). Amplifluors are primers characterized by a donor-acceptor pair and emit fluorescence only upon incorporation into PCR products. This method allows the elimination of the post-PCR processing, since the produced fluorescence signal directly correlates to the amount of amplified DNA generated during the PCR.
Another approach to perform TRAP is the scintillation proximity assay (SPA), which helps to increase the rate of detection of telomerase activity. Two elements are fundamental for TRAP-SPA: first, 5'-end biotinylated oligonucleotides are used as primers; moreover, the amplification takes place in presence of tritiated thymidin. Streptavidin-coated fluoromicrospheres, which contain a scintillator that emits in presence of tritium, are added. Biotinylated [^{3}H]-labeled product binds to

the microspheres and generate a signal. Thus, instead of using gel electrophoresis, PCR products are quantified using a scintillation counter. Using TRAP-SPA, telomerase activity could be detected with as few as 10 cell and a very high signal-to-noise ratio. However, as other alternative TRAP methods, it is sensitive to PCR artifacts.
Research has been focused toward PCR-free methods that maintain high sensitivity while also eliminating the complexity and drawbacks of the PCR.

1.3.2 Electrochemical and optical biosensors for telomerase activity detection

TRAP assay constitutes to be the standard technique to detect telomerase activity, but it suffers from many drawbacks, such as the need for expensive lab equipment and the high complexity. To overcome these disadvantages, simpler and cheaper solutions can be developed in the form of biosensors, which offer a valuable alternative to perform such investigations.

Electrochemical analysis

Among others, electrochemical analysis is a common technique used to study the properties of various analytes and it can be applied also to telomerase detection. Electrochemical analysis is often carried out in an electrochemical cell through diverse methods such as potentiometry, coulometry or voltammetry. An electrochemical cell consists of three main elements: an electrolyte and two electrodes (anode and cathode). When an electric potential is applied with respect to the reference electrode, a redox reaction takes place and there is charge transfer from one electrode to the other through the electrolyte. In Fig. 1.3.2a an electrochemical cell with three electrodes is presented. This particular configuration comprises a working electrode (WE), a reference electrode (RE) and a counter (or auxiliary) electrode (CE).
An electrochemical cell can be represented by an equivalent electric circuit, in which the circuit elements describe the different physical phenomena that happen on the cell. One of the most common models is the Randles circuit, shown in Fig. 1.3.3. The R_S term models the active electrolyte resistance and it is in series with the parallel combination of a double layer capacitance C_{dl}, a charge transfer resistance R_{ct} and a Warburg element Z_W. In particular, the C_{dl} term describes the capacitance that is present on the interface between the electrode and the electrolyte. A double layer is formed when ions from the solution adsorbs onto the electrode surface and act like a dielectric in a capacitor; thus, the electrode-electrolyte interface behave as a capacitance. In addition to this, the charge transfer resistance R_{ct} describes the behavior of the transfer of charge from the electrodes to the solution; finally, a Warburg element models the diffusion process.

A characterization of the equivalent circuit, and thus of the reaction that

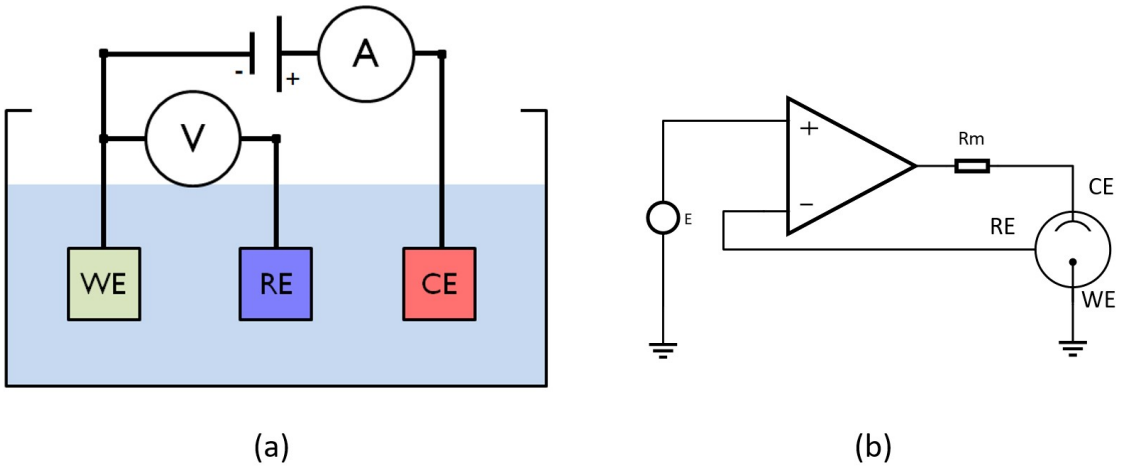

Figure 1.3.2: (a) Representation of a three-electrodes electrochemical cell. (b) Schematic of a potentiostat.

happens on the electrodes, can be performed by electrochemical impedance spectroscopy (EIS). This technique allows to estimate the circuital elements of the equivalent electric circuit by applying a small AC potential and measuring the resulting AC current. The properties of the electrochemical cells can then be estimated by measuring the frequency response.

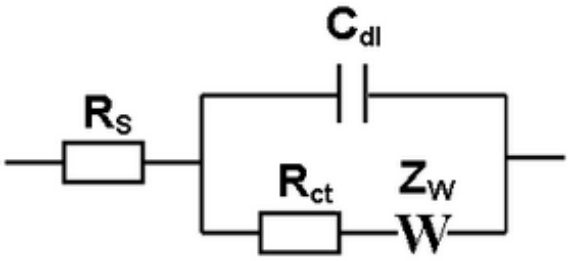

Figure 1.3.3: Randles circuit schematic.

Another electrochemical method which is used to analyze an electrochemical cells is represented by voltammetry. Voltammetry is performed by measuring the current derived from charge transport as a function of the potential applied on the working electrode with respect to the reference one. The resulting graphs, which represent the current as a function of the applied potential, are called *"voltammograms"*. Voltammetric techniques are considered to be *"active techniques"* as opposed to potentiometry, because they involve a variation of the applied potential and the monitoring of the current over time. The technique can be subdivided into different categories depending on the potential applied: for example, in cyclic voltammetry (CV) the potential is swept in both directions while measuring current, resulting in a simple response; furthermore, over the years many forms of potential modulation have been used, as normal pulse voltammetry (NPV) or square-wave voltammetry (SWV), resulting in increased speed and sensitivity.

Voltammetry allows to examine the reactivity of the analyte and it is used for quantitative determination of dissolved substances, studies of redox processes and many others bio-chemical applications [27]. The concentrations of the redox species on the electrodes and the rate of the reaction are controlled by the applied potential. The current is a function of different factors as the concentration of the species, the size and material of the electrodes, the solution resistance and the number of electrons transferred.
The potentiostat is the main instrument used in voltammetry analysis. To provide a more stable setup for voltammetry, a three-electrode electrochemical cell is used, as explained above and as shown in Fig. 1.3.2. The reaction takes place in the working electrode, while the reference electrode is maintained at a constant potential and the counter electrode passes all the current needed. The three-electrodes configuration has the advantage of separating into two different electrodes the tasks of maintaining a constant potential and, at the same time, passing the necessary current, which is not easy to implement in a single electrode due to the voltage drop caused by the double layer. The purpose of the potentiostat is to apply a known potential on the reference electrode and measure the current that flows through the counter electrode. A conceptual drawing of a potentiostat is depicted in Fig. 1.3.2b. An operational amplifier is used, exploiting its high input resistance, in order to maintain the voltage between the working electrode and the reference electrode as closely as possible to the input potential E.
This approach can be used in order to detect the presence of an analyte (or a derivative), and develop various sensors. As an example, applied to the detection of telomerase activity, Tominaga et al.[28] focused their studies on a new oral cancer screening method based on an electrochemical assay. Oral cancer screening is often executed by oral surgeons or cytodiagnosis, but the former is time-inefficient and the latter has an unacceptable rate of false-positives to be used effectively. Thus, Tominaga et al. proposed an *Electrochemical Telomerase Assay* (ECTA) method that, unlike TRAP, does not require PCR or gel electrophoresis, is easier to perform and is less susceptible to telomerase inhibitors.
The assay consists on a ferrocenylnaphthalene diimide (FND) based ECTA. Electrochemical measurement were performed using a three-electrodes potentiostat in which the primer was immobilized in the working electrode. An Osteryoung square wave voltammetry (SWV) was used, in which the applied potential consists on a square wave pulse superimposed on a staircase waveform [29]. This leads to excellent sensitivity and rejection of background noise with respect to cyclic voltammetry techniques, as well as being a fast technique and thus allowing the repetition of the experiments, resulting in an increase signal-to-noise ratio. Samples were obtained from 44 patient who suffered from oral cancer and 16 healthy volunteers; three different types of samples were collected: exfoliated cells from whole oral cavity (EO), exfoliated cells from local lesions (EL) and tissues (T). Applying SWV before and after the telomerase activity, due to the charge introduced by telomerase an increase of the current magnitude was expected. In fact, the current increase measured was significantly higher in the oral cancer group, while it was negligible in the healthy group, because telomerase expression

was not present. Also, as depicted in Fig. 1.3.4, there was no significant difference among different types of samples.

ECTA can be considered as an easier alternative to TRAP, while also retaining

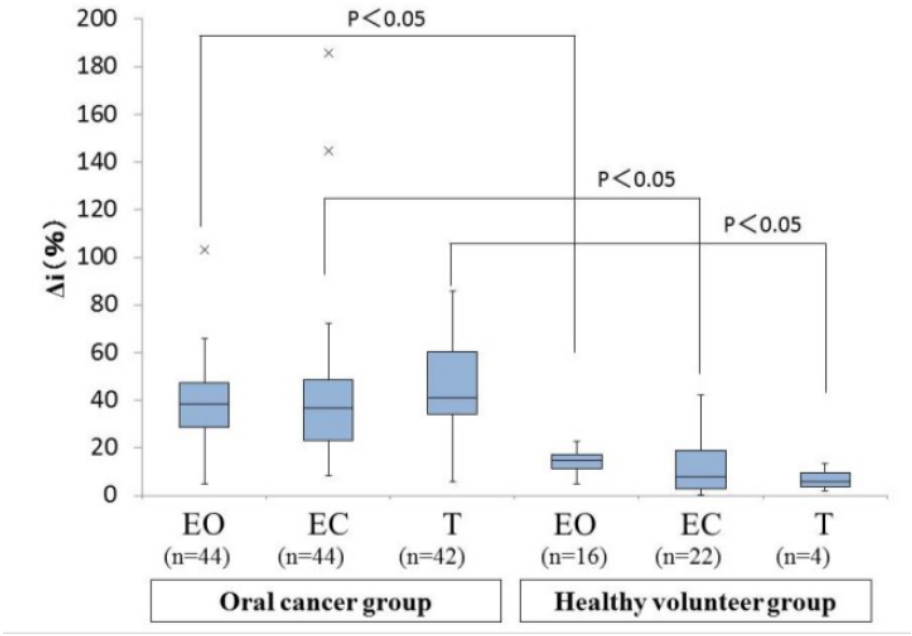

Figure 1.3.4: Comparison of current increase for different types of samples with ECTA, as demonstrated in [28].

an higher sensitivity and being able to detect telomerase activity in a small cell sample (10-100 cells). Furthermore, it's sensitivity and specificity were 94.6% and 88.6% respectively, meaning that ECTA can be effectively used as an oral cancer screening test and, in further studies, could be also applied to other types of malignant cells.

Gold nanoprobe-based optical detection

Another analytical method for the detection of biological molecules is represented by gold nanoparticles (AUNPs) which, among other properties, show tunable light-responsiveness and observable color changes relatively to modifications in the solution in which they are suspended. Additionally, upon aggregation they show variations in the maximum absorption wavelength of AuNP solution. Citrate-based AuNPs have a net negative charge on their surface, therefore they stay apart inside the solution, giving a red color to it. The addition of salt into the solution can change the superficial charge, causing the nanoparticle to aggregate and thus changing the solution color to blue or purple[30].

Pourhassan-Moghaddam et al.[31] exploited this mechanism to design gold nanoprobes which are able to detect and quantify the concentration of biological molecules, in particular nucleic acids. During DNA hybridization, the net charge on nanoprobes is highly negative and the particles are resistant to salt-induced aggregation. However, a low concentration of a target nucleic acid causes a less

resistance to the salt-induced aggregation and can favor the change of the red color and the spectral shift of the solution. For this reason, gold nanoprobes have successfully been used to detect the expression of human telomerase based on the inhibition of nanoparticle aggregation in a $MgCl_2$ solution.
Gold nanoparticles were synthesized and then characterized: through transmission electron microscopy (TEM) the nanoparticle size was determined to be 15 ± 3 nm; moreover, by interpolation of different concentrations of AuNPs in the absence of salt, the concentration was estimated to be approximately 9.8 nM. A 83 mM $MgCl_2$ solution, which was necessary to guarantee the complete aggregation of gold nanoprobes, was calculated to be optimal for the experiments. A limit of detection (LOD) of $300\,\mathrm{fmol}\,\mu\mathrm{L}^{-1}$ of synthetic hTERT (human Telomerase Reverse Transcriptase) was obtained, thus demonstrating the high sensitivity of this technique. Just as mentioned for the previous method, gold nanoprobes have the advantage of not requiring PCR or gel electrophoresis as well, thus being an optimal technique for easy and low-cost screening.

1.3.3 Electronic biosensors for telomerase activity detection

Up until this point, some techniques and methods to perform telomerase activity detection have been presented and analyzed, which make use of electrochemical and optical assays. This section expands the previously described analytical assays and shows some examples of electronic biosensors and Lab-on-a-chip (LoC) implementations which have been developed to detect biomolecules and biological processes. Some of the biosensors that are going to be illustrated below, as the flow citometry and dielectrophoresis LoC, are not specifically designed to detect telomerase-related quantities, but can be used to execute some of the steps required for more standard telomerase detection techniques such as the already mentioned TRAP.
As a matter of fact, the majority of traditional techniques related to the detection of DNA sequences or cancer markers require expensive equipment and complex steps in order to obtain data that later need to be interpreted with complex algorithms. To overcome some of these problems, in the past 20 years the research has focused on the development of electronic biosensor in CMOS technology.
As mentioned before, the implementation of a sensor in a standard CMOS process provides portability and reliability thanks to the full integration of the application, and also grants low cost mass production and increased performances over non-integrated solutions. Lastly, Lab-on-a-chip applications fabricated in CMOS technology allow to integrate sensing elements, amplification and conditioning circuitry all in the same chip, preventing the need of external devices and also providing the parallelization of operations and multiplexing capabilities.
As yet, different CMOS Lab-on-a-chip operating in several fields have been developed and tested, concerning the detection of telomerase activity by nanowires and the implementation of useful procedures as PCR, flow cytometry and dielectrophoresis.

Nanowire sensor

A first example of electronic biosensor is a nanowire-based sensor. Zheng et al. [32] presented an electronic detection method based on silicon-nanowire FET devices, capable of providing highly sensitive, label-free detection of cancer marker. Silicon-nanowire [33] and carbon-nanotube [34] had been previously used to detect binding of proteins in aqueous solution, but did not demonstrate high sensitivity nor selectivity to multiplexed detection of different proteins [35]. The innovation brought by Zheng's work was to develop integrated arrays in which independent nanowires and surface receptor can be incorporated as individual device elements, to achieve a better sensitivity and multiplexing capabilities.

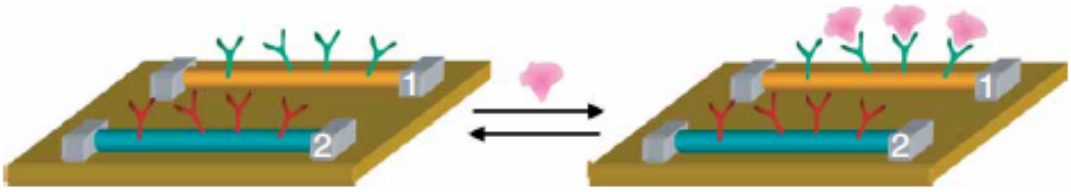

Figure 1.3.5: Two silicon nanowires modified with different antibody receptors. A cancer marker protein that binds specifically to its receptor (on nanowire 1) will produce a conductance change characteristic of the surface charge of the protein only on nanowire 1.

The nanowires, as shown in Fig. 1.3.5, were converted into sensor for protein marker detection by attaching monoclonal antibodies (mAbs) to the nanowire surface after the device fabrication. The binding of cancer marker proteins to surface-linked antibodies produces a conductance change in the corresponding silicon-nanowire device, but not in devices that lack the specific receptor. This mechanism can be exploited to obtain selective multiplexed detection by using different receptors.
Silicon nanowires conductance depends on gate voltage: in the case of a p-type device, a positive gate voltage depletes carriers and reduces the conductance, while a negative gate voltage leads to accumulation of carriers and thus an increase in conductance (the opposite is true for n-type devices). Binding of a charged species to the gate dielectric has an analogous effect of applying a gate voltage, so the conductance of a p-silicon nanowire will increase when a protein with negative surface charge binds to the antibody receptor, and will decrease with a positive surface charge [33].
This technique has been applied to detect protein cancer marker and, more specifically, to perform telomerase detection. In the first step, silicon-nanowire device elements are functionalized with oligonucleotide primers complementary to the telomerase binding site. Later, the presence or absence of telomerase is detected by measuring the device conductance after the delivery of a sample cell extract.
To understand how a biomolecule can be detected by means of its charge, it is useful to introduce the concept of isoelectric point (pI). The isoelectric point of a

biomolecule is the corresponding pH value at which the molecule shows an electrically neutral property; if the pH of the surrounding solution is higher than the pI, the molecule shows a negative charge, while if the pH of the solution is lower the molecule shows a positive charge. Since telomerase has an isoelectric point pI of about 10 [36], at physiological pH it shows a positive charge. This can be exploited to detect a telomerase molecule by means of the net charge it carries; in p-type devices, the positive charge induced by telomerase causes a reduction in conductance. Finally, the addition of deoxynucleotide triphosphates (dNTPs) causes, in presence of telomerase, the elongation of telomeres, which leads to an increase of conductance due to the extra number of negatively charged nucleotides. Just as the previously described methods, silicon-nanowire detection does not require PCR. The nucleotide addition and the consequent conductance variation depend on the telomerase concentration bound initially to primers. Experiments showed that the implemented application [28] is capable of reaching a high sensitivity, being able to detect telomerase binding at the ten-cell level without amplification. Finally, although some previously described assays, as gold nanoparticles, can reach even higher sensitivities, silicon-nanowire detection does not require labeling and additionally allows multiplexed detection.

Lab-on-Chip for quantitative PCR

As explained in the first section of this Chapter, TRAP is the most common technique to detect telomerase activity. The core steps in TRAP requires the execution of polymerase chain reaction (PCR), which generates millions of copies of a DNA segment.
Norian et al.[37] in 2014 presented a CMOS LoC application capable of performing quantitative PCR (qPRC). qPCR, or real-time PCR, is a technique based on PCR in which the amplification of the target DNA molecule is monitored in real-time and not exclusively at the end of the process. The Lab-on-a-chip was implemented in a high-voltage 0.35 µm process and a 3.3 V supply. The device can perform electrowetting droplet-based transport, reagent heating, temperature sensing and integrated fluorescence measurement. The chip surface constitutes of three areas at different temperatures, shown in Fig. 1.3.6 in which the droplets can be displaced through electrowetting-on-dielectric (EWoD) transport [38]. Electrowetting is a principle through which the wettability of liquids can be controlled using an electric potential. By changing the wettability of the electrodes, a liquid can be shaped and transported along the active electrodes. Once the droplet are in place, the thermal cycles required for the qPRC are applied. Finally, fluorescent measurement are taken with integrated Geiger-mode single-photon avalanche photodiodes (SPADs) [39].

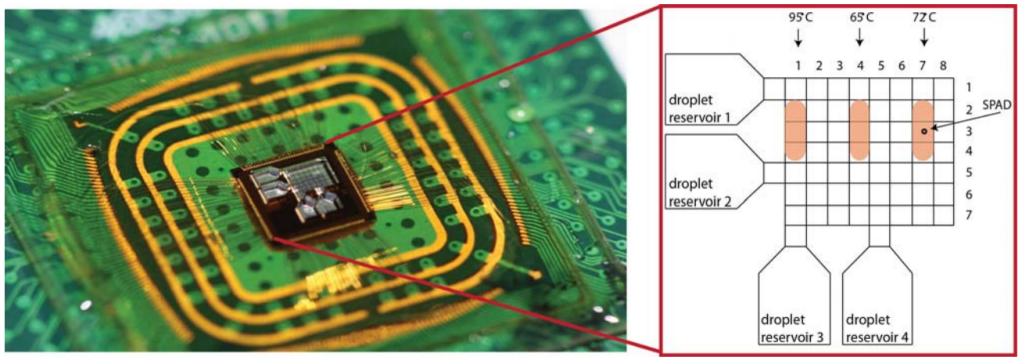

Figure 1.3.6: qPCR LoC implemented in [37]. The 4 mm-by-4 mm chip contains a 7-by-8 array of 200 μm by 200 μm electrodes to enable electrowetting-on-dielectric (EWoD) droplet transport.

PCR efficiency is greater with the qPCR chip with an average of 84.4% over the region of active amplification, with respect to 69.6% obtained with the MJ-Mini PCR thermal cycler used as comparison [37]. Fluorescent data is collected following the elongation stage of each PCR cycle, and SPAD detection limits are in the nM regime.

Flow cytometry

Flow cytometry is a laser-based technology used to accomplish cell counting [40], cell sorting [41] and biomarker detection [42]. It operates by suspending cells in a stream of fluid that traverses the region of space where a laser is used, generating light scattering or fluorescence. Flow cytometry is commonly used to measure the fluorescence of cells or other particles, which first need to be labeled with fluorescent chemicals, both directly (as in the case of DNA) or attached to antibodies (as in the case of different proteins) [43].
Hartley et al. [44] introduced a CMOS optical sensor to perform integrated cytometry on a chip, implemented with 0.18 µm CMOS technology coupled with a microfluidic system. The active pixel optical sensors, shown in Fig. 1.3.7 (a), arranged in a linear array, consist of a photodiode combined with a p-channel device to increase the pixel dynamic range. The output of the pixel sensor is connected to a correlated double sampling circuit, to subtract noise and offsets. Finally, there is spatial filter whose output is accessible as a 16-bit serial word.

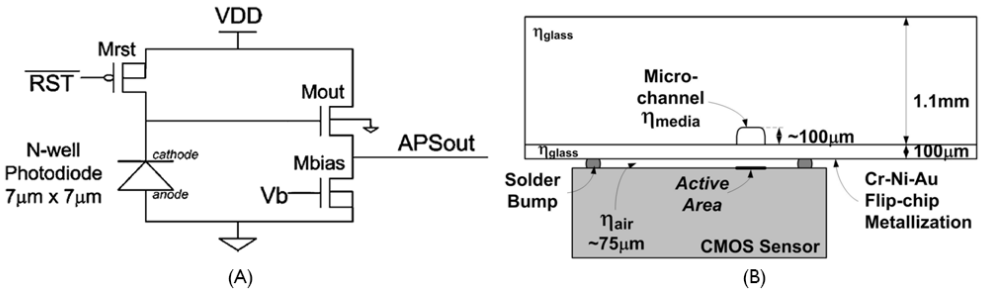

Figure 1.3.7: (a) Active pixel topology with photodiode; (b) Cross-section of the integration of sensor and microfluidic device. From [44].

The microfluidic system is implemented in a 1.1 mm thick glass sheet, which also delivers mechanical stability. The active area of the sensor is then bonded on the bottom of the glass sheet utilizing flip-chip technology, as shown in Fig. 1.3.7 (b). The microfluidic channel, with a width and depth of 100 µm, pass transversely over the center of the linear sensor array such as the pixel array spans the entire surface of the channel.
In 2009, Handa et al. [45] proposed the use of flow cytometry to detect hTERT expression. Their analysis through flow cytometry showed a quantification of telomerase activity in different components of bone marrow hematopoietic cells, and a commercial flow cytometer was used (BD FACSCalibur™). In a future application, the flow cytometry LoC could be employed to perform easier and less expensive flow cytometry related to telomerase activity detection.

Dielectrophoresis

Dielectrophoresis (DEP) is a physical phenomenon in which some neutral particles experience a force due to the application of a non-uniform electric field. The force exerted is dependent on the increasing or decreasing electric field and the physical properties of particles and medium.
Manaresi et al. [46] proposed a CMOS Lab-on-a-chip to individually detect and manipulate more than 10,000 cells in a parallel fashion through dielectrophoresis, utilizing the DEP-cages approach. The chip framework, which utilizes standard 0.35 µm CMOS, has a two-dimensional 320x320 array of microsites and a 9-bit row/column decoder for random access. Every microsite consists of a superficial electrode, embedded sensors and logic. The electrode is implemented in standard CMOS top-metal and protected by a standard passivation. A closed DEP cage can be created above each microsite by way of applying in-phase and counter-phase sinusoidal voltages to the electrodes, thus trapping and levitating particles inside the cage.
The device implemented has many advantages over standard lab equipment, such as the capability of performing parallel analysis on a large number of individual cells and isolating cells from a small sample. Finally, the programmability of the system opens the way to the development of different analytical protocols which share the same hardware.
Dielectrophoresis has many application in the field of nucleic acids [47]; this

technique can be used to manipulate, separate and analyze DNA molecules, and it is a label-free technique. In a telomerase-detecting environment, dielectrophoresis could possibly be used to trap and immobilize (permanently or not) DNA to a solid surface, a necessary step in some telomerase detection techniques.

2 | CMOS Lab-on-Chip for telomerase detection

In Chapter 1 many biosensor applications have been reviewed, the majority of which have been implemented in standard CMOS technology. This, along with the fact that the innovations introduced in CMOS fabrication processes allow the increasing integration of more complex devices, leads one to believe that direct electronic detection of biological processes is the most promising approach to follow. CMOS technology can be used to implement the most diverse detection methods, from optical sensors, as seen in [44], to conductance-based readout as in [32].
As an alternative to the previous mentioned examples, Field-Effect Transistor (FET) has been accurately investigated as a biotransducer, thanks to its property of being a *multi-parameter* device. More specifically, the output current I_D can be expressed as a function of various parameters:

$$I_D = f(\mu, C_{OX}, W, L, V_{GS}, V_{DS}, V_{TH}) \tag{2.1}$$

in which process-dependent (mobility μ, oxide capacitance C_{OX}) and geometric (width and length of the channel) parameters are taken into account, in addition to the operative voltages employed (gate-to-source voltage V_{GS}, drain-to-source voltage V_{DS} and threshold voltage V_{TH}).
Over the years various modifications of the basic FET structure have been proposed as an alternative to perform biological sensing. For example, an Ion-Sensitive FET (ISFET) can be obtained by substitution of the metal-insulator interface with an electrolyte-insulator interface, and is illustrated in Fig. 2.0.1(b) beside a standard MOSFET (a). Presented in 1970 by P. Bergveld [48], the Ion-Sensitive FET (ISFET) was originally proposed for pH sensing, but has also been used as a telomerase biosensor [49].

Another variation of a MOSFET structure is the Charge-Modulated FET (CMFET). Because of its properties, CMFET has been chosen as the basis for this work. The next section explains in detail the working principle of the CMFET. Moreover, its application as sensing unit for telomerase activity detection and how it can be integrated in an electronic platform will be briefly explained. A more detailed description of the sensor's design will be introduced in Chapter 3, while the readout schemes and other circuits will be presented in Chapter 4.

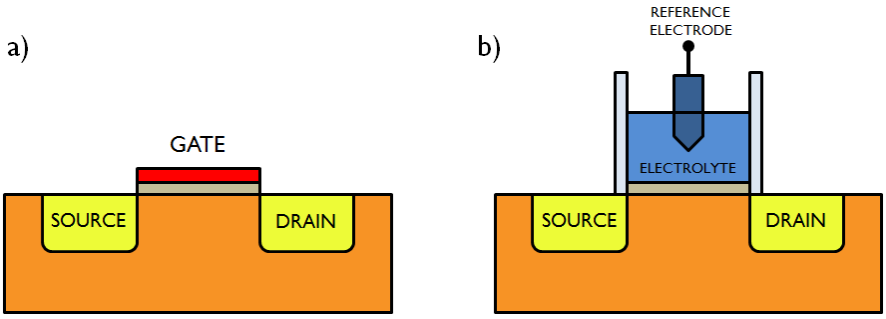

Figure 2.0.1: (a) Standard MOSFET structure. The gate terminal is separated from the Silicon substrate by an oxide layer. A voltage applied on the gate modifies the charge underneath and a channel where current flows is formed between the source and drain diffusions. (b) ISFET structure. The gate electrode is repleced by an electrolytic solution and a reference electrode. Thus, the output current depends on the ions concentration in the solution.

2.1 CMFET

Firstly presented by Barbaro et al. [50] in 2006, CMFET is a direct evolution of the floating-gate MOS transistor and is made up of a floating gate transistor M_0, a control gate V_{CG} and an active area A_S. The section of the original implementation is shown in Fig. 2.1.1.

2.1.1 CMFET working principle

CMFET can sense charge variation on the active area (also called "sensing area" throughout this work) and its threshold voltage varies according to the charge immobilized in the active area. The active area is created through a standard pad opening in SiO_2 passivation and the charge to be sensed has to be chemically bounded to the surface. DNA probes are bounded on top of the exposed active area by an organic/inorganic interface called spacer. Both the charge on the active area and the voltage applied to the control gate (V_{CG}) contribute to the voltage applied to the floating-gate with respect to the Si substrate. The device can be modeled as a standard MOSFET with a modified threshold voltage, that depends on the voltage applied to the control gate and on the charge on the active area.

The charge Q_S, immobilized on the active area, generates an electric field which causes charge separation inside the buried gate. A charge Q_i is induced on the top side of the floating gate and an opposite charge $-Q_i$ appears on the bottom side, since the total charge in the buried gate must remain constant. This gives rise to one of the two contributes that constitute the V_{FG} voltage, which can be used to turn on the MOS. If a p-type substrate is used and the Q_s charge is positive, the induced V_{FG} variation leads to switch on the device, while a negative Q_S charge will switch off the MOS. The contrary is true if a n-type substrate is used.
Equation for the model can be derived applying the charge conservation principle on the closed surface that contains the floating gate. The total charge Q_{F0} on the

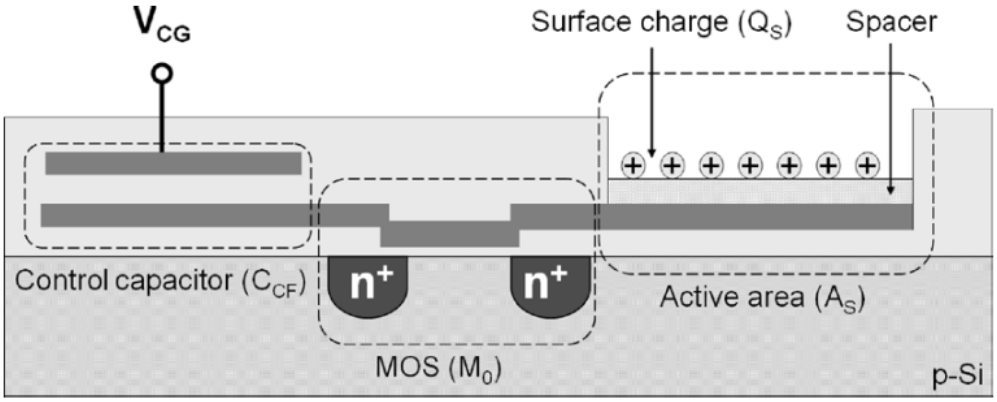

Figure 2.1.1: CMFET structure as presented in [50]

floating gate must remain constant, and it depends on the induced charge $Q_i(Q_s)$, the charge between control gate and floating gate Q_{CCF} and finally the charge between the floating gate and the bulk of the device Q_{CFB}:

$$\begin{aligned} Q_{F0} &= Q_i(Q_s) + Q_{CCF} + Q_{CFB} \\ &= Q_i\left(Q_s\right) + C_{CF}\left(V_{CG} - V_{FG}\right) + C_{FB}V_{FG} \end{aligned} \tag{2.2}$$

where all the voltages are expressed relatively to the bulk voltage. The terms C_{CF} and C_{FB} are respectively the capacitance value of the control capacitor and the stray capacitance between the floating gate and the substrate.
From Equation (2.2) a relation between floating gate voltage and capacitances in the device can be derived:

$$V_{FG} = \frac{C_{CF}}{C_{CF} + C_{FB}} V_{CG} + \frac{Q_{F0} - Q_i}{C_{CF} + C_{FB}} \tag{2.3}$$

Therefore the drain current of the M_0 MOS is determined by the voltage V_{CG} applied to the control gate and the charge Q_s in the active area.
The effect of all the different sources can be modeled as a variation of an effective threshold voltage V_{THF}. A new model that shows the effective threshold voltage relation can be obtained:

$$\begin{aligned} V_{FG} - V_{TH} = V_{CG} - V_{THF} &= \frac{C_{CF}}{C_{CF} + C_{FB}} V_{CG} + \frac{Q_{F0} - Q_i}{C_{CF} + C_{FB}} - V_{TH} \\ &\simeq V_{CG} - \left(V_{TH} - \frac{Q_{F0} - Q_i}{C_{CF} + C_{FB}} \right) \end{aligned} \tag{2.4}$$

Equation (2.4) is valid under the approximation that $C_{CF} \gg C_{FB}$, that is the capacitance originating from the coupling between floating gate and bulk has to be negligible respect to the control capacitance.
From this, the expression for the effective threshold voltage V_{THF} can be obtained. In fact, in a first-order model, a perfect induction can be hypothesized if the spacer thickness is much thinner that other dimensions. Therefore the induced charge Q_i

results equal in magnitude and opposite in sign t the surface charge Q_s.

$$V_{THF} \simeq V_{TH} - \frac{Q_{F0} - Q_i}{C_{CF} + C_{FB}} \simeq V_{TH} - \frac{Q_{F0} + Q_s}{C_{CF} + C_{FB}} \tag{2.5}$$

Finally, the variation of threshold voltage can be expressed as:

$$\Delta V_{THF} \simeq \frac{-\Delta Q_S}{C_{TOT}} \tag{2.6}$$

where ΔQ is the variation of immobilized charge and C_{TOT} is the sum of all the capacitances on the floating gate ($C_{CF} + C_{FB}$).
Therefore, if the charge Q_{DNA} increases, this will result in a negative shift of the effective threshold voltage, while a decrease of Q_{DNA} will result in a positive shift. The first causes a n-type MOS to turn on due to the increase of negative charges in the channel, whereas the latter causes the NMOS to turn off, due to an increase of positive charges. P-type transistors are subjected to the opposite phenomenon.

2.1.2 CMFET as a DNA sensor

CMFET seems a suitable alternative for a device that needs to detect biological processes activity, specifically telomerase activity, because:

- it is possible to completely integrate CMFET in a standard CMOS process, thus keeping all the advantages of CMOS technology as high precision, large scale of integration and low cost fabrication process on mass production;
- as opposed to other DNA sensors, in which the probes are directly bound to the MOS gate, the CMFET active area and the MOS transistor do not have to lay on the same plane. This can lead to an easier design of the layout, in which the biological process and the transduction mechanism can be decoupled.

For these reasons, CMFET appears as a very promising device to perform detection of biological processes which involve charge variations, and has already been implemented as a DNA hybridization sensor.

DNA hybridization by CMFET

DNA hybridization detection is a crucial step in the development of diagnostic tools, while also finding application in different areas such as forensic investigation. The standard approach utilizes optical detection and often requires DNA immobilization and labeling, thus being an indirect method [51]. Other techniques have been developed which are label-free but are still difficult to integrate with standard CMOS technology.
In 2006 Barbaro et al. [52] proposed a solid-state CMFET device able to perform a label-free detection of DNA hybridization. The chip was designed in a standard 0.8 µm CMOS process with two metal layers and two polysilicon layers. DNA hybridization detection is made possible by immobilizing single DNA strands in

the sensing area. When hybridization occurs, the addition of nucleotides causes an increase in the negative charge immobilized on top of the sensing area, which then affects the threshold voltage of the device, as stated in Equation 2.6, thus leading to an increase in the output current of the transistor.
The chip developed comprises 16 sensors divided in two clusters: an active cluster and a reference cluster, needed to test the selectivity of the device. Two PDMS micro-chambers were used to functionalize the sensing areas by activating the surface with spacer molecules and anchoring the DNA single strands to the spacer layer.
In 2007 an evolution of the above mentioned chip was presented [53]. It was implemented in a standard 0.35 µm CMOS process with two poly layers and five metal layers. In addition to the core sensing unit, which also utilizes CMFET sensors but in a PMOS-NMOS pair to extend the sensitivity range, this version of the chip includes two different read-out schemes, PTAT (Proportional To Absolute Temperature) sensors, a variable gain amplifier and a cyclic A/D converter, all of which are controlled by a digital control unit (DCU). The sensing part of the chip is composed of 80 sensors, subdivided in two arrays in order to allow differential measurements and thus test the specificity of the detection. A microfluidic system with two channel was also developed.
In 2012 the DNA hybridization LoC was improved, and several innovations were

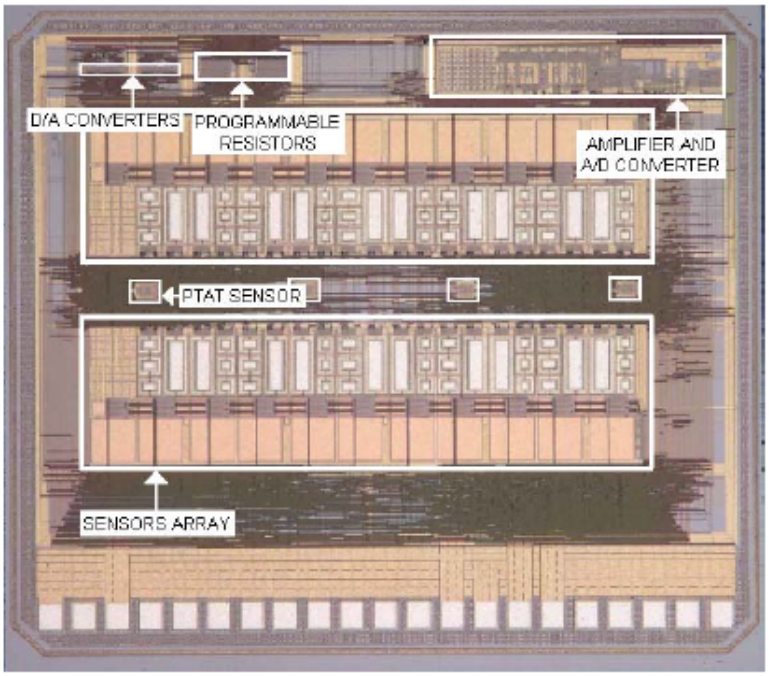

Figure 2.1.2: A microphotograph of the chip.

introduced [54, 55]. In this work, a refined model of the stray capacitance of the CMFET structure has been presented and validated, thus allowing a more precise modeling of the device behavior. All the steps required to perform DNA hybridization were tested and validated with fluorescence.
Figure 2.1.3 shows some experimental results obtained with the implemented

CMFET technology. In (a) the variation of threshold voltage during surface functionalization and DNA hybridization is plotted, while in (b) the extrapolated charge variation evaluated in all three steps is shown. These results show two main aspects of the CMFET working principles: first, as demonstrated in Fig. 2.1.3(b), the charge variation is proportional to the sensing area of the devices, which have been implemented in three different sizes. The sensor with the larger sensing area is subjected to the larger charge variation.
Moreover, the effective threshold voltage variation on CMFET is highly dependent on the capacitances of the device. This is clear in Fig. 2.1.3(a). In this example, sensor with large areas display a smaller threshold voltage variation, even though the charge on their surface is larger than the other sensors. This is due to the parasitic capacitance that exists between the sensing area and the bulk, which contributes to the increase of the C_{TOT} term and thus causes a decrease in sensitivity. The detection limit was found in 0.1 nM concentration and a linear dependence of the detected charge is obtained up to 100 nM dilution. Finally, the highest detectable concentration taken is 1 µM, due to the limits deriving from the sensing structure. Selectivity test were also made by using DNA molecules which differed from the target sequence for a few basis. No significant charge variation was measured when using modified sequences, while a strong variation was measured when injecting the target sequence. In conclusion, the results obtained show that CMFET approach in CMOS technology is feasible and it can be an interesting starting point for the development of an electronic platform for biological sensing.

2.2 Telomerase activity detection process

Once CMFET capability to detect charge variations has been demonstrated and implemented successfully, it is easy to expand its application field to all the biological processes which involve charge variations.
Telomerase activity represents a good candidate for detection by CMFET, because it gives rise to charge variations during all the steps of the process.
Telomerase activity detection requires a proper measurement protocol. The process is subdivided into three main steps:

- the first step consists in the functionalization of the sensing area through immobilization of DNA probes. The immobilized probes are single DNA strands which contain one or more repetition of the telomeric sequence TTAGGG. The first portion of probe consists on a *stuffer* sequence, which is needed to separate the telomeric sequence from the sensitive surface, to avoid that telomerase physically hinders the process. A typical probe has a length comprised between 24 and 30 nucleotides; using longer probes could be detrimental to the functionalization and covering process because longer strands tend to form less ordinate structures, thus reducing the covering of the surface. In this phase, a negative charge should be detected: in fact, each nucleotide brings a single negative charge to the sensing area region. This

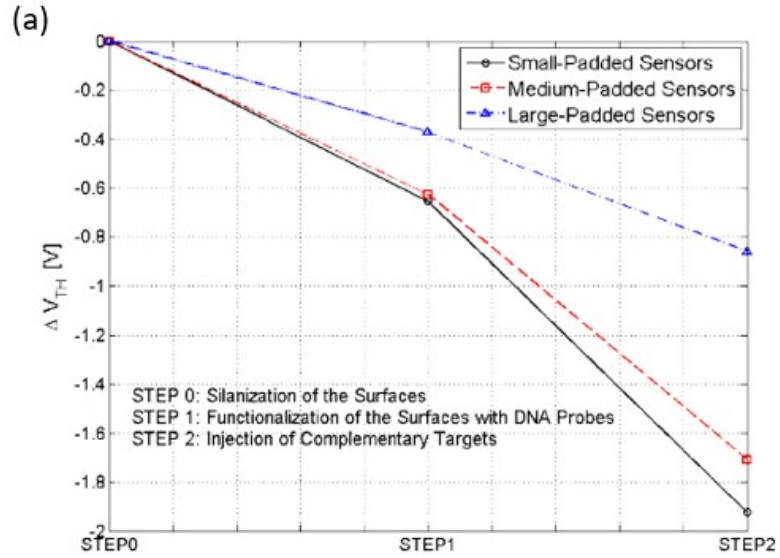

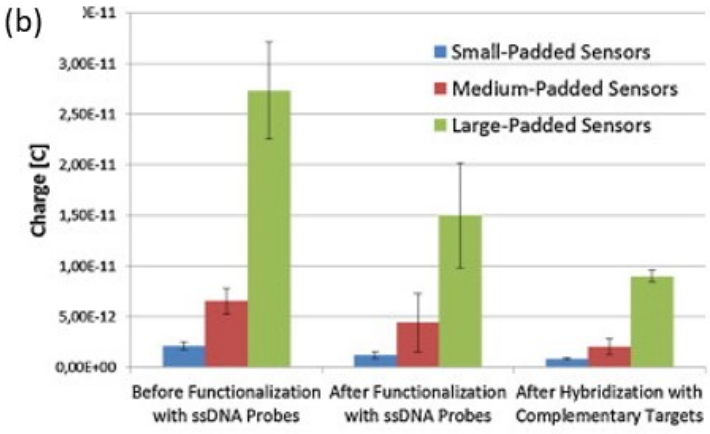

	Functionalization		Hybridization	
Sensor Type	Q_{oligos} [C]	Density (oligos/m²)	Q_{oligos} [C]	Density (oligos/m²)
Small-Padded	$(1.2\pm0.3)\cdot10^{-12}$	$(2.7\pm0.7)\cdot10^{14}$	$(8.4\pm1.2)\cdot10^{-13}$	$(5.1\pm2)\cdot10^{13}$
Medium-Padded	$(4.4\pm2.9)\cdot10^{-12}$	$(6\pm4)\cdot10^{14}$	$(2\pm0.8)\cdot10^{-12}$	$(2.1\pm0.7)\cdot10^{14}$
Large-Padded	$(1.5\pm0.5)\cdot10^{-11}$	$(3.6\pm1.2)\cdot10^{14}$	$(9\pm0.3)\cdot10^{-12}$	$(9\pm0.9)\cdot10^{13}$

Figure 2.1.3: (a) Average differential threshold voltage variation during the steps required for DNA hybridization; (b) average differential charge variation during the functionalization and hybridization processes.

reflects as a positive shift of the effective threshold voltage;

- once the probes are immobilized on the sensitive surface, telomerase molecules can be added to the solution. As explained in Chapter 1, telomerase presence can be detected thanks to its net charge. Since isoelectric point of telomerase is about 10, at physiological pH there is a positive net charge associated with each telomerase molecule. Thus, a negative threshold voltage shift occurs;

- the final step to perform telomerase activity detection requires to estimate the

elongation of the telomeres caused by telomerase. Telomeres bring a negative charge, so a positive threshold voltage shift should be detected. The limit of measurable telomere elongation is given by the Debye length λ_D, which is the maximum distance after which the charges are electrically screened by the ions contained in a solution and it is equivalent to the double layer introduced in Chapter 1 for an electrochemical cell. It is estimated that to avoid the screening effect of the ions diluted in the solution, the Debye length has to be at least two times the length of the longest strand. Since a typical strand has a length between 10 and 15 nm, a Debye length of about 30 nm is required. The required λ_D value can be obtained by properly preparing the solution used for measurements.

2.3 Chip architecture

The work described in this thesis is centered around the development of a CMFET-based Lab-on-a-chip device, specifically engineered to perform telomerase activity detection. In a Lab-on-a-chip device, the sensing unit has to be integrated and included in an environment which allows to perform the transduction of the biological process into a more convenient physical quantity, more specifically an electric signal, and the subsequent elaboration of the signal to permit the analysis of the data. Therefore it is necessary, beside the development of the single sensing element, to design all the necessary circuitry that implements the additional functions. For this reason, this Section introduces the general architecture of the chip and briefly explains the role of each fundamental module.
The circuit has been designed in a standard 0.18 µm CMOS process with six metal layers and simulated through Virtuoso Analog Design Environment (ADE). The chip architecture comprises, in addition to the active pixel unit, three different read-out methods and an A/D converter. Digital cells to allow multiplexing, single sensor addressing and measurements management have also been developed. A block diagram of the chip architecture is shown in Fig. 2.3.1.

2.3.1 Sensor array

The core of the chip is represented by multiple sensor channels, each one implementing an array of 32 sensors for a total of 1024 sensors on the chip. Such a large number of sensors has been chosen thinking about alternative applications to telomerase detection, such as liquid biopsy. Liquid biopsy, or fluid biopsy, [56] is a diagnostic non-invasive technique for the detection and monitoring of cancer through the analysis of cfDNA (circulating free DNA) released by tumours in the blood. The large number of sensors could be used to detect different kinds of cfDNA biomarkers with statistical relevance. The single sensing unit is composed of a CMFET sensor, as described in the previous section. The design, layout and simulation of the sensing units are presented in detail in Chapter 3.

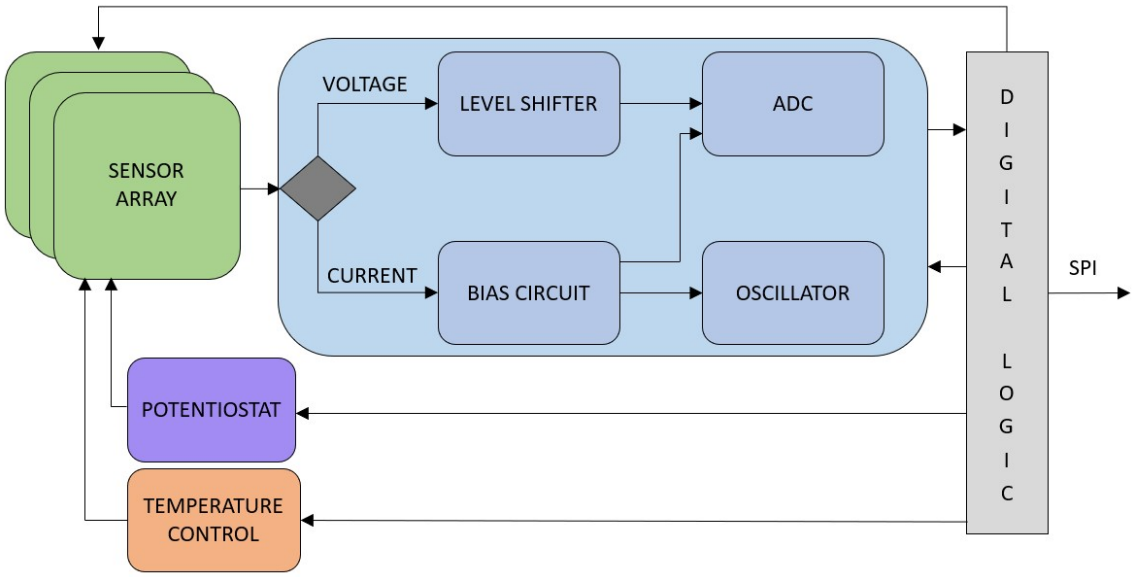

Figure 2.3.1: A block diagram of the chip architecture.

2.3.2 Read-out circuitry

Three different read-out methods have been included in the chip design, which are explained in more detail in Chapter 4.
The sensor can either be connected to a voltage or a current read-out scheme. The generated voltage is proportional to the threshold voltage variation and can be directly converted by means of an on-chip ADC (analog-to-digital converter). The current read-out scheme offers more possibilities: a current is generated in a modified self-biasing current reference scheme in which the resistor has been replaced by the sensor. Hence, the generated current depends on the sensor's current, which in turn depends on the threshold voltage. From here, measurements can be performed in two different ways:

- if the ADC path is selected, a direct readout of the current is performed. The ADC operates in a dual slope configuration, by charging a capacitance and measuring the time needed to discharge it with a known current. Then, a digital counter (thus acting as a time-to-digital converter) measures the elapsed amount of time required for the discharge, which is proportional to the current value;

- if the current-to-frequency path is selected, the current is used to drive a five-stages *current-starved oscillator* which generates a current-controlled square wave. Any variations in the effective threshold voltage of the sensor translate in a variation of the generated current, which reflect on the output frequency of the oscillator.

The three read-out paths can be selected by the digital control logic, and provide different ranges of measurement.

2.3.3 Integrated potentiostat

An integrated potentiostat has been added to the LoC in order to allow different characterization of the sensing area and, possibly, the employment of various electrochemical functionalization procedures. A standard implementation of a potentiostat utilizes three electrodes: a working electrode (WE), a reference electrode (RE) and an auxiliary or counter electrode (CE). The potentiostat measures the current that flows in the counter electrode while keeping the working electrode at a constant potential with respect to the reference electrode.
The floating-gate structure of the CMFET makes it possible to implement a two-electrodes potentiostat, in which the two electrodes are realized through the metal surface of the sensing areas of the sensors in the array. To address the two active areas, a switch has been integrated in the layout of the pixel, allowing to start the potentiostat operations and to provide a path for the current flow between CE and WE, which would otherwise be impossible due to the floating gate nature of the sensor.

2.3.4 Temperature control system

Since telomerase catalytic activity increases with temperature [57], a temperature control system has been designed to keep the temperature around the sensing area at 37°. The temperature control system makes use of PTAT (proportional to absolute temperature) sensors spread across the sensor's channel, and a set of resistive heaters which generate heat when a current flows and can be digitally turned on and off.

2.3.5 Digital logic

To conclude the description of all the elemental blocks which constitute the proposed LoC, the digital logic is addressed. To easily interface the chip with the external world an SPI (Serial Peripheral Interface) interface has been implemented. Given the high variability of biological processes, every analog circuit here described needs to be tuned and configured. For this reason, the SPI protocol was chosen, as taking off-chip each control signal would have required an enormous amount of pads. Thus, the digital logic task is to decode commands which are sent through SPI and perform the required actions, such as writing or reading data from memory registers or starting and managing conversions. A register file has also been implemented to save both configuration parameter (such as which sensors are active or which conversion technique has been chosen) and the conversion data coming from each counter (16 bit for each of the 256 clusters). Finally, stored data can be retrieved in two different methods, both by request or by continuous data reading.

3 | CMFET-based biosensor for telomerase detection

After the introduction of the chip general architecture in Chapter 2, this Chapter focuses on modeling and designing the CMFET-based biosensor. In Section 3.1 the mathematical model of the CMFET is refined to take into accounts the telomerase sensing application; in Section 3.2 and 3.3 the design process and layout are presented, finally, in Section 3.4 the simulated behavior of the sensor in response to telomerase activity is analyzed.

3.1 Refining CMFET model for telomerase activity detection

In Chapter 2 the basic working principle of the CMFET structure has been described and an expression that represents the variation of its effective threshold voltage has been determined, as illustrated in Equation (2.6), which is reported here for the reader's convenience:

$$\Delta V_{TH} \simeq \frac{-\Delta Q}{C_{TOT}} \tag{3.1}$$

The physical quantity that allows to quantify telomerase activity is exactly the effective threshold voltage variation, and thus it is the object of measurements.
To obtain a wider sensing range, in this work an NMOS-PMOS pair has been used. As already explained, the threshold voltage variation also depend on the sign of the charge: if the charge is positive, the threshold voltage decreases (i.e. it shifts towards more negative values), whereas if the charge is negative, the threshold voltage increases (i.e. it shifts towards more positive values). This produces an opposite effect in NMOS and PMOS sensors: when the threshold voltage variation makes the NMOS turn on, it also makes the PMOS turn off and vice versa. Using a NMOS-PMOS pair instead of a single MOSFET allows to detect both positive and negative charges and thus doubles the sensing range. In fact, when one of the two MOS saturates or turns off, not allowing the correct operation of the sensor if alone, the complementary MOS is in a region that allows full operation. A schematic of the CMFET pair is shown in Fig. 3.1.1.

Before proceeding to the analysis of the readout circuitry and addressing the issue of sensitivity, it is necessary to better define the two terms that constitute the

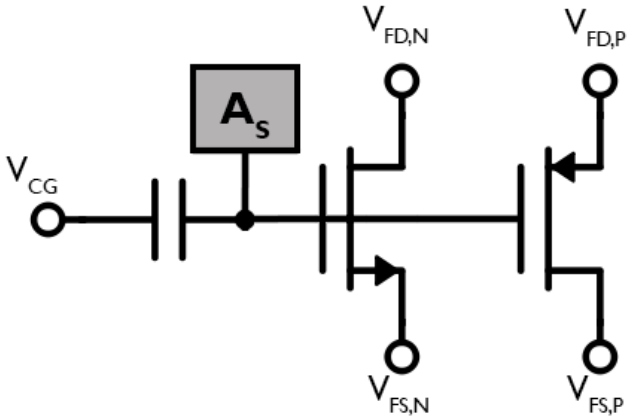

Figure 3.1.1: A basic schematic of the sensor with an NMOS-PMOS pair. In the picture are represented the control gate voltage V_{CG}, the sensing area A_s, the drain voltages V_{FD} and source voltage V_{FS} for the N-type and P-type CMFET, respectively.

threshold voltage variation: the variation of charge related to the biological process and the total capacitance of the device.

3.1.1 Charge variation model

So far in this work, charge variation generated from telomerase activity has simply been described as a charge variation ΔQ. When introducing the problem of the device sensitivity with respect to the telomerase activity, there is a need to define a precise model of the various contribution that add up to that variation. In a preliminary sensor characterization, the effective threshold voltage of the device has merely been described by the sum of the real threshold voltage V_{TH} and a variation induced by telomerase-deriving charge $V_{TH,param}$, set as a varying parameter which could be changed during simulations.
Taking into account all the physical phenomena that take place on the sensing area, the parametric threshold voltage variation has been subdivided into three main terms that depends on charge variations: $\Delta Q_{telomerase}$, ΔQ_{probes} and ΔQ_{charge}.

$$V_{TH,param} = \frac{\Delta Q_{telomerase} + \Delta Q_{probes} + \Delta Q_{charge}}{C_{TOT}} \tag{3.2}$$

All three terms introduce a charge variation proportional to the area of the metal surface used as sensing area.
The first term $\Delta Q_{telomerase}$ describes the charge induced by the telomerase activity, in particular the charges brought on the sensing area by the elongation of telomeres:

$$\Delta Q_{telomerase} = \beta \cdot \sigma_q \cdot d_{bases} \cdot q_e \cdot A_{sens} \tag{3.3}$$

in which:

- β is the process efficiency and is a number between 0 and 1 (1 meaning that telomerase elongated all the probes immobilized on the sensing area);

- σ_q is the coverage factor, or the density of DNA probes, expressed in DNA molecules per µm^2;
- d_{bases} is the number of nucleotides that telomerase adds to the existing telomeres. Since the telomeric repeating sequence is TTAGGG, if a single elongation is taken into account this parameter is fixed at 6 nucleotides;
- q_e is the electron charge, 1.602×10^{-19} C. A single electron charge is taken into account because each added nucleotide brings a single negative charge. This, multiplied by the number of nucleotides added during telomeric elongation, gives the total charge that corresponds to a single telomeric sequence;
- A_{sens} represents the area of the sensing surface in µm^2.

Essentially, the $\Delta Q_{telomerase}$ term takes into account the contribution to the threshold voltage shift due to the elongation of telomeres. It strongly depends on the number of probes that can be immobilized on the sensing area and on the percentage of probes that are elongated by telomerase. Present studies on DNA probes immobilization on aluminum and telomerase elongation efficiency does not permit to obtain precise values for σ_q and β, but a rough estimate can be done for the former, while the latter is used as a parameter. For this reason various combination of efficiency and coverage factor have been simulated, to guarantee the correct operation of the sensor in every situation.

The second term of the parametric threshold voltage, ΔQ_{probes}, is related to the probes immobilized on the sensing area. Probe immobilization is one of the steps preceding the addition of telomerase to detect its activity, so during the sensor design an initial charge has to be considered.
The expression for the ΔQ_{probes} contribution is the following:

$$\Delta Q_{probes} = \sigma_q \cdot n_{bases} \cdot q_e \cdot A_{sens} \tag{3.4}$$

As for the $\Delta Q_{telomerase}$ term, the ΔQ_{probes} term depends on the coverage factor σ_q and on the sensing area dimensions. Additionally, it depends on the term n_{bases}, which represents the length of the DNA probes immobilized on the metal surface. Each base brings an electron, thus allowing to estimate the charge present on the sensing area before the addition of telomerase and the elongation process, due to the functionalization of the surface.

The final term of the parametric threshold voltage is:

$$\Delta Q_{charge} = q_0 \cdot A_{sens} \tag{3.5}$$

and it represents a generic charge which can be already present on the floating gate following the fabrication process.

In conclusion, the model here presented offers a rough estimate of the charge contribution, which allows to simulate telomerase activity and evaluate sensor's performance as a function of process efficiency.

3.1.2 Capacitance model

Once the charge variation has been described and modeled, it is important to focus on a more precise model of the device that represents all the capacitance contributions to the C_{TOT} term.

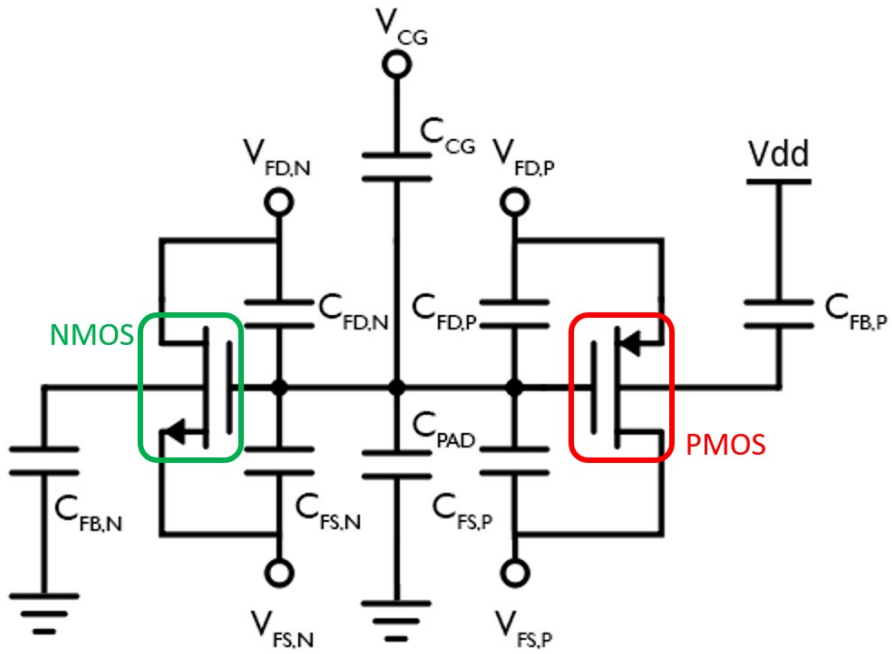

Figure 3.1.2: A schematic of the sensor that includes parasitic capacitances.

Figure 3.1.2 shows a schematic representation of the NMOS-PMOS pair which constitutes the sensor, with all the corresponding parasitic capacitance terms. The nodes V_{FD}, V_{FS} etc represents the source and drain voltages for NMOS and PMOS respectively. Capacitances can be summarized as:

- C_{CG} is the capacitance associated with the control capacitor. In the actual design it is the larger capacitance inside the active pixel, and it is the main capacitive contribution to the sensitivity of the sensor, being the greater term in the denominator of the ΔV_{TH};
- C_{FD}, C_{FS} and C_{FB} are the parasitic capacitances that derive from the coupling between floating gate and drain, source and bulk, respectively, and for both NMOS and PMOS. Their exact value can be estimated through the simulator;
- C_{PAD} is the parasitic capacitance due to the coupling between the metal surface that implements the sensing area, which has the same potential of the floating gate, and the bulk.

The sum of all the above contributions is the C_{TOT} term of Equation (3.1). After carefully designing the layout of the device to reduce the parasitic capacitances, it is possible to set a constant value of C_{TOT} by conveniently calculating the size of the control capacitor; therefore, the effective threshold voltage variation depends

only on the charge induced on the floating gate. With a control capacitor in the pF order, it has been estimated that it is possible to obtain a threshold voltage variation of tens to hundreds of mV. To extend the sensing range and to evaluate the influence of the control capacitor on the threshold voltage, two different control capacitors sizes have been designed. Thus, the appropriate size and sensing range can be chosen depending on the measurement requirements.

3.2 CMFET implementation

After a first phase of study of the CMFET structure, two different implementations have been analyzed, and a different layout has subsequently been created for both versions. The first CMFET structure in analysis directly follows the one already presented in literature, while the second structure has been thought of as an improvement of the standard structure which makes use of the *"circuit-under-pad"* technology, that allows to place a portion of circuitry under the sensing area (defined as a bond pad for fabrication purpose), to reduce stray capacitances and optimize area occupation. Taking into account the two different control capacitor sizes that have been designed, a total of four different layouts have been produced for the sensor.

3.2.1 Planar version

Following previous implementations of the CMFET [50, 52, 53, 54], a similar CMFET structure has been designed in a 0.18 µm standard CMOS process. A section of this structure, which will be referred to the *"planar"* version, is depicted in Fig. 3.2.1.

This is the standard CMFET structure. Figure 3.2.1 illustrates a n-type CMFET, but the same structure is valid for a p-type CMFET. The fabrication process made available a poly layer and six metal layer, including a thick metal layer in which the sensing area has been implemented.
The MOS transistor is a standard NMOS (or PMOS) transistor. Its gate is not directly connected to an external voltage, but it is connected to the middle plate of a sandwich capacitor and to the sensing area. Thus, the gate is a floating node the transistor can be biased by applying a voltage V_{CG} to the control capacitor.
The control capacitor is realized with a double sandwich capacitor which utilizes Metal 2 and Metal 4 for the top and bottom plate, and Metal 3 for the middle plate. This capacitor structure enables higher capacitance values to be achieved (with respect to a standard metal-insulator-metal (MIM) capacitor). It was also chosen because it met the desired capacitance values for this application, while maintaining reasonable area occupation.
Finally, the sensing area is implemented in 3 µm thick metal, and it has been exposed to allow the deposition of DNA probes and analytes. The topmost metal level has been chosen as sensing area to minimize the capacitive coupling between the metal itself and the bulk of the device. The coupling between the thick metal and the bulk amounts to about 14 aF µm^{-2}, thus in this version the C_{PAD} contribute in Fig. 3.1.2 has a capacitance of about 70 fF.

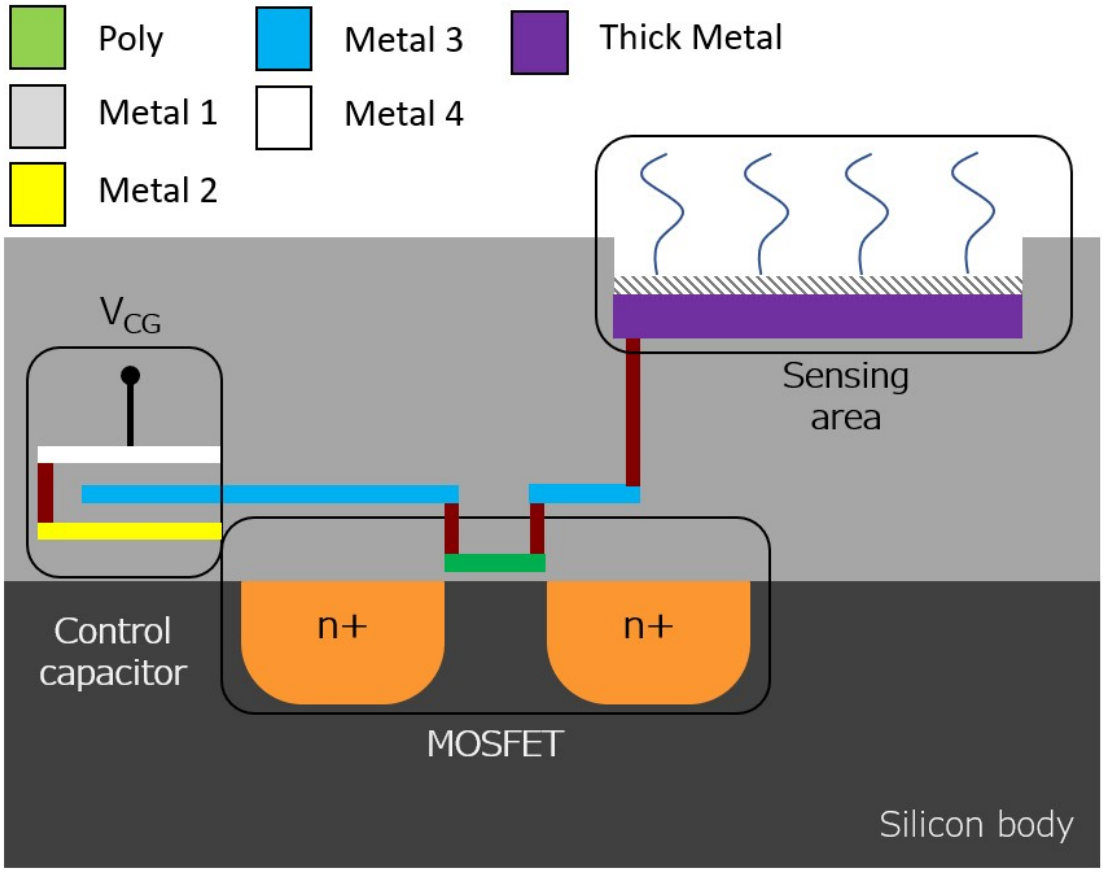

Figure 3.2.1: Section of planar CMFET structure (NMOS).

This implementation of the CMFET structure and its operation have already been tested and verified in the above-mentioned works, despite it being a slightly different application.

3.2.2 Circuit-under-pad version

To further enhance the sensitivity of CMFET, a new structure has been designed (from now on referred to as the *"circuit-under-pad" (CUPAD)* version), illustrated in Fig. 3.2.2. In particular, this implementation exploits the possibility of placing a portion of circuitry under the area occupied by a bond pad, which normally is not accessible. Therefore, defining the sensing area as a bond pad in the layout (a necessary operation to comply to the fabrication design rules), additional circuitry can be placed underneath it. This leads to two main advantages: first, it reduces the capacitive coupling between the floating gate and the bulk, thus allowing a further reduction of the parasitic capacitances; second, it is possible to fit the entire control capacitor under the sensing area, reducing the physical space it occupies and allowing the integration of a larger number of sensors with respect to the standard structure.
The advantages introduced by the circuit-under-pad version with respect to the planar version are more evident if a comparison between the large control

capacitor implementation is made as follows. While on the planar version the C_{PAD} term has a capacitance of about 70 fF, in the circuit-under-pad version this contribution becomes negligible because the control capacitor occupies all the area underneath the sensing area, thus greatly reducing its coupling with the bulk.
The area occupied is also reduced: in Table 3.1 rough estimates of sensor's area are shown. It has to be noted that the circuit-under-pad structure allows the implementation of the $45\,\mu m^2 \times 45\,\mu m^2$ capacitor version with almost the same size of the small capacitor planar sensor, while also saving about 30% of the area used by the big capacitor planar sensor.

Version	Planar	CUPAD
$25x25$ cap	$6200\,\mu m^2$	$4900\,\mu m^2$
$45x45$ cap	$9000\,\mu m^2$	$5800\,\mu m^2$

Table 3.1: Area occupation for different sensor implementations.

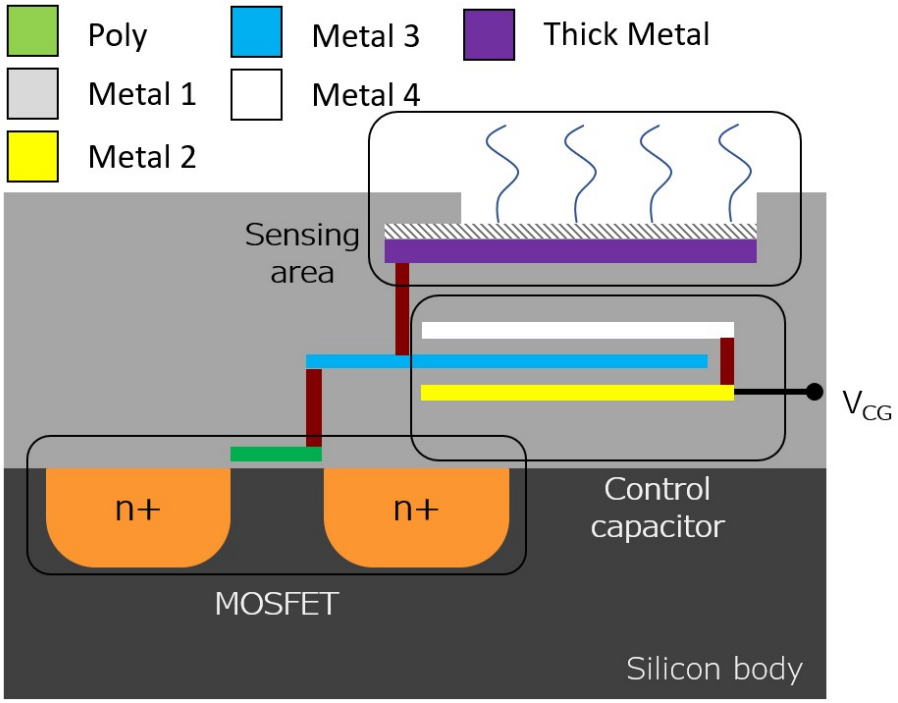

Figure 3.2.2: Section of circuit-under-pad CMFET structure (NMOS).

3.2.3 Definition of the active pixel

Once the structure of a single CMFET has been defined, it is possible to analyze the next hierarchy level, which consists in the complete active pixel.
The pixel includes, besides the CMFET pair described above, all the switches that implements multiplexing and readout scheme selection. It also includes additional n-type and a p-type MOS that match the CMFET MOS, which is needed for the voltage readout scheme.

The control signals are subdivided into two main parts: the addressing signals and the readout scheme selection:

- the addressing logic aims to select a single pixel by connecting it to the bias voltages and to the output, as shown in the block diagram in Fig. 2.3.1. It is composed of transmission gates switches, controlled by digital signals that allow to select a single sensor using row and column selection signals in a matrix-like system;
- the readout scheme selection connects the pixel to the chosen readout method. It includes N-type and P-type MOSFETs used as digital switches, which are controlled by two signals, for selecting the voltage or the current readout scheme, respectively.

Four different version of the active pixel have been designed, with different combinations of capacitor sizes and planar/under-pad structures. The active area is kept the same size throughout all the pixels and is a square metal layer with a side of 66 µm.
The size of the active area has been chosen as the minimum pad size that could be defined in the specific CMOS process. Larger areas lead to a higher sensitivity (because more DNA probes can be immobilized) but also a faster saturation of the device (because the induced charge is also proportional to the number of probes and thus the exposed metal area).

The control capacitor size has been determined by looking at two factors: the capacitive divider voltage and the sensitivity derived from the C_{TOT} term. To set the operating point of the device, a bias voltage V_{CG} can be applied on the top plate of the control capacitor, thus setting the floating gate voltage. Ideally, this should set the floating gate at the same voltage that is applied to the control capacitor. However, if parasitic capacitances are taken into consideration as shown in Fig. 3.1.2, a capacitive voltage divider effect arises because of the parasitic coupling C_{FB} between floating gate and bulk, causing the floating gate voltage to be lower than expected. For this reason, the control capacitor has to be large enough to maintain the voltage on the floating gate at least at 90% of the external applied voltage.

The second parameter taken into account for the sizing of the control capacitor is by sensitivity. As explained above, once parasitic capacitances have been estimated, the only design-related parameter that sets the sensitivity is the control capacitance. If the sensitivity is too low, the detection of telomerase activity can be very difficult. Vice versa, if the sensitivity is too high the sensor response can saturate even with a small charge variation, thus being unusable.

The capacitive divider and the sensitivity constraint move in the opposite way, so a trade-off is needed: in fact, a bigger control capacitor means that the floating gate voltage is closer to the applied voltage but at the same time the sensitivity is subjected to a decrease. The opposite happens with a smaller capacitor: the sensitivity is high enough to detect telomerase activity but the floating gate voltage may be too low to switch on the device and set the operating point.

Two different capacitors have been chosen. Both have a capacitance per area of $4.4\,\mathrm{nF\,\mu m^{-2}}$, being implemented with the same double MIM structure. A square base unit with a side of $5\,\mu m$ has been used to increase matching. The small capacitor is implemented with a total of 25 base units, while the big capacitor contains 81 base units. Simulations have been performed to verify the impact of both statistical and process variations on the capacitive divider and on the sensitivity of the device. Results showed an average total capacitance of about $3.2\,pF$ and $10\,pF$ for the small and the big capacitor, respectively.

Sensitivity has been evaluated according to capacitances variation in the control capacitor due to process mismatch and statistical variations. Results are reported in Table 3.2: while negligible differences were produced by the statistical variations of capacitor size, as expected the two different sizes highly affected the sensitivity; in fact, sensitivity obtained with the small capacitor turns out to be three times larger than the one obtained with the big capacitor.

Cap size [μm^2]	$\Delta V_{TH} \pm SD$ [mV]
25x25	128.5 ± 2.8
45x45	42 ± 1

Table 3.2: Sensitivities for different control capacitors.

Threshold voltage variations are expressed in mV and refer to a charge variation of about $4.18 \times 10^{-14}\,C$, which is calculated on telomerase activity detection on a $66\,\mu m \times 66\,\mu m$ sensing area with a process efficiency β equal to 1 and a coverage factor σ_q of 100 DNA molecules per μm^2, which is consistent with the probe immobilization procedures reported in a previous CMFET chip [55]. Since it is difficult to precisely estimate the total charge induced on the floating gate, having two different sensitivities available is convenient and allows the detection of different levels of telomerase activity.

3.3 Layout design

Once a model for the CMFET sensor has been defined, the next step consisted in the design of the physical layout. As explained above, two different sizes of the control capacitor and two different CMFET structures imply the realization of four different layouts. The next section is subdivided into two main parts: in the former the layouts are illustrated, while in the latter a characterization of the sensor during simulated telomerase measurements is presented.

3.3.1 CMFET sensing unit layout design

To simulate the entire architecture and the design of the layout, the Cadence Virtuoso platform has been employed, which includes the ADE (Analog Design Environment) simulation environment and the Virtuoso Layout Suite. In

particular, the layout that are shown in this section have been exported from the Virtuoso Layout Suite XL.
The layout of the sensors include the NMOS-PMOS pair, the control capacitor and the matched NMOS and PMOS that are required for the implementation of the level shifter. All of the layouts include also the 66 µm × 66 µm sensing area.
The first and more standard implementation of the CMFET is the one described before as *"planar"* version, which is characterized by the control capacitor placed beside the sensing area and is depicted in Fig. 3.3.1. The sensing area occupies the

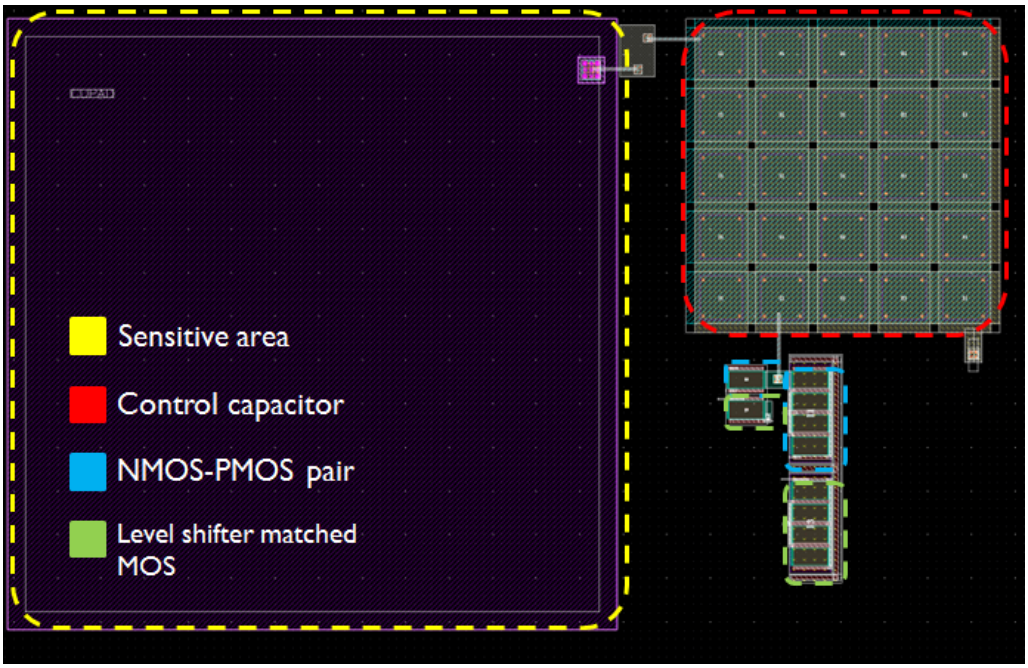

Figure 3.3.1: Standard planar version of the CMFET layout.

majority of the pixel area, and it is a single thick metal layer. The control capacitor is situated in the upper-right corner and is composed of 25 base units; it has a total capacitance of about 3 pF. The NMOS-PMOS pair is placed beside the control capacitor. Since the floating gate comprises the sensing area, the middle plate of the control capacitor and the gate of the NMOS and PMOS, the three elements are closely placed in the same area of the pixel, to reduce parasitic effects. Finally, the matched NMOS and PMOS required for the level shifter readout scheme are placed at the side of the NMOS-PMOS pair, to decrease process and statistical variations and thus increase the matching between the two.
A similar layout has been designed for the planar sensor with the larger capacitor.

The *"circuit-under-pad"* version of the sensor is illustrated in Fig. 3.3.2. The control capacitor is located in the top-right, under the sensing area. This has two main advantages: it reduces the coupling between the sensing area metal surface and the Si bulk and also decreases the area occupation, thus allowing a greater integration of the sensors. As in the above planar versions, the NMOS-PMOS pair and the matched transistor required for the level shifter are placed near the capacitor, to decrease parasitic effects and process variations.

In this version, all the switching logic can be fitted under the sensing area. This

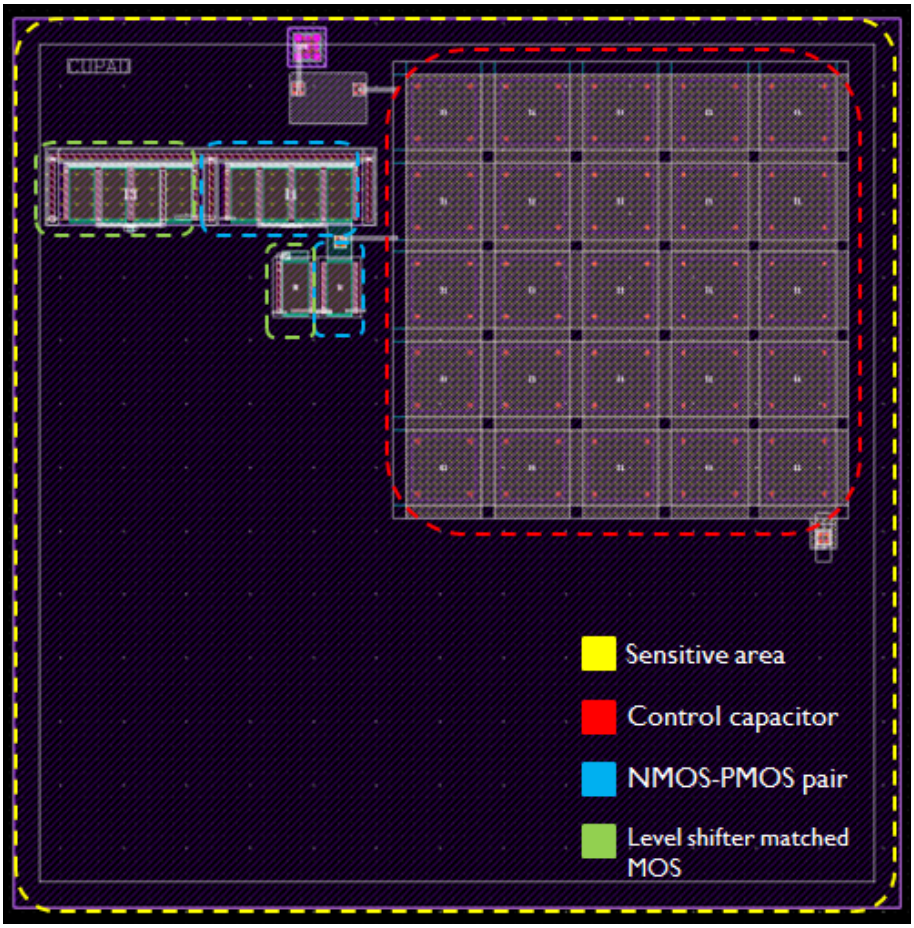

Figure 3.3.2: Circuit-under-pad version of the CMFET sensor with a 25 µm × 25 µm capacitor.

leads to an area occupation which depends on the sensing area size only. Therefore, with respect to the corresponding planar version, it is possible to almost double the number of sensors with the same area occupation. As before, a similar layout has been drawn for the larger capacitor version.

Finally, Fig. 3.3.3 shows the layout of the sensor with the addition of a DMOS switch for potentiostat usage. The DMOS increases the area occupation by a considerable amount, in exchange for the possibility to perform the electrochemical functionalization of the sensing area.

3.3.2 Sensor array

A complete cluster is illustrated in Fig. 3.3.4. The cluster contains 4 sensors and all the circuitry that allows the transduction and conversion: voltage and current readout schemes and an ADC are included in each cluster, so that each of them can function in parallel to other clusters.

As introduced in Chapter 2, clusters are organized in channels of 32 sensors each. This subdivision has been made to develop a subsequent microfluidic system which can brings solutions and reagents to the sensing areas.

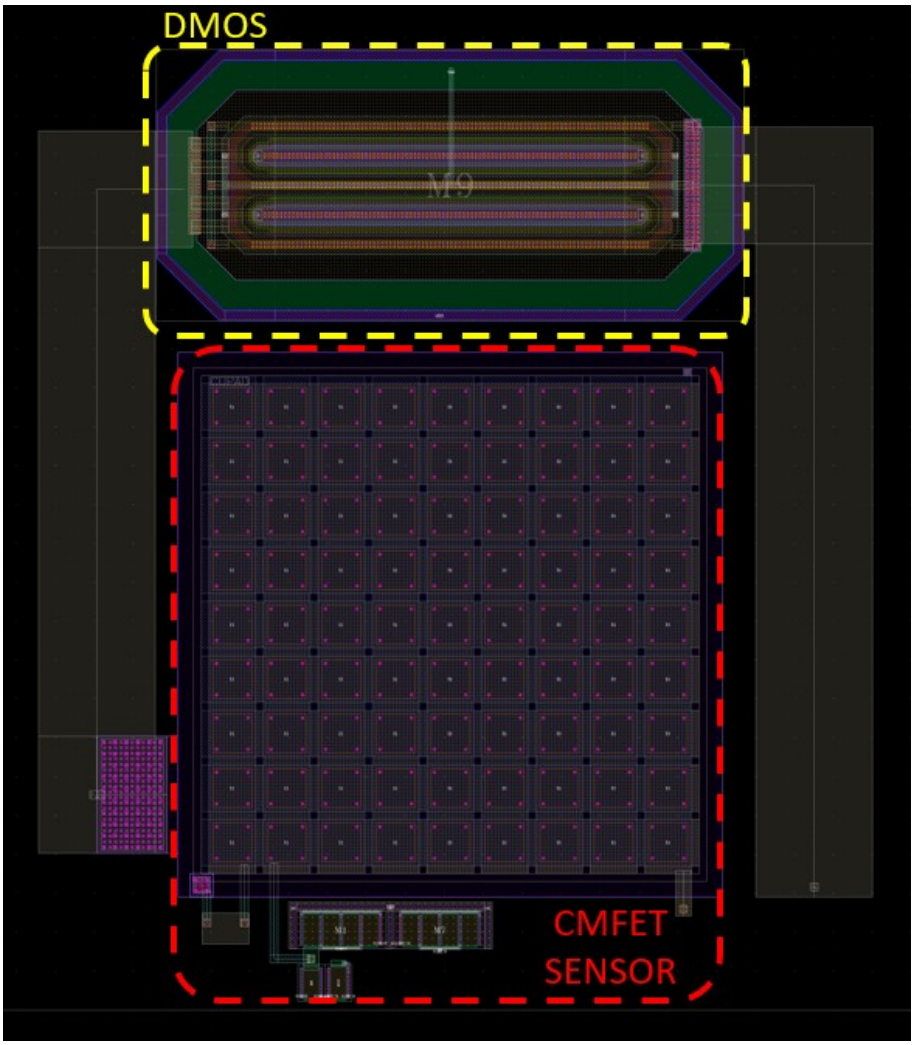

Figure 3.3.3: Sensor with DMOS for potentiostat usage.

The complete chip layout, as in Fig. 3.3.5, is made up of 32 channels. A single channel with 32 sensors is highlighted. The channels have been subdivided into two halves: the top half of the chip contains channels in which sensors have not been modified with the DMOS switch, thus they required an external potentiostat or a different functionalization procedure. The bottom half of the chip contains channels that can be used with the integrated potentiostat.

3.4 Simulation of sensor characterization during telomerase activity

In Chapter 2 the process necessary to perform telomerase detection measurements has been described. To summarize, three steps are required:

1. functionalization of the sensing area by immobilizing DNA probes;

2. addition of telomerase molecule to the solution, which causes the telomeres to

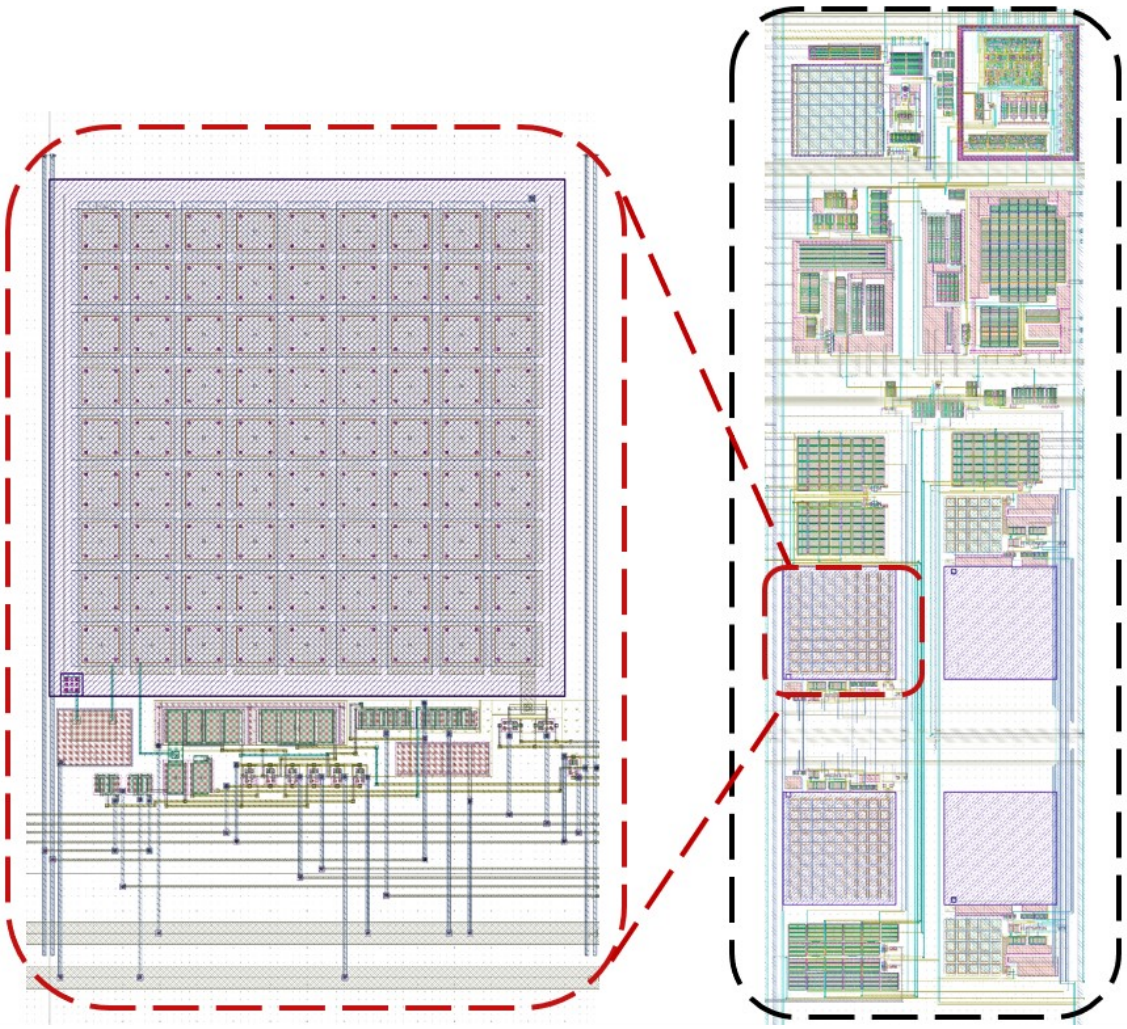

Figure 3.3.4: On the right, the layout of a cluster is shown. Each cluster is made up by 4 sensors (in the bottom part of the black box) and all the conversion circuitry which includes the level shifters, the current-reference circuit, the AD converter and the current-to-frequency converter (in the top part of the black box). A single sensor with the complete multiplexing logic is depicted in the magnified box. It includes the sensing area, the under-pad control capacitor, the CMFET MOSFET pair and the digital switches to select the conversion scheme.

elongate;

3. estimation of the telomeric elongation.

The process involves both charge increases and decreases, so the sensor has to be able to detect variations in both directions.
Currently it is difficult to estimate telomerase efficiency β and coverage factor σ_q, since they are highly variable process-dependent parameters, but a rough estimation can be done. As can be expected, in a real experiment it is unlikely that telomerase efficiency reaches 100%; a plausible value can be included between 10% and 60%, which means that telomerase will elongate about 10 to 60% of the immobilized probes.

The coverage factor is also a variable term: the estimated density of DNA molecules varies in a range from 10 molecules per µm^2 to 1000 molecules per µm^2.
Figure 3.4.1(a) shows the variation of the effective threshold voltage for a N-type sensor, while Fig. 3.4.1(b) shows the same variation but for a P-type sensor. In the x-axis the parameter β sweeps from 0 to 1, which are the lower and upper boundaries for telomerase efficiency: the former means that telomerase did not elongate any probe, while the latter indicates the elongation of all the probes. An average coverage factor σ_q of 100 DNA probes per µm^2 was chosen, and it was hypothesized that telomerase elongates the probes by a single telomeric sequence, thus carrying the charge of six bases per probe.

While the induced charge, that for the above-mentioned conditions and for $\beta = 1$ equals to 4.2×10^{-15} C, is the same in both simulations, it is clear that a different sensibility can be achieved with the two sizes of capacitor. As expected, the sensor with the small capacitor has a bigger threshold voltage shift (about 120 mV) if compared with the big capacitor sensor (whose threshold voltage shifts by 40 mV). The results obtained through this simulation indicate that telomerase activity detection can be performed by using this approach, since even small variations of charge in the order of fC produce a considerable threshold voltage shift.
However, if the variability of the parameter σ is taken into account, a threshold voltage variation spanning from a few mV to about 1 V can be expected.

Moreover, the threshold voltage shift produced by the elongation of telomeres, as in Fig. 3.4.2, occurs only during the last step of the measurement protocol. In fact, a significant charge variation is also present after the surface functionalization, due to the immobilization of the probes. This causes a noticeable threshold voltage shift that, for the above condition of $\sigma = 100$ molecules/µm^2, can be quantified as about 600 mV. Therefore, it has to be pointed out that during the last step of the measurement protocol the threshold voltage is not equal to the intrinsic threshold voltage of the device, but has already been shifted by the charge induced by the probes.
The additional shift of the threshold voltage caused by the probes has some repercussion on the readout system: in fact, the overall sensing range of the readout scheme has to take into consideration not only the threshold voltage variation induced by telomerase activity, but also needs to be wide enough to detect aforementioned variations after the offset shift caused by surface functionalization.

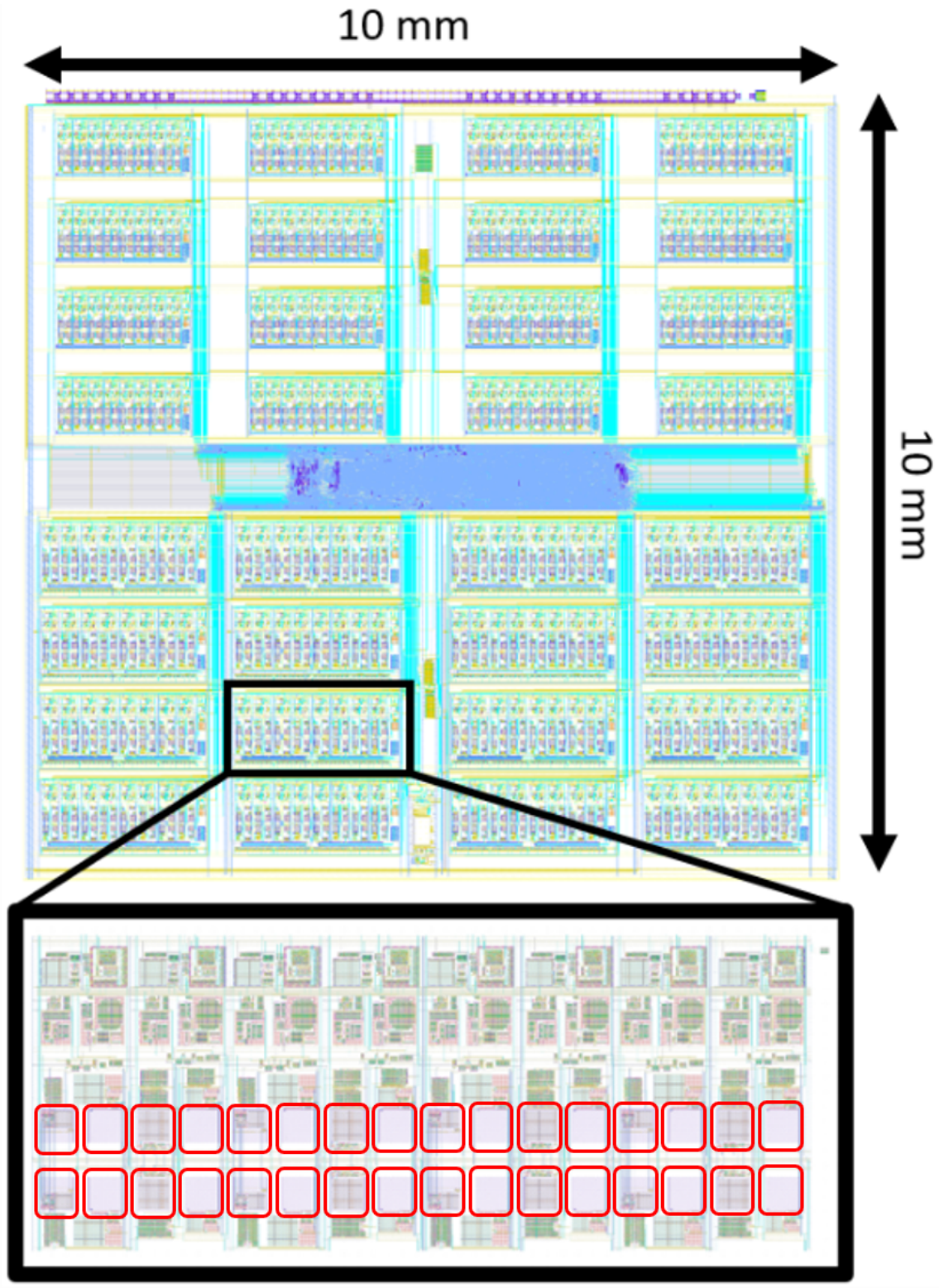

Figure 3.3.5: Layout of the complete chip. The top hhalf of the chip comprises channel without the potentiostat switches. In the bottom half, all channels include the logic to allow potentiostat operations. The digital logic is situated between the two halves of sensor channels. In the magnified box, a single channel is depicted. The sensing areas are highlighted in red.

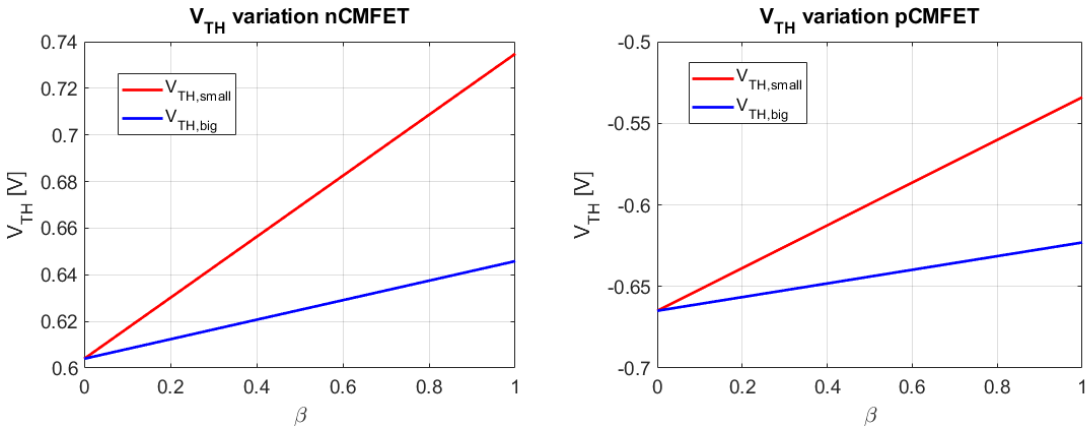

(a) V_{TH} variation for NMOS.

(b) V_{TH} variation for PMOS.

Figure 3.4.1: Effective threshold voltage variation as a function of telomerase efficiency β. The plots show that, for both N-type and P-type CMFET, the threshold voltage variation is inversely proportional to the device capacitances, as reported in Eq. 3.2. By selecting a different control capacitor (which is the main contribution to the overall capacitance), sensitivity can be adapted to the specific application.

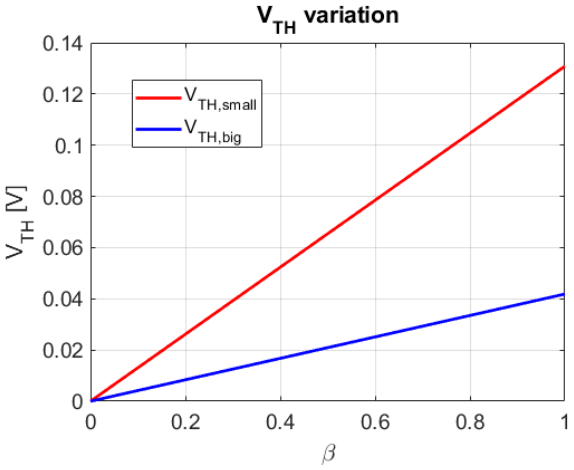

Figure 3.4.2: ΔV_{TH} induced by telomeres elongation.

4 | Readout schemes

The designed LoC offers the possibility to select three different readout schemes, the voltage scheme, the current scheme and the current-to-frequency converter. In this Chapter all the readout schemes are analyzed. In addition, the temperature sensor and the potentiostat are addressed.

4.1 Level shifter

The level shifter readout scheme is used to translate a variation of effective threshold voltage of the CMFET sensor into a variation of the drain voltage of a diode-connected matched MOS of the same type.
A basic schematic of the circuit used for the N-type level shifter is shown in Fig. 4.1.1. The sensing unit M1, i.e. the CMFET, is paired with the matched transistor M2. The circuit is biased through the current sinked from M3 and M4: one (M4) sets the current on the matched transistor branch (I_2), while the other (M3) sets the total current on the level shifter (I_1). The output voltage V_{OUT} is measured at the drain of M4.

In the case of the N-type level shifter, V_{OUT} can be expressed as a function of the effective threshold voltage and the currents in the level shifter:

$$V_{OUT,N} = V_{FG} - \Delta V_{TH} + k\left(\sqrt{I_2} - \sqrt{I_1 - I_2}\right) \tag{4.1}$$

in which V_{FG} is the voltage on the floating gate of the CMFET, ΔV_{TH} is the variation of the effective threshold voltage of the CMFET and the term k is equal to $\sqrt{\frac{2}{\mu_n C_{OX} \frac{W}{L}}}$ and only depends on process and design parameters. Finally, currents I_1 and I_2 are those generated by the N-type and P-type current mirrors.
For the PMOS the complementary relationship is valid:

$$V_{OUT,P} = V_{FG} + \Delta V_{TH} - k\left(\sqrt{I_2} - \sqrt{I_1 - I_2}\right) \tag{4.2}$$

Since the current ratio $\frac{I_1}{I_2}$ has been chosen to be equal to 2, both V_{OUT} expressions can be simplified to:

$$V_{OUT,N} = V_{FG} - \Delta V_{TH} \tag{4.3}$$

$$V_{OUT,P} = V_{FG} + \Delta V_{TH} \tag{4.4}$$

As can be seen from Eq. (4.3) and Eq. (4.4), it is possible to directly read out the effective threshold voltage variation from the output of the level shifter, thus

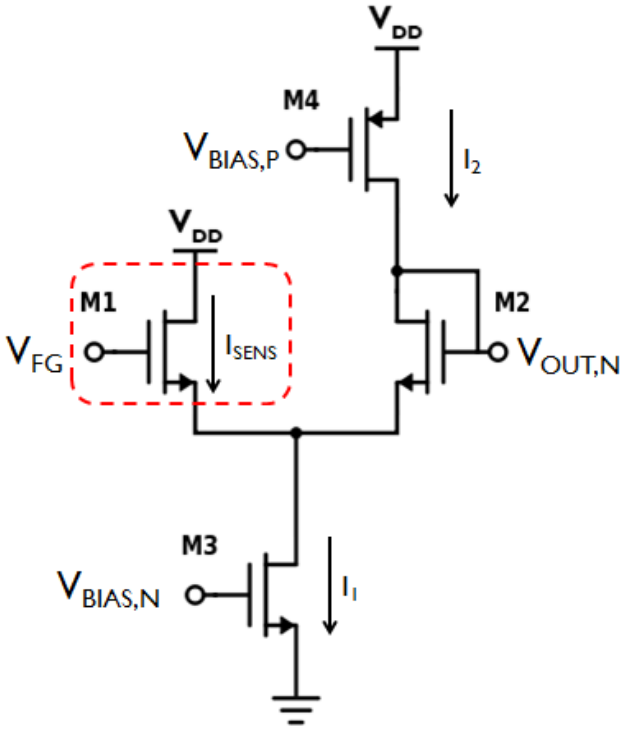

Figure 4.1.1: Schematic of the N-type level shifter. The highlighted MOS M1 represents the CMFET, while M2 is the matched transistor. MOS M3 and M4 are current mirrors which set the I_1 and I_2 currents, respectively.

estimating the charge induced on the floating gate.
As explained before, a positive charge on the sensing area causes the PMOS to go into cut-off region and the NMOS into saturation, while a negative charge has the opposite effect. For this reason, to extend the sensing range and guarantee that at least one MOS is switched on at any time, the NMOS-PMOS pair is used as a sensing unit. The current values in this operating point are $I_{SENS} = I_2 = 1\,\mu A$ and $I_1 = 2\,\mu A$.
The sensor's can be biased by applying a voltage equal to $V_{DD}/2 = 0.9V$ on the control gate, to keep both the n-type and the p-type CMFET in saturation region at the same time. This configuration can be used to sense charges with unknown sign or small variations around the center of the measurement range. When the threshold voltage varies by less then 0.8 V in both directions, the level shifter output varies as a linear function of the effective threshold voltage variation ΔV_{TH}. This allows to obtain a linear output range of 1.6 V as depicted in Fig. 4.1.2, thus doubling the output range with respect to the single NMOS/PMOS transistor.
If the charge variation causes a shift of the effective threshold voltage greater than 0.8 V in any direction, one of the MOS saturates and the other exits from saturation region, thus the circuit does not operate as described in Eq. (4.3) and (4.4). To overcome this problem, the level shifter range can be tuned according to the charge variation that is detected: it is possible to shift the entire range by applying a different control gate voltage, comprised between 0 V and 1.8 V, thus achieving an

extended range that covers threshold voltage variation between $-1.7\,\mathrm{V}$ and $1.7\,\mathrm{V}$. The range obtained by using the $V_{DD}/2$ biasing voltages is plotted in Fig. 4.1.2; the y axis represents the variation of the output voltage (the drain voltage of the matched transistor) as a function of the variation of the effective threshold voltage of the CMFET.

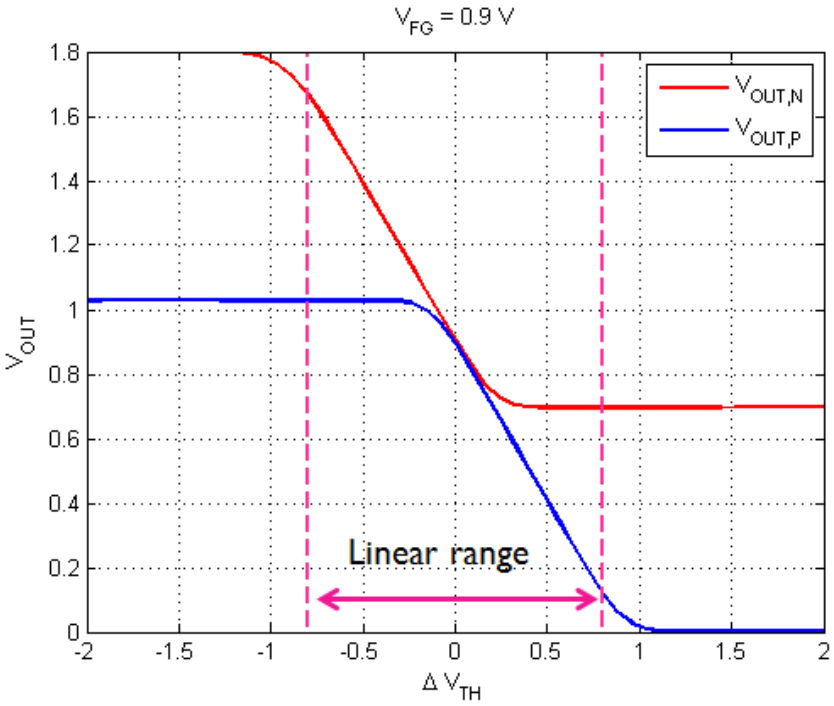

Figure 4.1.2: Level shifter output for both NMOS and PMOS, with $V_{FG} = 0.9\,\mathrm{V}$.

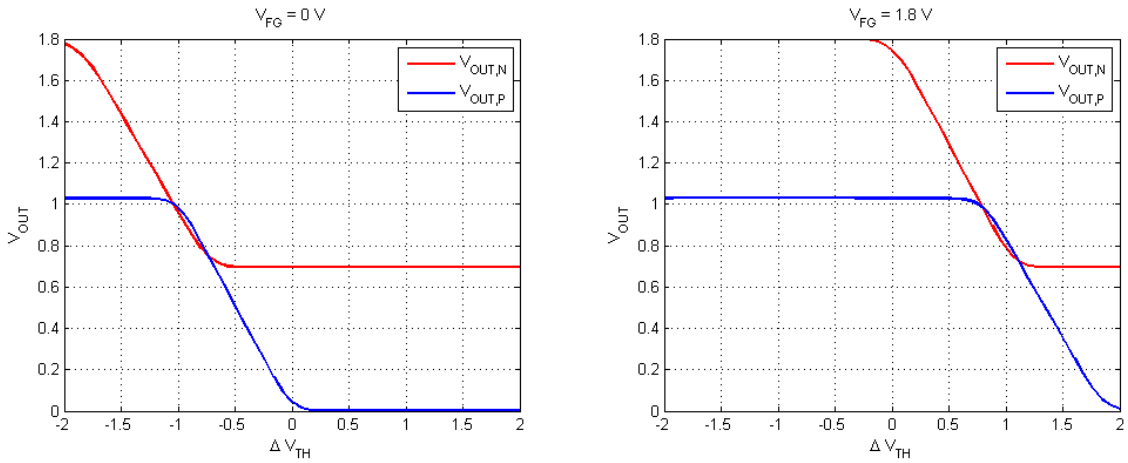

Figure 4.1.3: Level shifter output for both NMOS and PMOS, with $V_{FG} = 0\,\mathrm{V}$ and $V_{FG} = 1.8\,\mathrm{V}$ respectively. With respect to Fig. 4.1.2, the measuring range has been translated towards more negative (left plot) or more positive (right plot) voltages.

Figure 4.1.3 shows two different operating points used to extend the level shifter sensing range. The ranges are obtained by applying $0\,\mathrm{V}$ and $1.8\,\mathrm{V}$ respectively on

the control capacitor and can be used when there is a larger positive or negative charge on the sensing area and the outputs of the standard configuration saturate. By applying the adequate control gate voltage during the measurement process it is possible to detect threshold voltage variation from $-1.7\,\mathrm{V}$ to $1.7\,\mathrm{V}$, obtaining an overall range of $3.4\,\mathrm{V}$. As previously mentioned, telomerase activity carries a charge that induces threshold voltage variations that span from few to hundreds of mV, depending on parameters such as β and σ. The sensing range obtained with this readout is thus suitable to perform telomerase activity detection while also taking into consideration the threshold voltage shift induced by the immobilized probes.

4.2 Current reference circuit

An alternative readout circuit is shown in Fig. 4.2.1a for the N-type CMFET. The complementary scheme is used for the P-type CMFET. In this scheme, the NMOS transistor of the sensing unit, here named M5, is biased in its linear operating region and acts as a variable resistor in a β multiplier reference circuit. For this reason, the output current of the β multiplier is a function of the threshold voltage of the CMFET. A simulation of this circuit is shown in Fig. 4.2.1b. A sensitivity of $175\,\mathrm{nA}/100\,\mathrm{mV}$ was obtained in a linear range of $3.1\,\mathrm{V}$.

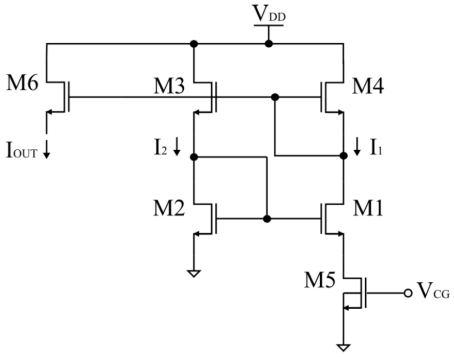

(a) Current reference schematic.

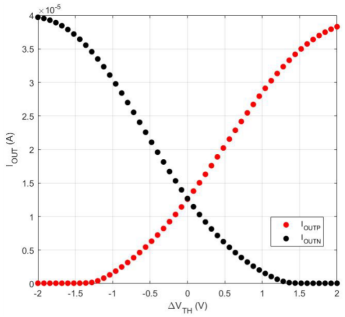

(b) Output current as a function of threshold voltage variation.

Figure 4.2.1: Current reference readout scheme.

4.3 Analog-to-digital converter

A dual-slope ADC was chosen, in order to be able to perform the analog-to-digital conversion of both voltages (from the level shifter) and currents (from the current reference circuit).
The working principle of the circuit, shown in Fig. 4.3.1, relies on the ratio of the time required to discharge two capacitances C_1 and C_2. During the first reset phase, control signal S_1 and S_2 disconnect the respective switch while both capacitances are charged to the same voltage by a reset signal. In the second phase, the capacitance C_1 is connected to I_{SENS}, which is the output of the level shifter or the current reference, depending on the chosen readout method. The voltage V_+ then decreases

linearly by a value given by $\frac{I_{SENS}}{C_1}\Delta T_1$. In the third phase, C_1 is disconnected from its current source and C_2 is connected to a reference current I_{REF}. The voltage V_- across C_2 decreases by $\frac{I_{REF}}{C_2}\Delta T_2$. A comparator connected to both capacitors detects when the two voltages are equal, that is:

$$\Delta T_1 + \Delta T_2 = (1 + \frac{C_2}{C_1}\frac{I_{SENS}}{I_{REF}})\Delta T_1 \tag{4.5}$$

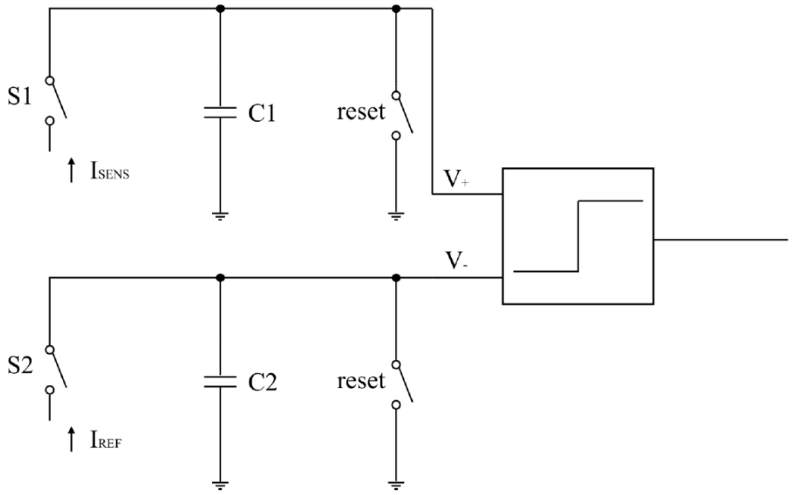

Figure 4.3.1: Schematic representation of the implemented dual-slope ADC.

With a capacitance ratio $M = \frac{C_2}{C_1}$ and a current ratio $N = \frac{I_{SENS}}{I_{REF}}$, the initial time interval ΔT_1 is amplified by a factor $(1 + M \cdot N)$ which can be further measured employing a simple counter for the final time-to-digital conversion. A clock frequency of 10 MHz, $M = 100$ and $I_{REF} = 1\,\mu A$ were used. Figure 4.3.2 shows in more detail what happens during the beginning of the conversion: both capacitors are charged until they have the same voltage (1.6 V) during the reset phase and then the conversion starts by connecting C_1 to the current source. In a fixed amount of time ΔT_1 capacitor C_1 discharges to about 1.4 V. After that, capacitor C_1 is kept floating and capacitor C_2 is connected to a known current source and starts discharging (comparation phase) as in Fig. 4.3.2. When both voltages are equal, the comparator activates and stops the counter, which has now stored a value corresponding to time ΔT_2. By using Equation 4.5 the unknown value of I_{SENS} can be calculated. In the case of current measurements a resolution of 38.9 nA was determined. Such a behavior is related to the leakage current which decreases the voltage across C_1, thus affecting the converter performances. In the case of voltage conversion a final resolution of 100 µV was achieved.

4.4 Current-starved ring oscillator

The output current of the current reference circuit can be also used to bias a current-starved ring oscillator and then translated into a frequency. Then, a simple counter can be used for the final time-to-digital conversion. A five-stages current-starved

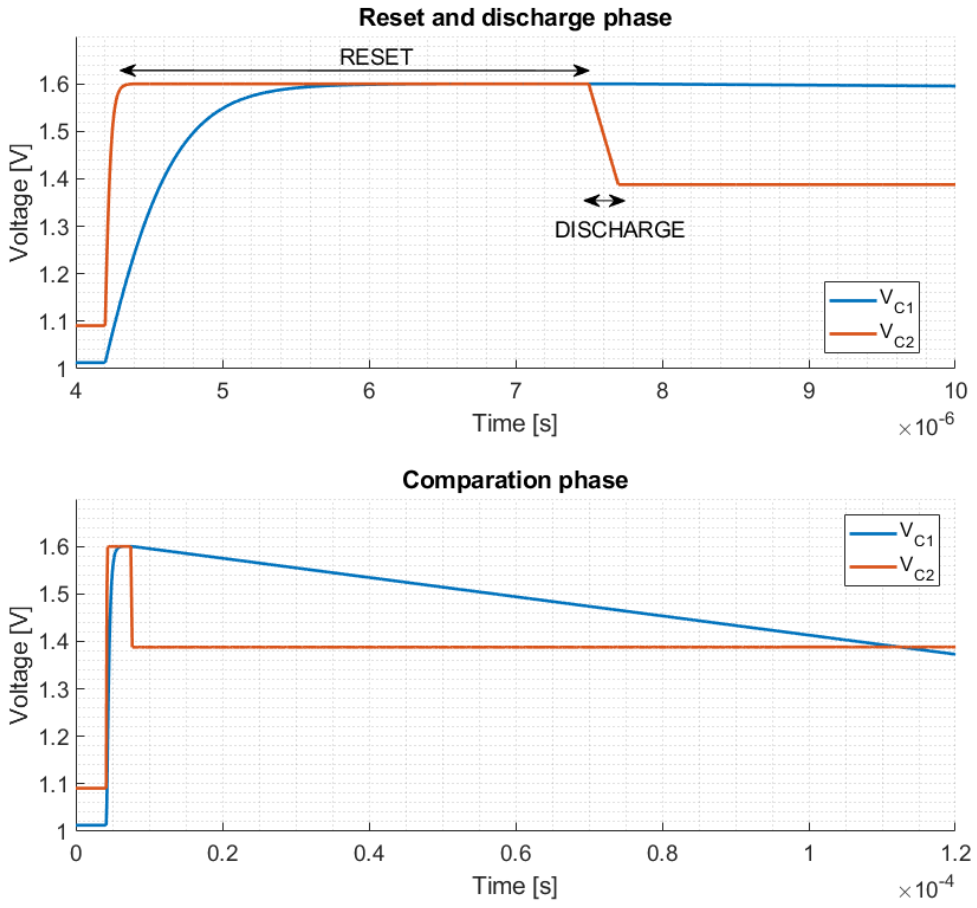

Figure 4.3.2: Ring oscillator circuit

ring oscillator was employed as an alternative readout circuit. In a standard ring oscillator, the oscillating frequency depends upon the current I_S which flows on the inverter and can be expressed as:

$$f_{OSC} = \frac{I_S}{NV_{DD}C_{TOT}} \tag{4.6}$$

where V_{DD} is the supply voltage, C_{TOT} is the total output capacitance of the loop and N is the number of stages. As stated in Eq. 4.6, it is possible to tune the oscillator frequency through the current I_S. Figure 4.4.1 shows the schematic of the employed circuit, where I_{IN} is the current generated by the current reference circuit and depends on the threshold voltage of the sensor. The output frequency is linear with the variation of the threshold voltage for a range of 2.2 V of each sensor type, thus achieving an overall linearity range of 2.8 V. A sensitivity of 0.33 MHz/100 mV has been achieved.

Figure 4.4.2 shows a simulation of the ring oscillator in which the parameter β in Eq. 3.3 has been changed from 0 to 1. In the second case, the current generated by the sensor is larger and the oscillator produces a higher oscillating frequency.

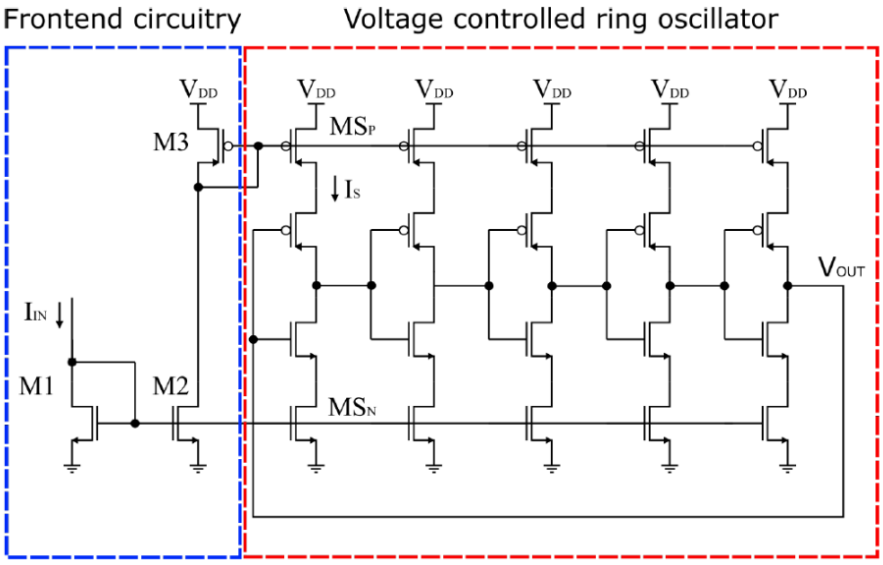

Figure 4.4.1: Ring oscillator circuit

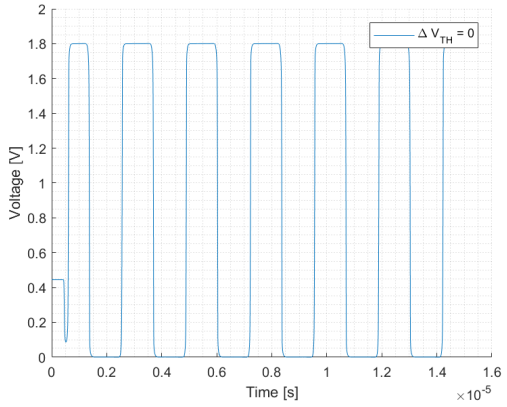

(a) Ring oscillator with $\beta = 0$.

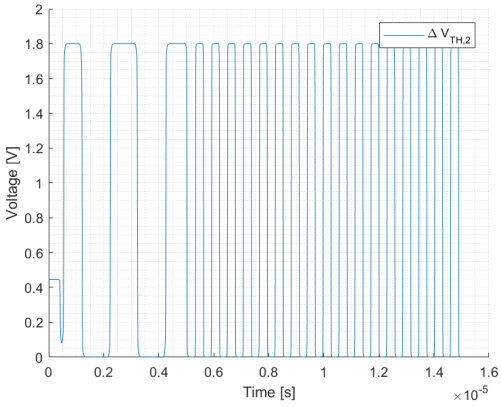

(b) Ring oscillator with $\beta = 1$.

Figure 4.4.2: Simulation of the ring oscillator for different β values.

4.5 Temperature sensor

Temperature control is a critical factor in order to increase the catalytic activity of telomerase [57]. Therefore, a temperature sensor was implemented in order to monitor this parameter. In particular, a proportional to absolute temperature (PTAT) sensor was employed and it is shown in Fig. 4.5.1a. The PTAT voltage is obtained by biasing two bipolar transistors (Q_1 and Q_2), with different areas ($A_2 = n \cdot A_1$), with the same current. In such conditions, assuming V_1 and V_2 potentials are at the same level, the drain currents of M_1 and M_2 are equal to:

$$I_{DS1} = I_{DS2} = \frac{k \cdot T}{q} \frac{\ln n}{R_1} \tag{4.7}$$

where k is the Boltzmann's constant, q the electron charge, T the absolute temperature and n the ration between A_2 and A_1. Consequently, the output

voltage can be expressed as follows:

$$V_{PTAT} = \frac{W_5}{W_4}\frac{k \cdot T}{q}\frac{\ln n \cdot R_2}{R_1} \tag{4.8}$$

where R_1 and R_2 are the resistors in the schematic in Fig. 4.5.1a and W_4, W_5 are the width of MOS M4 and M5. Simulation results, reported in Fig. 4.5.1b, show the linear dependence of the PTAT output voltage with respect to the temperature. A resolution of 9.49 mV/°C was achieved, thus leading to a final resolution of the system of 0.1 °C.

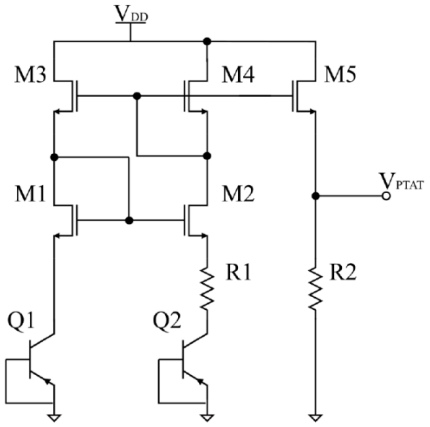

(a) Schematic PTAT circuit.

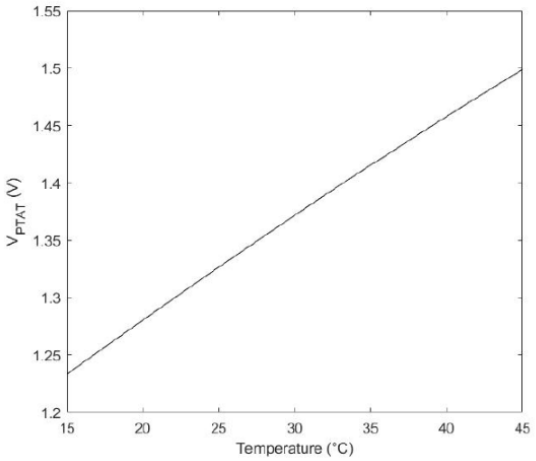

(b) Output voltage as a function of temperature.

Figure 4.5.1: Implemented PTAT circuit and simulation.

4.6 Potentiostat

The large scale of integration offered by a standard CMOS process allows an increasingly large number of sensing units to be implemented in a single chip; however, to obtain multiplexing capabilities, it is required to functionalize each sensor independently. A good alternative to common functionalization techniques, such as Self Assembled Monolayers (SAM), is the electrochemical modification of the electrodes, which allows a more stable functionalization of selected electrodes with the application of a potential through a potentiostat. To allow the use of a potentiostat, the standard CMFET structure has been modified with the addition of a switch that enables or disables the potentiostat operation. While floating gate isolation was not possible with standard MOS switches due to leakage (resulting in the fast discharge of the control capacitor), by using Double-diffused MOS (DMOS) and Isolated MOS as switches it was possible to hold the floating gate at a constant potential for a sufficient time. Moreover, due to the large number of sensors and their small dimensions, employing an external potentiostat may become a complicated task. To address this problem, an integrated two-electrode

potentiostat was designed, with single sensor addressing capabilities, suitable for the functionalization of the sensing areas of a CMFET-based DNA biosensor. The working principle of the potentiostat is depicted in Figure 4.6.1: an operational amplifier with a NMOS in its feedback loop is used to provide a current in the range between 1 and 15 mA while being able to keep a constant potential difference of at least 1 V across the electrolytic cell, here modeled as a parallel $R_{CELL} - C_{CELL}$ impedance. A programmable current mirror was also used to output a current proportional to that sunk from the potentiostat and perform time-to-digital on-chip conversion with the same methods described above.

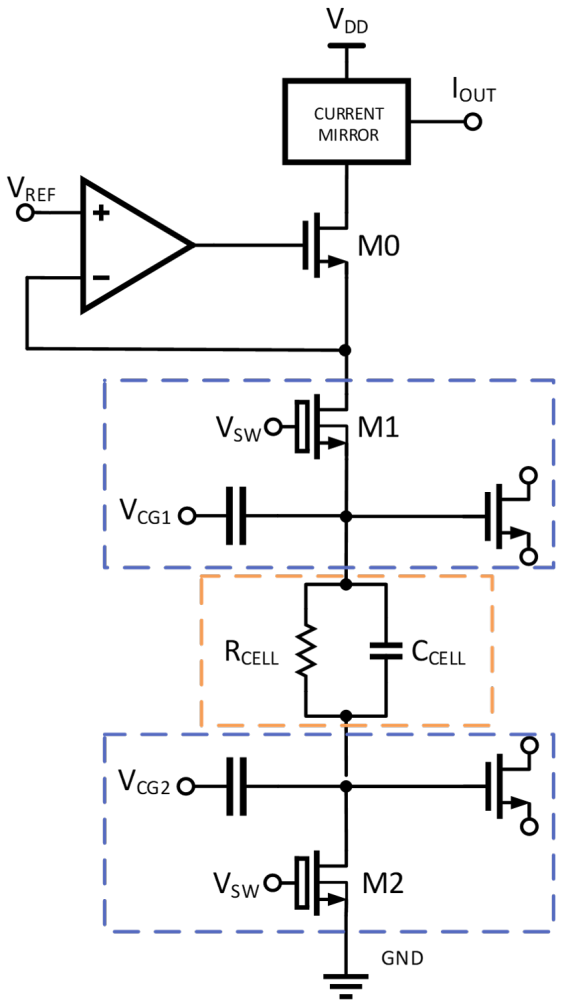

Figure 4.6.1: Implementation of the potentiostat: two CMFET sensors are highlighted in the blue boxes, one connected to the potentiostat and the other connected to ground through DMOS switches. Between the electrodes, an electrolytic cell is modeled with a parallel $R_{CELL} - C_{CELL}$ impedance.

4.6.1 Self-calibrating current mirror

The complete architecture of the integrated potentiostat is illustrated in Fig. 4.6.3. The potentiostat current is mirrored and divided through a two-stages

programmable current mirror before being converted into a 16-bit data by the dual-slope ADC. However, due to the high variability of biochemical processes, a current mirror with a wide input range is required. For this reason, the current mirror proposed in [58] has been chosen (Fig. 4.6.2). With respect to a standard cascode current mirror, the level-shifted low-voltage cascode current mirror has the advantages of having an improved input range due to the MOS M_5, biased in sub-threshold region and used as a level shifter.

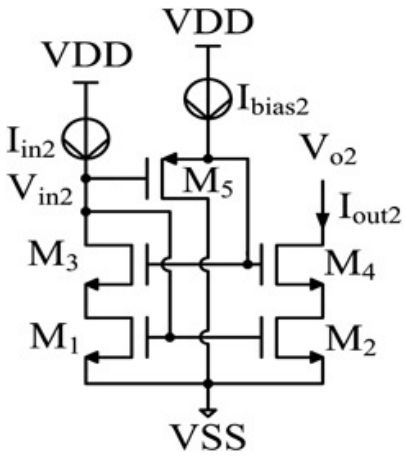

Figure 4.6.2: Level-shifted low-voltage cascode current mirror from [58]. Mirror transistors M_1, M_2 have the same aspect ratio as cascode transistors M_3, M_4. M_5 is operated in sub-threshold region, while M_1 and M_3 can operate in sub-threshold region for low input currents and in saturation region for high input currents.

Moreover, digital programmability has been added to further increase the dynamic range. To perform the self-calibration of the current mirror, a current comparator and digital logic have been included. The current comparator is based on the standard Traff comparator as in [59]. However, the input stage has been modified to compare the input current I_{MIRR} with a reference current, and a buffer has been added to the output to obtain a clean digital signal. A simple diode-connected NMOS, properly sized, has been used to generate the reference current, which is then mirrored into the comparator input. If I_{MIRR} is larger than the reference current, the output has a high logic value, else it has a low logic value.

Furthermore, a calibration algorithm has been implemented and is presented in Algorithm 1. The output of the current comparator *out_comp* is used by the digital logic to decide if the current mirror range has to be increased or not; to avoid errors given by fluctuations, the previous value of the comparator (*out_comp_reg*) is also used. The 16-bits output *en_mirr* constitute a thermometer code, which selects the number of instances at the input and output of the current mirror, to change the gain. The overall gain can be programmed between $2 \cdot 10^{-3}$ and 10. This allows the measurements of current ranging from hundreds of nanoamperes to milliamperes.

The complete layout of the potentiostat is shown in Fig. 4.6.5 and occupies an area of 960x300 μm^2.

A post-layout simulation of the self-calibrating current mirror is shown in Fig. 4.6.6: I_{pot} is the current provided by the potentiostat, I_{out} is the current output

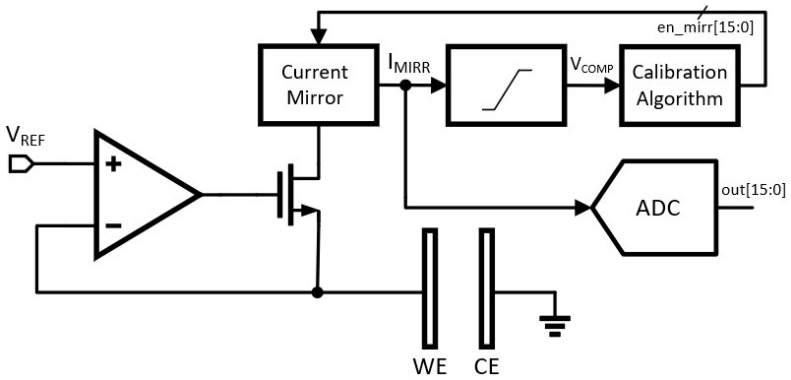

Figure 4.6.3: Schematic of the integrated potentiostat.

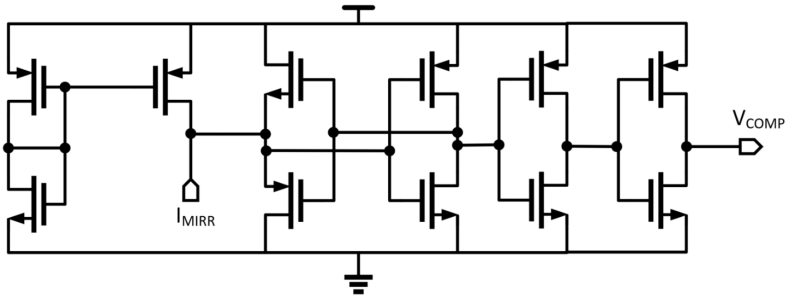

Figure 4.6.4: Schematic of the current comparator.

from the current mirror, $START$ and $OUTCOMP$ are digital signals used for the calibration. In this simulation, the potentiostat is trying to provide a current of about 11 mA, but the current mirror is not able to sink it so it causes a large voltage drop and the NMOS at the output of the OTA is not able to provide all the current. The output of the current comparator is high, so the input instances of the current mirror are increased, causing a smaller voltage drop on the mirror and a larger available drain-source voltage for the NMOS. In the I_{pot} box in Fig. 4.6.6 it can be seen that this process continues until $3.2 \cdot 10^{-4}$ s, when the potentiostat current reaches a stable value (i.e. when the NMOS is able to conduct all the current). The calibration process continues until the current at the output of the current mirror

Algorithm 1: Current mirror calibration

```
Input  : out_comp
Output : en_mirr
initialization;
while out_comp_reg OR out_comp ≠ 0 do
    out_comp_reg = out_comp;
    if out_comp then
        enable_mirr[i]=1;
    end
    wait for next comparation;
end
```

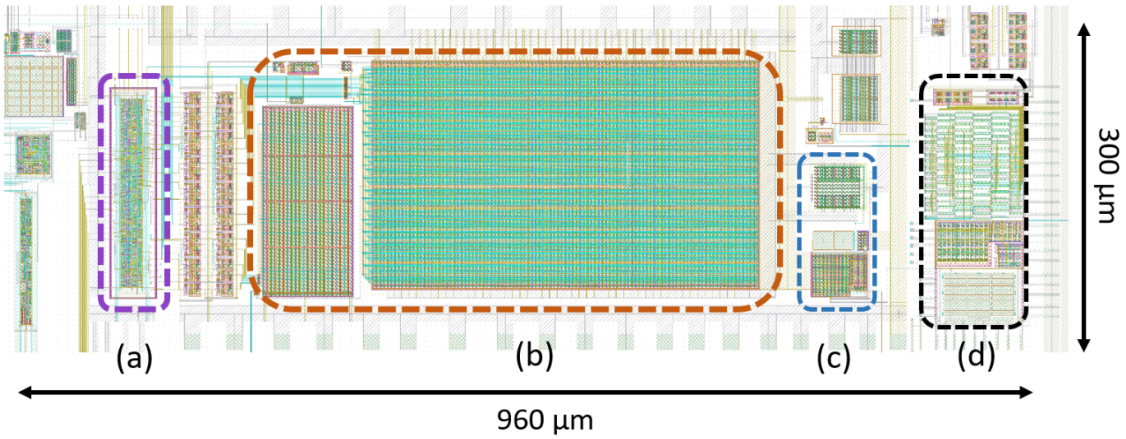

Figure 4.6.5: Complete layout of the potentiostat. (a) Digital logic. (b) Current mirror. (c) Amplifier and NMOS. (d) ADC.

is suitable for the ADC, which works best with a maximum current of 40 µA. The original current value can be reconstructed by looking at the mirror configuration bits, which are related to the overall gain.

4.7 Results

Post-layout, chip-level simulations of the complete chip have been performed to test the readout schemes and the digital control logic. Some results are shown in Fig. 4.7.1. Analog signals are plotted in the upper half, while digital signals are plotted in the lower half. The simulation shows the complete read-out path, from the sensor to the SPI bus which sends data off-chip and was obtained by addressing 2 different sensors ($Sens1$ and $Sens2$) located in two different cluster and channels of the chip. During the initial reset phase, both capacitors $C_{1,1}$ and $C_{1,2}$ of each addressed cluster and the reference capacitor C_2 are connected to a reference voltage equal to $1.6V$. Then, capacitors $C_{1,1}$ and $C_{1,2}$ are connected to the level shifter and pre-charged to the level shifter output voltage. Next, the conversion begins: the external C_2 capacitor is discharged by a known reference current I_{REF}, while counters in each cluster start counting. Comparators in each addressed cluster i output a digital end-of-conversion (EOC) signal when $V_{ref} < V_{sens,i}$, thus stopping the counters.

Table 4.1: Number of devices on chip

Device	MOS	DMOS	BJT	Capacitor	Resistor
#	1,714,141	1,664	640	68,972	2,716

When all active clusters have completed the conversion process, data are sent off-chip with a SPI protocol; the MISO (master in, slave out, i.e. the data stream sent from the chip to the controller device) bus is shown in Fig. 4.7.1. In particular, the following hexadecimal byte sequence is sent: 02 00 02 6f 01 01 dd. The first

byte contains information about the number of active clusters: two clusters have been selected for this simulation. Then, for each cluster, three bytes are sent: the first indicates the identification number of the cluster (00 and 01 for clusters 0 and 1 respectively), the other two bytes constitute the output value of the measurement, saved from the ADC and stored (026f for the first cluster, 01dd for the second cluster). Continuous data acquisition can be performed: when a conversion ends, data are sent through SPI; meanwhile, a new conversion can start.

The proposed device, fully designed to the layout level, represents a complete platform for telomerase activity detection. It integrates into a single device all the components needed to realize a fully autonomous lab-on-chip, including not only the biosensing device but also the overall signal chain until A/D conversion. Moreover, it includes temperature sensors and heater to properly set the temperature in within the enzyme operating range. Finally, it includes a potentiostat to exploit electrochemistry to functionalize sensors. The high level of integration of CMOS process allowed to integrate all this blocks altogether with 1024 sensing units into a single device. Post-layout simulations performed on the complete chip are provided, and considering that the sensing principle has been proved in [54], they represent a good estimation of the final device performances.

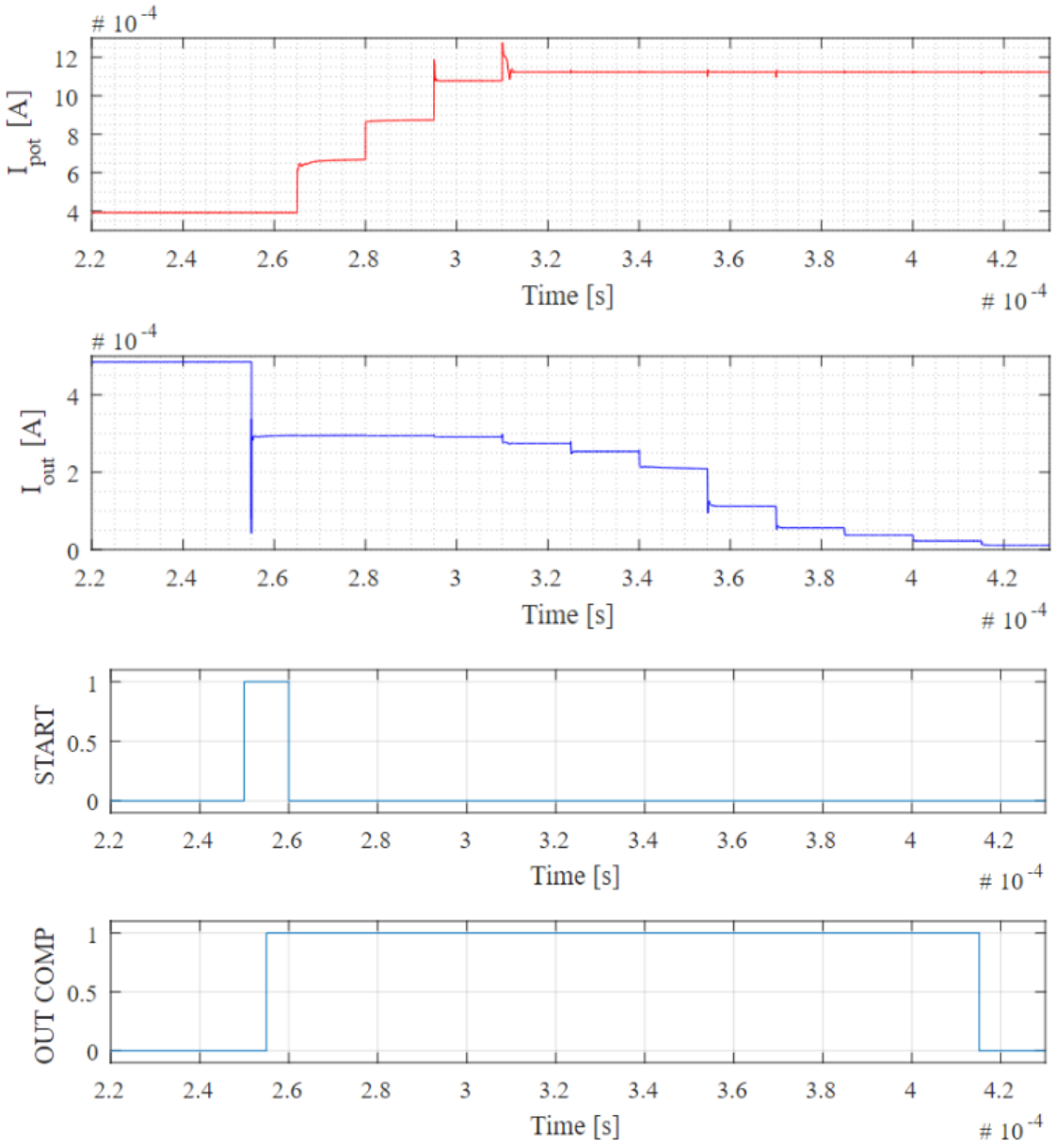

Figure 4.6.6: Implemented PTAT circuit and simulation. The first and second plots show the I_{pot} current generated by the potentiostat and the I_{out} current from the current mirror output. The third and fourth plot show the digital signal that starts the calibration procedure ($START$) and the output of the current comparator (OUT_{COMP}), which is kept at a logical level 1 until the calibration is complete.

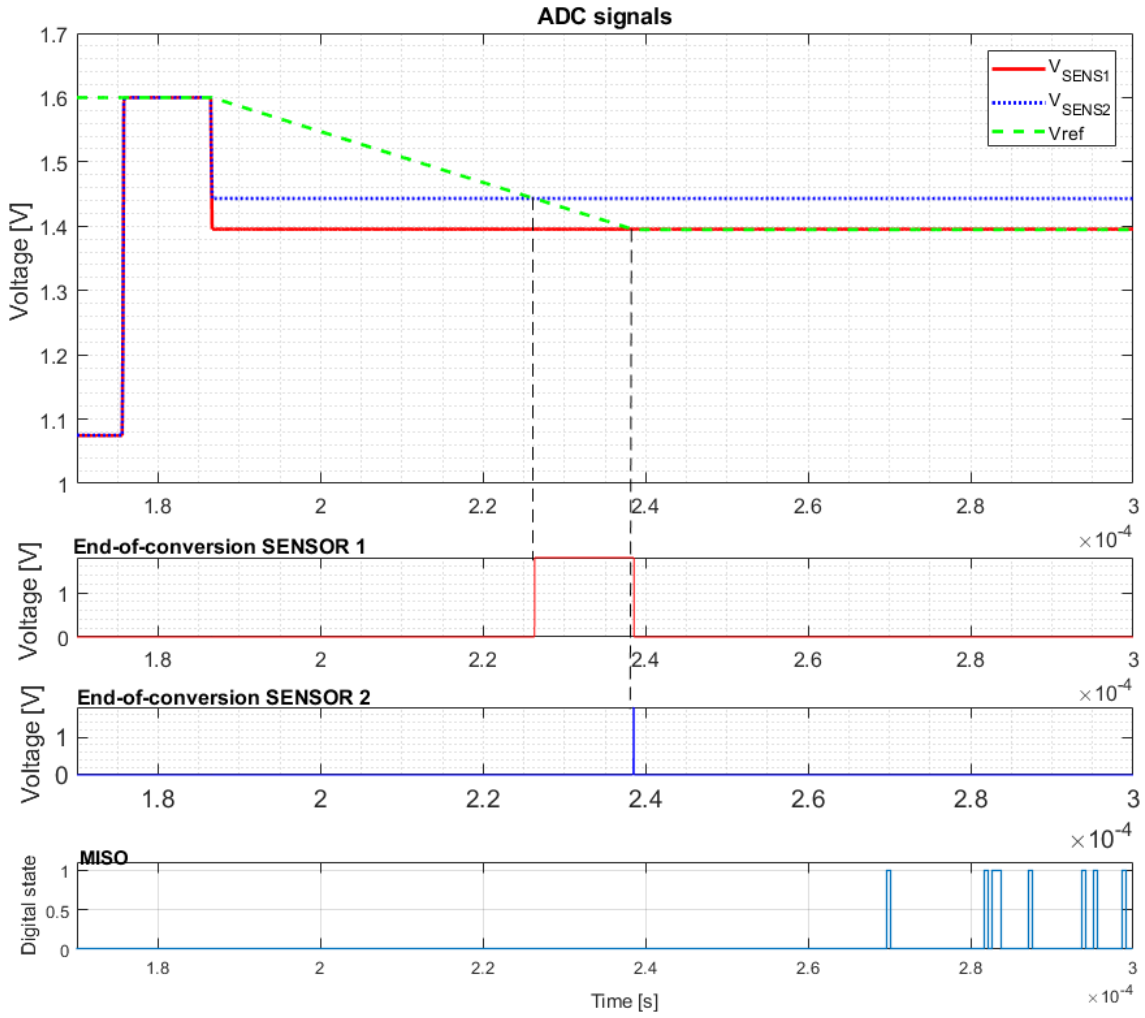

Figure 4.7.1: In the "ADC signals" box, the output voltages of two sensors V_{SENS1} and V_{SENS2} are plotted, together with the ADC capacitor reference voltage V_{ref}, which progressively discharges. When the ADC comparator detects that the sensor's output and the V_{ref} are equals, an end-of-conversion (EoC) signal is set to 1 (shown in the second and third boxes for the two sensors). Once the conversion is completed for all sensors, data is saved and then sent out through SPI protocol (the MISO wire is shown in the last box).

Part II

Bacterial sensing

5 | Bacterial biosensing

The application presented in the previous chapters is an example of how electronics can be employed in conjunction to biological sciences to design new assays or enhance already existing assays, be it in size, ease of use or through automation. The CMFET LoC for telomerase detection makes use of telomeric probes, immobilized on an active surface, to detect the presence of the enzyme telomerase and monitor its activity. However, a wide variety of molecules can be sensed through the use of different bioreceptors.

The use of microbes (e.g., algae, bacteria, and yeast) as bioreceptor gives rise to interesting applications and has some advantages over more common bioreceptors such as enzymes [60]. Microbes are easy to obtain, because they can be produced in large numbers through cell-culturing. Also, compared to other cells from higher organisms such as plants, animals, and humans, some microbial cells, often used in research like *Escherichia coli*, are easier to manipulate and have better viability and stability *invitro*, which can greatly simplify the fabrication process and enhance the performance of biosensors. High selectivity can be achieved through microbial biosensors by adapting the microorganisms to an appropriate substrate of interest (target) through selective cultivation conditions [61, 62]. Moreover, recent progresses in molecular biology offer new techniques to give birth to genetically engineered microorganisms (GEMs), thus allowing new ways to manipulate the selectivity and sensitivity of microbial biosensors at the DNA level.

Most bacteria, like *Escherichia coli*, can respond to environmental changes in different ways and over different time scales: chemotaxis, which happens on short timescales (in the order of seconds to minutes) is used to bias movement towards nutrients and away from toxins, and depends on the available proteins. Over longer timescales, in the order of hours, *E. coli* reacts to the environment by producing new proteins with changes in its genetic expression through transcription and translation [63].

5.1 A slower response: transcription

Transcription in bacteria is a mechanism used to regulate gene expression. An example of a transcription-regulated response in *E. coli* is metalloregulation. Zinc plays a very important role in the cell. However, excess of zinc is toxic to the cell, therefore its intracellular level is finely controlled and regulated [64]. The cellular zinc quota is millimolar, but free Zn(II) concentrations that trigger transcription of zinc uptake or efflux machinery are six orders of magnitude less than one atom per

cell (or one atom every per 10^6 cell volumes). Metalloregulation of *E. coli* has a response time of about 20 minutes, roughly one cell generation, and a femtomolar sensitivity [65].

5.2 A fater response: chemotaxis

The chemotaxis has been widely studied for over three centuries [66]. As opposed to the metalloregulatory transcriptional system, chemotaxis requires the evaluation of the concentration of nutrients in shorter time scales, in the order of seconds. Through chemotaxis, the cell directs its movements according to the presence of chemical gradients in its environment. Chemotaxis is fast: large changes in the attractant L-serine affect motility withing 300 ms [67]. Moreover, chemotaxis is also sensitive: the detection limit for the attractant L-aspartate is 3.2 nM, which given a generic cell volume of 1 fL, corresponds to the detection of just 3 molecules [68]. These characteristics place chemotaxis near the limit of the ideal biosensor proposed by Berg and Purcell [69].

Some bacteria, like *E. coli*, move by alternating a random pattern made by tumble and swim phases. During swim phases (1 second on average) the cell follows a roughly straight line parallel to its long axis, whereas during tumbles (0.1 seconds on average) the cell roughly randomly changes its orientation. The resulting overall movement is a random-like walk. If no changes in the environment are detected, the bacterium will forage the surrounding environment while constantly monitoring its chemoreceptors. Then, if a gradient is detected, the bacterium will keep swimming in a straight line for a longer time before tumbling again. However, if it is moving in a wrong direction, tumbles will become more frequent to change its direction. In this way, bacteria can direct their motion towards nutrients, also know as chemoattractants, or adjust their tumbling frequency to move away from chemorepellents.

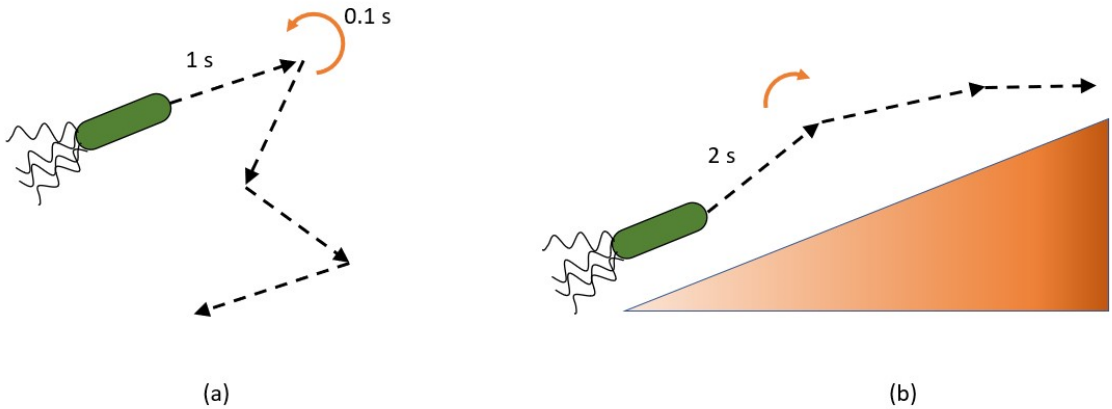

Figure 5.2.1: Chemotaxis in *E. coli*. (a) In absence of a chemical gradient, a random walk is performed to forage the environment. (b) When a chemical gradient is detected, runs are biased towards the direction of the gradient.

The chemotactic system makes use of differents components of the cell:

1. Bacterial flagellar motor;
2. Chemoreceptors;
3. Signaling pathway.

5.2.1 Bacterial flagellar motor

The bacterial flagellar motor is the actuator for locomotion in *E. coli* [70] and its rotation is the output of the chemotaxis pathway. The *E. coli* bacterial flagellar motor is a reversible rotary motor, no more than 50 nm in diameter, powered by an electrochemical-potential difference of specific ions across the cytoplasmic membrane. The motor, together with the hook and the filament, constitutes the flagellum (Fig. 5.2.2). Different speeds have been observed in different bacteria, from hundreds of Hz in *E. coli* to thousands of Hz in *Vibrio* [71]. Torque is generated by interactions between the rotor protein FliG and the stator units attached to the cell wall; the torque generated by a fully induced motor has been estimated to be approximately $1260\,\mathrm{pN}\cdot\mathrm{nm}$ [72] for *E. coli*.

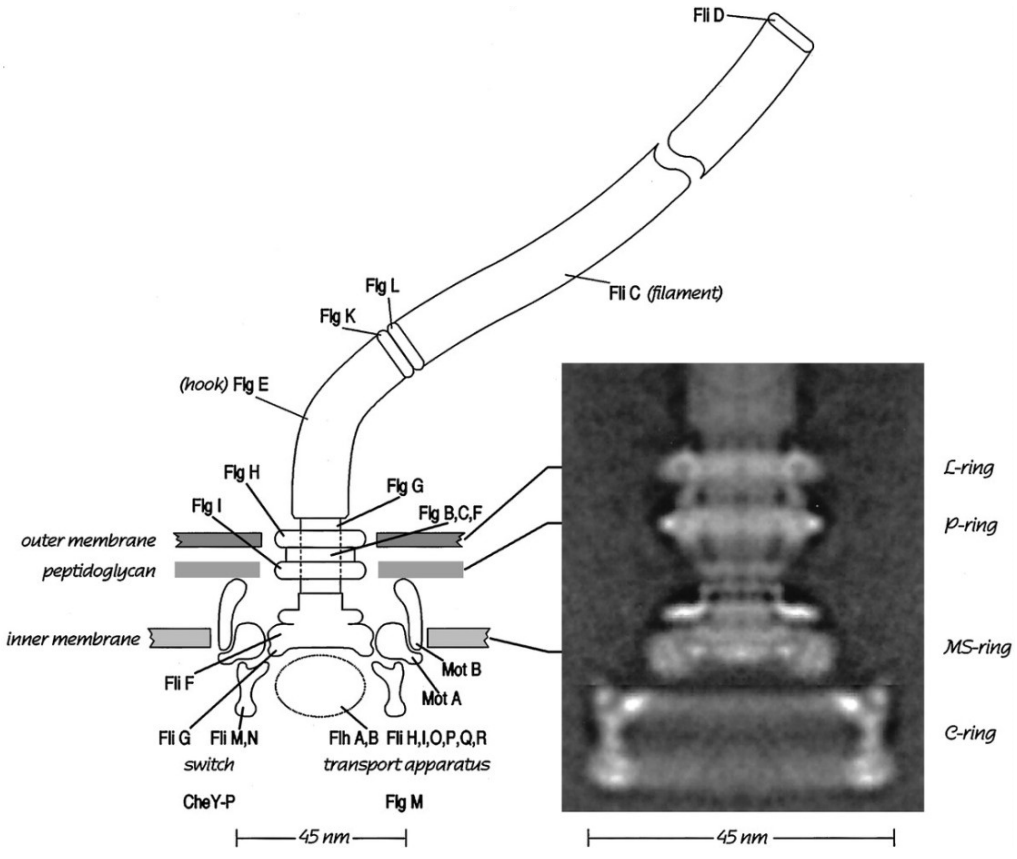

Figure 5.2.2: A schematic diagram of the flagellar motor, drawn to scale, compared to a reconstruction of images of hook-basal bodies seen in an electron microscope [70].

E. coli is a peritrichously flagellated cell, meaning that its multiple flagella, on average 6-8 per cell depending on growth conditions, are distributed along its

entire surface. The motor can spin clockwise (CW) or counterclockwise (CCW); the direction of the rotation is controlled by the chemotaxis biochemical network [73]. When all the flagellar filaments spin CCW, the cell is pushed steadily forward. When one or more filaments spin CW, they leave the bundle and the cell starts to tumble. Because of the spatial correlation among the signaling molecules, multiple flagella often switch rotation simultaneously, thus making the "effective number" of flagella smaller than the actual number and achieving more robust swimming against variations in flagella number [74]. Tracking the rotation of a cell body tethered by a single flagellum can provide an insight about the global trajectory of the cell: the probability of spinning CW or CCW changes in response to the presence of attractant or repellents [75] so meaningful information about the bacteria environment can be inferred.

5.2.2 Chemoreceptors and signaling pathway

Bacteria can sense the presence of chemicals in the environment through chemoreceptors. In particular, *E. coli* is equipped with five different chemoreceptors: Trg, for ribose and galactose; Tar, for aspartate; Tsr, for serine; Tap, for peptides; and Aer, which is the major oxygen-sensing transducer [76]. Bacterial chemoreceptors are transmembrane proteins (TP, a type of protein that spans across the entire cell membrane) that can detect chemical stimuli in the environment and send signals to a cytoplasmic two-component transduction system, consisting of a kinase (CheA) and a response regulator (CheY), to provide a real-time chemotactic response. CheA is a cytoplasmic histidine protein kinase capable of autophosphorylation.

When a repellent is sensed by the chemoreceptors, the kinase CheA is activated, which results in an increase in the phosphorylation of the CheY response regulator. This induces CW rotation of the flagella, resulting in a tumble. The presence of an attractant has the opposite effect: the CheA kinase is inhibited, preventing response regulator phosphorylation and thus blocking the interaction between the response regulator CheY and the flagellar motor, causing a straight run. A schematic depiction of the receptor-motor pathway is shown in Fig. 5.2.3. *E. coli* cells react to gradients of attractant or repellent, rather than on their concentration absolute value [77]. For example, when the cell detects a change in concentration of a repellent, it sends a signal to activate the kinase and change the motor response. However, after only a few seconds of swimming through the gradient, the cell returns exactly to its prestimulus swimming behavior, despite the continued presence of the repellent. This is accomplished by an adaptation system that makes use of changes in methyl esterification of glutamate sidechains in the receptor proteins [78].

Moreover, the *E. coli* chemotactic signaling pathway is able to amplify stimuli at least 50 times: for example, a 1% change in the receptor occupancy can generate a 50% change in the rotational bias of the flagellar motor. Measurements of CheA kinase activity *in vivo* by means of Förster resonance energy transfer (FRET) showed that a large portion of this amplification (36-fold) is due to the signaling complex [79]. A single receptor molecule can thus control 36 kinase molecules, which implies a functional network that links one receptor to multiple copies of the kinase. This

allows to achieve a really high sensitivity: a detection limit of 3.2 nM L-aspartate has been reported [68], which is a concentration three orders of magnitude lower than the detection limit in the standard chemotaxis capillary assay [80].

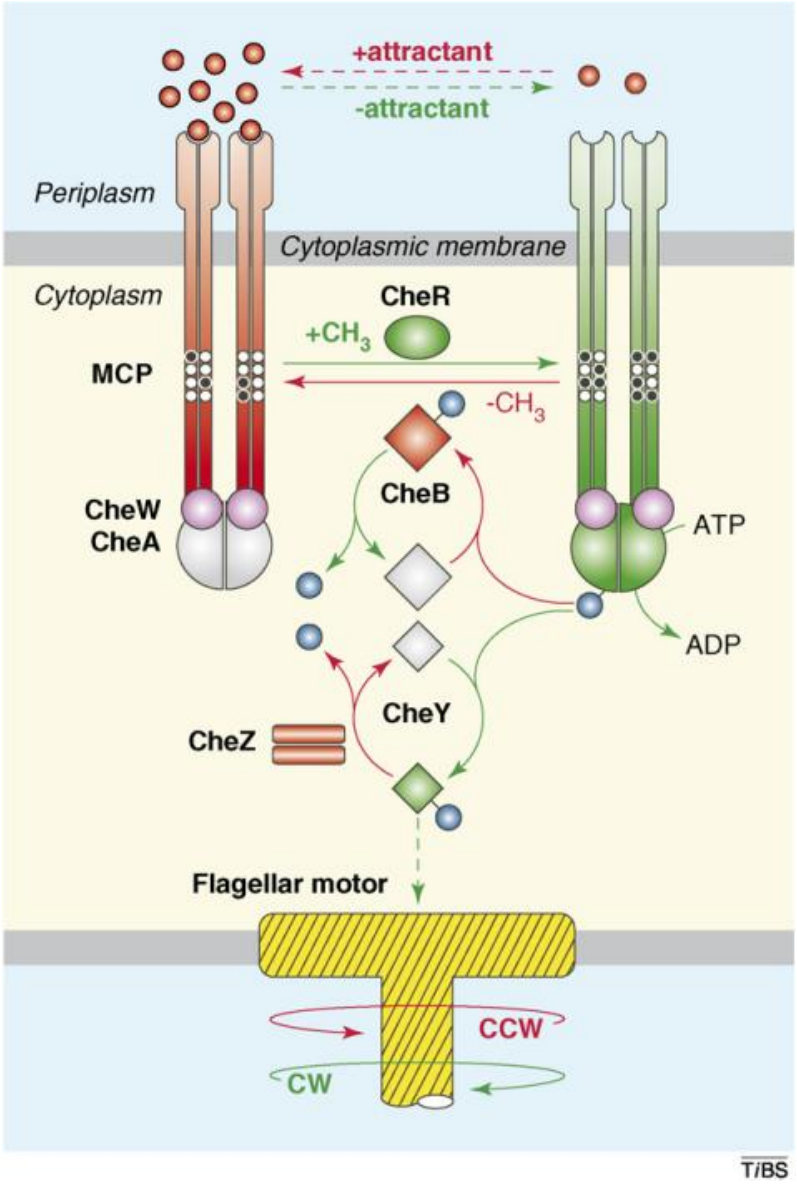

Figure 5.2.3: The chemoreceptor signaling pathway in E. coli. Components and reactions in red promote counter clockwise (CCW) flagellar rotation; those in green promote clockwise (CW) flagellar rotation [79].

5.3 Methods for assaying bacterial chemotaxis

Thanks to its properties, chemotaxis can give rise to interesting application in biosensing. Therefore, a wide variety of assays exist, which aim to evaluate the chemotactic activity of bacteria either in qualitative or in quantitative ways. Some of the assays require only simple and non-expensive lab equipment, while others

require more complex and sophisticated tools. Moreover, some assays focus on the movement of an entire population, others focus on single-cell activity. The next sections describe some examples of existing assays.

5.3.1 Capillary assay

The capillary assay was first described in the 1880s [81], but was finally standardized by Adler in the 1970s [80]. Many of the fundamental discoveries about chemotaxis, such as the discovery of chemoreceptors on the surface of the cell membrane, were made by using this simple assay [82]. A suspension of highly motile bacteria is loaded in chambers on the order of 1 cm^2 and 1 mm or less thick with one open side. Then, a 1 µm thick capillary sealed at one end is filled with an attractant and inserted into the chamber. After an incubation period, the capillary is removed from the chamber. The chemotactic activity can be estimated by looking at the capillary end: a positive response to chemotaxis results in the accumulation of bacterial cells in the capillary. Alternatively, the content of the capillary can be placed in a dilution buffer and later in a nutrient medium. The chemotactic response can be calculated from colony counts after some time. A quantitative chemotactic response can be obtained by comparing the colony count of the test colony and a buffer colony. The response to repellent can also be assessed by filling the capillary with repellent and measuring the decrease in the number of cells with respect to a buffer capillary or, vice versa, by filling the chamber with repellent and the capillary with buffer. Despite the simplicity of the method, some variation exist, that can perform parallel assays and achieve a high throughput[83].

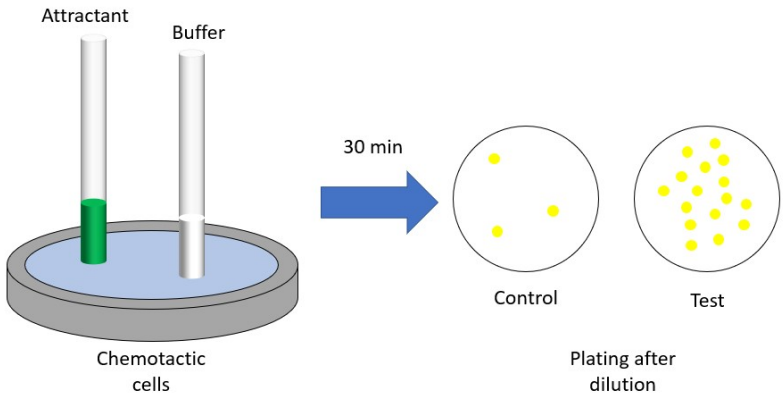

Figure 5.3.1: Schematic representation of the capillary assay and expected outcome.

5.3.2 Microfluidic assay

Microfluidics are becoming more and more common in biosciences because they require only a small sample volume is required, exhibit laminar flow and high throughput. Consequently, fast analysis can be performed. For example, microfluidic devices can generate specific and precise gradients of signaling molecules, which are very useful in the analysis of bacterial chemotaxis. The first example of microfluidic devices for bacterial chemotaxis has been presented by

Mao et al. [68]. A device with three inlets was designed, as shown in Fig. 5.3.2: a chemoeffector and a buffer solution are injected from two of them, developing a spatial gradient perpendicular to the direction of flow. *E. coli* cells are injected into the third inlet. At the end of the device, on the right side, cells enter one of the 22 outlets according to their migration, perpendicular to the direction of flow and dependent on the chemotactic response.

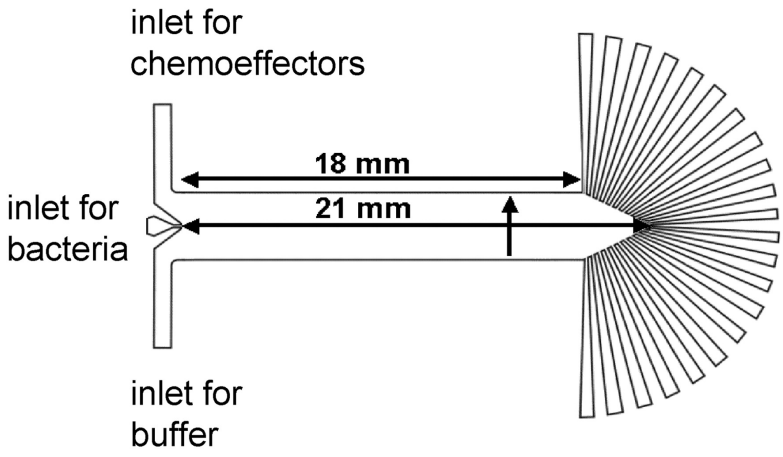

Figure 5.3.2: Device for microfluidic chemotaxis assays. The vertical arrow indicates the direction of increasing chemoeffector concentration across the channel [68].

More complex gradients can also be generated: Kalinin et al. [84] developed a microfluidic device for chemotaxis in which a dual concentration gradient is created inside a microchannel by diffusion of two parallel streams in laminar flow (Fig. 5.3.3). By using two grandients with the same attractant strenght, methyl-aspartate and serine, they demonstrated that chemotaxis response of *E. coli* bacteria in dual gradients depends on the ratio of the receptor number of Tar/Tsr. The versatiliy of microfluidics enables a wide variety of tests which are not easy to perform with other approaches.

5.3.3 Tethered cells assay

Due to the balance of forces, when flagella rotate the whole cell body rotates in the opposite direction. If a single flagellum is tethered on a surface, a CW rotation of the flagellum generates a CCW rotation of the cell body, and a CCW rotation of the flagellum makes the cell body rotate CW. Therefore, information on the presence of attractants or repellents can be inferred from the rotation of the entire cell body: attractants cause longer periods of CW rotation (due to longer straight runs) and repellents cause briefer periods of CCW rotation (due to more frequent tumbling).

Cells can be tethered with antiflagellar filament antibodies that bind specifically to the flagella and nonspecifically to the substrate, which is typically a glass slide or coverslip [85]. However, by using an *E. coli* strain that expresses sticky filaments because of the $fliC^{ST}$ mutation in its genome, the need for antibodies can be eliminated [86]. Moreover, flagella can also be functionalized by attaching antibody-coated latex beads [87]. A large number of cells can be

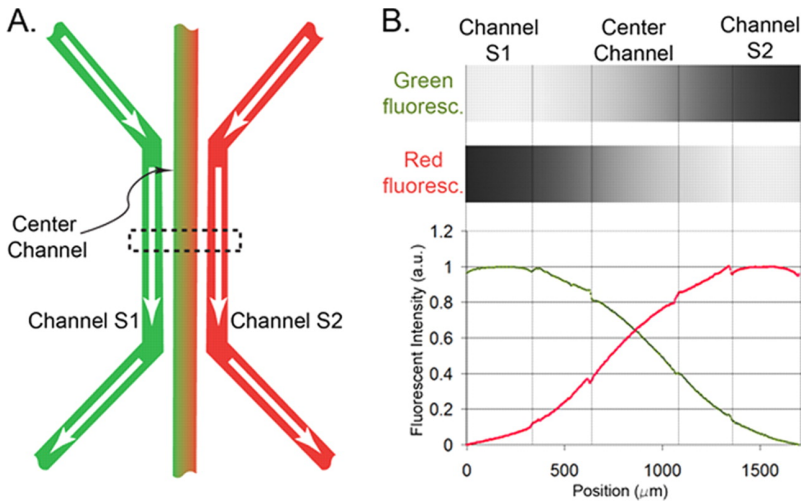

Figure 5.3.3: Microfluidic device for dual chemical gradient generation [84]. (A) Two different chemicals are flowed through the side channels and diffuse into the central channel through the agarose gel barrier, creating a dual concentration gradient. (B) Concentration gradient profile measured with fluorescent dyes.

video-recorded at the same time and analyzed later, either by an observer or with various automatic systems. For example, Zajdel et al. [88] applied machine learning techniques to monitor bacteria chemotaxis. Bacteria were tethered on a substrate and exposed to chemical gradients. The recorded images were processed to extract information about the rotation of cells, and a support vector classifier (SVP) has been trained to detect chemical presence of the attractant Asp and repellent Leu, and differentiate between them.

6 | Electronic bacteria flagellar motor detection

6.1 BFM sensing

The characteristics of chemotaxis, which is a fast and sensitive process, make the combination of bacteria and biosensing an interesting possibility. Studies on the response of bacteria like *E. coli* to chemical stimuli have already been made: in [89] experiments were conducted on *E. coli* during chemotaxis by using *in vivo* Förster resonance energy transfer (FRET), which is a single-cell technique that allows to measure intracellular changes during chemotactic stimulation. In [90] bacteria are observed under the microscope while swimming, under the presence of chemical gradients. Responses to aspartate, glucose, leucine, and serine have been recorded. Results were in agreement with more standard methods like flagella tethering, with the advantage of being a non-invasive method. Tethered cells assays, as described in 5.3.3, also allow the observation of multiple cells at the same time. Moreover, the limitation given by the small size of flagella can be overcome by observing the whole cell body, or even by attaching large latex bead on the flagella. However, all the cited types of assay require high resolution and high frame rate microscopes, which may not be suitable for low power and portable applications. This work was born as a continuation of the work presented by Zajdel et al. [91], in which a biohybrid sensor is developed to monitor the bacterial flagellar motor (BFM) rotation and speed by electrochemical means: in particular, by tethering bacteria between a set of electrodes, changes in impedance caused by BFM can be detected. To reduce the effects of the double layer capacitance, a pair of 4 µm by 4 µm electrodes were used for potential sensing, while larger 100 µm by 100 µm electrodes were used for current injection. Measurements of the solution resistance were performed at 10 kHz. However, a signal-to-noise ratio (SNR) of only 7 dB was obtained for a bead that enters and then completely leaves the electrode array. Thus, the resolution of the system was not sufficient to detect changes in impedance due to the BFM rotation. Moreover, due to the discrete nature of the system, the measurement frequency was limited by parasitic capacitances.

The aim of this work is to develop an ASIC (Application Specific Integrated Circuit) based on the same working principle. The goal of the ASIC is to allow fully electronic monitoring of BFM by solving the issues encountered in the former discrete-component implementation, and achieve higher SNR and higher measurement frequency.

6.1.1 Electrochemical impedance measurements

As briefly explained in Chapter 1, when electrodes are immersed in an electrolytic solution and a potential is applied between them, the ions in the solution interact with the electrode and form a double-layer capacitance. The first and simplest model of this phenomenon was introduced by Helmholtz [92], which described it as a capacitor whose plates were represented by the electrode surface and the layer of adsorbed ions on its surface. The model was later refined by Gouy and Chapman [93, 94], which hypotesized the presence of an additional diffuse layer with a Maxwell-Boltzmann distribution of charge. Later on, Stern unified the two previous models: some ions adhere to the electrode surface and form a "compact layer" or "Helmholtz layer", causing the largest potential drop, while other ions diffuse in a Gouy-Chapman layer. A final refinement of the model is presented by Grahame in 1947, which introduces a separation of the Helmholtz layer into two parts: the *Inner Helmholtz Plane* (IHP), made by specifically adsorbed ions, and the *Outer Helmholtz Plane* (OHP), made by ions that are non-specifically adsorbed or attracted by electrostatic force. Finally, a diffuse layer extends until the bulk of the solution.

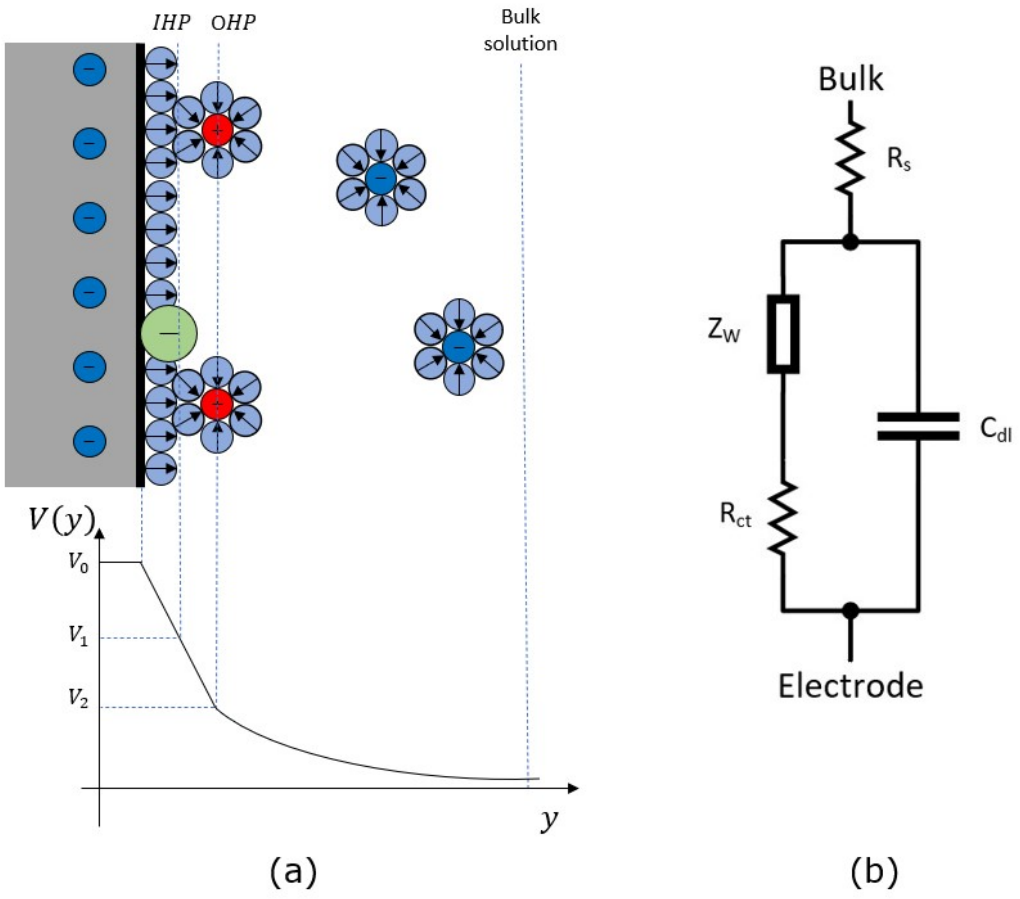

Figure 6.1.1: (a) Schematic representation of the double layer structure. (b) Randles equivalent circuit.

The double-layer interface can be modeled with an equivalent electrical circuit-

The Randles model is shown in Fig. 6.1.1. It consists in the resistance of the bulk solution R_s, in series with the parallel of a double layer capacitance C_{dl}, a charge transfer resistance R_{ct} and a Warburg element Z_W. The C_{dl} describes the double-layer capacitance that is present at the interface between the electrode and the electrolyte. The faraidic process is described through the charge transfer resistance and the Warburg element, which describes the diffusion process and is negligible at high frequencies.

Electrochemical impedance measurement methods are currently able to detect single dielectric beads and even single cells by the Coulter counter principle, and can be useful in the development of a BFM monitoring system. The working principle of the Coulter counter, invented by Wallace H. Coulter in the 1940s, is based on the fact that a particle that passes through a microchannel in which a current is flowing, produces a resistance change that is proportional to the volume of the particle itself. Since cells can be approximated with insulating spheres below certain frequencies (in the order of MHz), a cell that passes through the channel increases the solution resistance and so the current across the channel decreases. With this principle it has been possible to precisely count the number of particles or cells in a given volume of fluid. Moreover, after the introduction of impedance flow cytometry, the Coulter principle has been extended and microelectrodes can now be integrated on the walls of the microchannel or even at the bottom as coplanar electrodes [95]. Microelectrodes can be fabricated with a size of the same order of magnitude of the cells adn by using a differential configuration, the cell properties can be measured while canceling all the secondary effects of the electrodes and the medium.

A similar approach would allow the detection of bacterial flagellar motor activity: as depicted in Fig. 6.1.2a, an *Escherichia coli* cell could be tethered on the surface between two coplanar electrodes and its movement would produce changes in the measured solution resistance. For this purpose, the equivalent circuit of the electrochemical cell has been simplified to describe this system, according to [96] and shown in Fig. 6.1.3a.

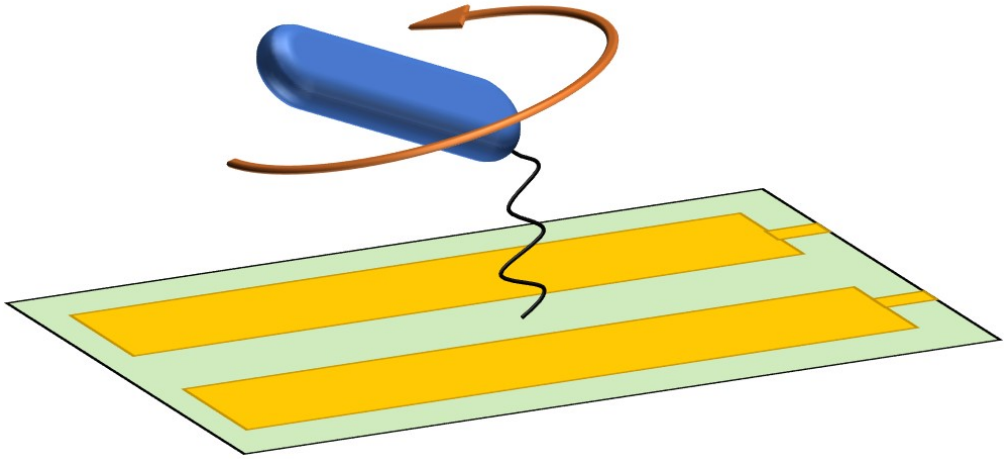

Figure 6.1.2: Schematic representation of the proposed BFM monitoring principle.

The frequency of the measurements depends on the properties of the solution and the cells in it. The target of the measurement is the solution resistance, which

changes depending on the bacterium activity. Figure 6.1.3b shows the expected impedance spectrum of one of the designed electrochemical cells when the electrode voltage is swept in frequency. At low frequencies (the C_{DL} region in Fig. 6.1.3) the total impedance of the solution is dominated by the double-layer capacitance, which depends on the electrodes area. Small electrodes yield a small capacitance value (in the tenths of picofarad range), which in turn becomes a very large impedance (for example, a capacitance of 1 pF corresponds to an impedance of $\frac{10^{12}}{2\pi F}$, in which F is the frequency of the voltage applied to the electrodes).

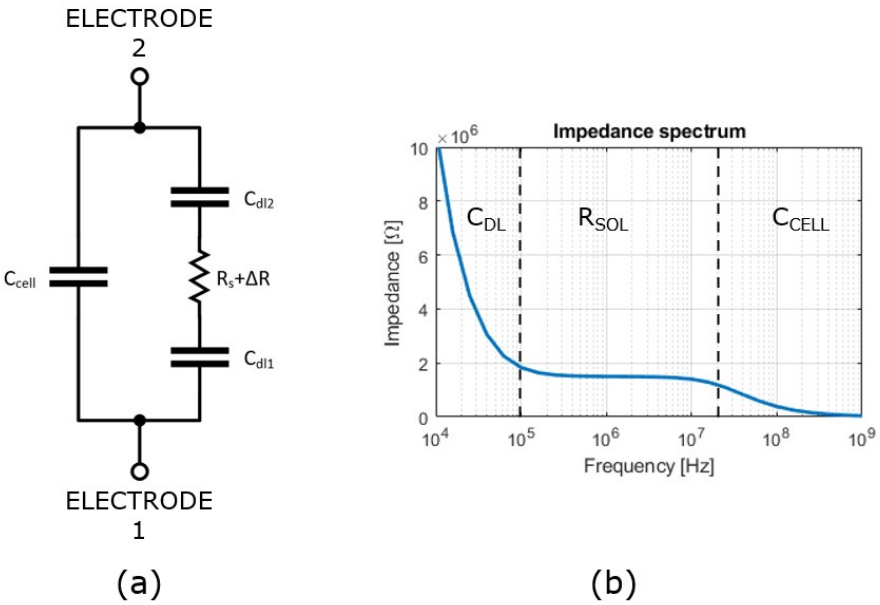

Figure 6.1.3: (a) Equivalent circuit for coplanar electrodes. (b) Expected impedance spectrum.

Increasing the frequency, the double-layer capacitance becomes negligible and the impedance value is mostly given by the solution resistance R_{sol}. Finally, if frequency is increased again, the impedance major contribution is given by the capacitive coupling between the electrodes. Thus, the frequency of the voltage applied to the electrodes must be chosen carefully to be able to perform measurements in the R_{sol} region.

6.1.2 Impedance measurement principle

Impedance has become an important tool in biosciences, due to its many applications, from cell monitoring to affinity biosensors. General purpose LCR meters are instruments used to measure inductance L, capacitance C and resistance R (such as E4980AL LCR meter from Keysight Technologies), but many application-specific solutions exist, such as the AD594x family of impedance analyzers (Analog Devices) or custom ASICs tailored for a single application. A widespread method for impedance measurement is the auto-balancing bridge [97], whose basic scheme is shown in Fig. 6.1.4. The auto-balancing bridge balances the current that flows through the range resistor I_r with the DUT (Device Under Test)

current I_x while keeping a zero potential at the L_p terminal. If the two currents are not equal, a difference current flows through the Null Detector, which in turn controls the amplitude and phase of the OSC2 output until the detected current goes to zero. Since the L_p voltage is at the virtual ground, the output voltage V_r can be expressed as:

$$V_r = I_r R_r = I_x R_x \tag{6.1}$$

The current I_x through the DUT is determined by the impedance of the DUT and the voltage V_x, as:

$$I_x = \frac{V_x}{Z_x} \tag{6.2}$$

Then, combining Eq. 6.1 and 6.2, the expression for the unknown impedance Z_x is derived:

$$Z_x = \frac{V_x}{I_x} R_r = \frac{V_x}{V_r} \tag{6.3}$$

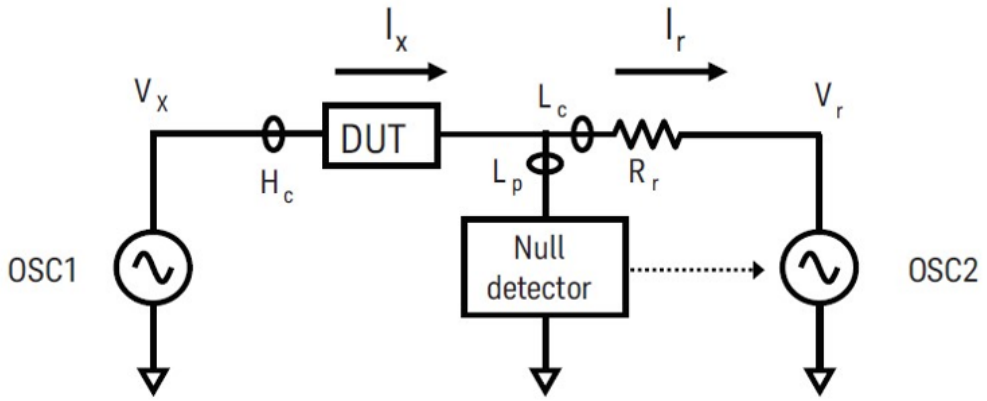

Figure 6.1.4: Auto-balancing bridge impedance measurement scheme [97].

Thus, the DUT impedance can be obtained by measuring the vector voltages V_x and V_r, since the value of the R_r resistor is known.

The implementation of the auto-balancing bridge in different depending on the application. For measurements below 100 kHz, a simple operational amplifier can be used to implement both the null detector and the OSC2. For higher frequencies, the performance of the instrument is limited by the operational amplifier. Thus, instruments that cover frequencies higher than 100 kHz employ a $0°/90°$ phase detector to separate the null detector signal into real and imaginary part, and then generate the OSC2 signal with a vector modulator which combines real and imaginary parts again, to cancel the current I_x. In this way, both the amplitude and phase errors can be detected and balanced out [97].

6.2 System architecture

The measurement system implemented in the ASIC is based around the auto-balancing bridge, but with a few differences. In the block diagram of the system architecture, shown in Fig. 6.2.1, the Z_{DUT} represents the impedance of the electrochemical cell made by the bacteria and the surrounding solution. Since the target of the measurement is not the solution impedance itself, but more specifically the impedance variation caused by the bacteria rotation, a differential approach has been chosen to eliminate the dependency on the "base" impedance, while measuring only the variations.

The Z_{REF} has been physically implemented by an identical electrochemical cell which, ideally, should balance the current coming from the DUT when the voltages V_{AC1} and V_{AC2} are equal in amplitude and opposite in phase. Due to process mismatch and variations, the two electrochemical cells will not be exactly identical, but the two input voltages V_{AC1} and V_{AC2} can be set off-chip to obtain a null current I_{EL} from the electrodes.

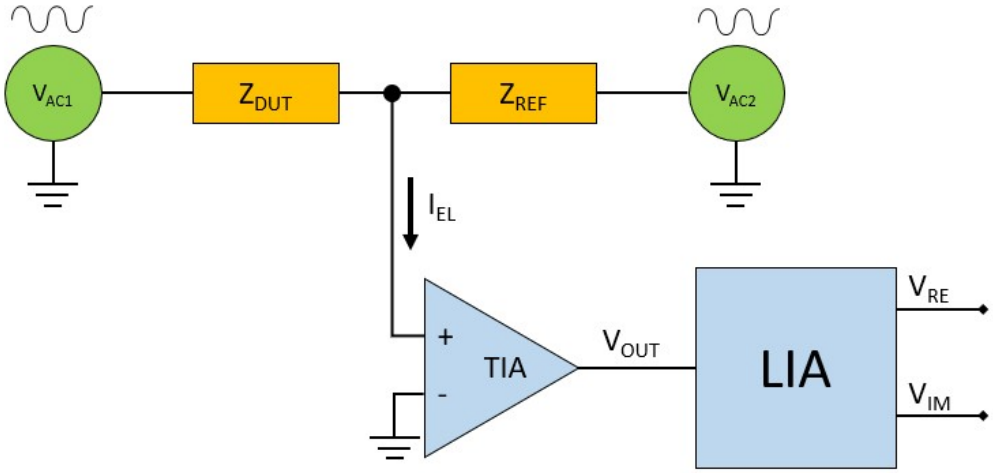

Figure 6.2.1: Implemented impedance measurement scheme.

A variation in the Z_{DUT} impedance caused by bacteria presence and/or movement generates a non-zero I_{EL} current, proportional to said variation. A transimpedance amplifier (TIA) with programmable gain is used to convert the current into a voltage and amplify it. The resulting voltage is fed to a lock-in amplifier (LIA) which extracts the real and imaginary part of the voltage and filters the high frequency components, resulting in a low frequency output which is still proportional to the impedance variation, which happens on a time scale in the order of hundreds of milliseconds.

Due to the fact that the first version of the ASIC is focused on testing the working principle with different electrode sizes, the electrode active substrate and the lock-in amplifier have been integrated in a CMOS 0.18 µm process from TSMC (Taiwan Semiconductor Manufacturing Company), while the generation of the input signals and the output ADC (analog-to-digital conversion) circuitry are not integrated in the chip; bench-top signal generators and discrete components will be used for testing.

6.3 Electrochemical cell design

In the previous realization of this project, electrodes were fabricated by photolitography techniques and physical vapour deposition (PVD) of metals [91]. The resulting microelectrode array consisted of a pair of 100 µm×100 µm current-injecting electrodes and 4 µm×4 µm sensing electrodes, to reduce the effects of the double layer capacitance on measurements performed at 10 kHz. The upper frequency limit was constrained by printed circuit board parasitics. Parasitic capacitances can be greatly reduced by transitioning from discrete components to an integrated circuit, thus the maximum measurement frequency of the input signals can be much higher. As a consequence, on the ASIC the 4-electrodes electrochemical cell has been replaced by a 2-electrodes cell, getting rid of the larger current-injection electrodes. Electrodes with a size comparable to the size of *E. coli* have been designed, ranging from 10 µm to 0.75 µm by side. For the next section, three different geometries will be analyzed, as reported in Table 6.1. All the electrodes are coplanar electrodes made of Aluminum and, by default, passivated due to the process design rules constraints on passivation openings (the smallest apssivation opening window was 80 by 80 μm^2). The values here presented do not take into account the passivation layer, which can be later removed by post-processing operations.

Electrode type	Width [µm]	Length [µm]	Spacing [µm]
A	2	5	2
B	1	1	2
C	0.75	0.75	1

Table 6.1: Different electrode types.

The first modeled element of the equivalent circuit in Fig. 6.1.3 is the double layer capacitance C_{dl}:

$$C_{dl} = \varepsilon_r \varepsilon_0 \frac{A}{\lambda_D} \tag{6.4}$$

where ε_r is relative permittivity of the solution, ε_0 is the vacuum permittivity, A is the electrode area and λ_D is the Debye length. Table 6.2 shows an example of the calculated values of the double layer capacitance C_{dl} for the three different geometries. As already mentioned, smaller electrodes are characterized by a smaller double layer capacitance, which can hinder the measurements if the frequency is not high enough.

Type	C_{dl}
A	3.36 pF
B	0.34 pF
C	0.19 pF

Table 6.2: Double layer capacitance for different electrode geometries.

To model the solution resistance R_{sol} and the effect of bacteria activity between the electrodes, some approximations are required. The cellular body of *E. coli* has been approximated by a sphere with a volume of $0.5\,\mu m^3$, made of cytoplasm enclosed by a thin insulating membrane, which is a valid approximation for frequencies up to a few MHz [98]. The conductivity of cytoplasm has been estimated as σ_i=3 mS cm^{-1}, which is consistent with results found in literature by dielectric measurement of cell suspensions in a wide frequency range (from 1 kHz to 110 MHz) [99]. The conductivity σ_s of the motility medium in which bacteria live, which is primarily a 10 mM potassium phosphate buffer solution, has been measured with a Sension+ EC71 conductivity meter at about 1.5 mS cm^{-1}.

A rough estimate of the impedance variation caused by the activity of bacteria between the electrodes has been calculated by considering the variation due to the presence of a single spherical cell of the same volume of the average *E. coli* cell, with respect to the impedance of the medium without any bacteria in it. Starting from Pauly and Schwan studies [100], Hoffman and Britt [101] proposed the following equations for a suspension of spherical non-conducting cells:

- conductivity is essentially constant when the frequency is very high or very low compared to a characteristic frequency f_0, which can be calculated as:

$$f_0 = \left[\pi D C_m \frac{\sigma_i + 2\sigma_s}{2\sigma_i \sigma_s}\right]^{-1} \tag{6.5}$$

  D indicates the cell diameter (assumed here at 1 µm for a cell volume of about $0.5\,\mu m^3$), C_m is the membrane specific conductance (1 µF cm^{-2}[102, 99]). A characteristic frequency of about 5 MHz has been calculated. Therefore, most measurements will happen at frequencies around or below 5 MHz.

- the low-frequency and high-frequency conductivity limits σ_0 and σ_∞ are given by:

$$\sigma_0 = \sigma_s \frac{(1-p)}{1+p/2} \tag{6.6}$$

$$\sigma_\infty = \sigma_s \frac{1 + 2p(\sigma_i - \sigma_s)/(\sigma_i + 2\sigma_s)}{1 - p(\sigma_i - \sigma_s)/(\sigma_i + 2\sigma_s)} \tag{6.7}$$

  where σ_s is the medium conductance, σ_i is the cytoplasm conductance and p is the volume fraction of the cells, obtained as a ratio between the volume of the *E. coli* cell and the volume of the electrochemical cell. σ_0 and σ_∞ represent the suspension conductivity when the frequency is either very low or very high compared to the characteristic frequency f_0.

- finally, the conductivity of the cell suspension at a given frequency f is calculated as:

$$\sigma = \sigma_\infty + \frac{[\sigma_0 - \sigma_\infty]}{[1 + (f/f_0)^2]} \tag{6.8}$$

The conductivity variation due to the presence of the bacterium between the electrodes has been calculated as $\Delta\sigma = \sigma - \sigma_s$, i.e. the conductivity of the medium with cells minus the conductivity of the medium without any cells. The conductivity terms in the equations above is expressed as $\mathrm{S\,cm^{-1}}$. To obtain the corresponding resistance value, the following expression has been used [103]:

$$R_{sol} = \rho\frac{k_{cell}}{L} = \frac{1}{\sigma}\frac{k_{cell}}{L} \tag{6.9}$$

where ρ is the resistivity of the solution (which is the inverse of conductivity), k_{cell} represents the cell constant and L is the length of the microfluidic channel in which the electrodes are situated. The cell constant depends on the electrodes geometry, specifically on the area A and distance d between the electrodes, and would simply be $k_{cell} = d/A$ in the case of parallel electrodes. However, because the electric field generated by coplanar electrodes is not homogeneous, conformal mapping techniques are required to better describe the cell constant. The Matlab script provided by Linderholm [104] has been used to calculate the cell constant for different electrode geometries. The value is calculated based on the width of the electrodes along the flow direction, the spacing between the electrodes and the channel height, which is taken with an arbitrary value of 10 µm and depends on the microfluidic system that delivers bacteria on the electrode area. The cell constant for the three different geometries is shown in Table 6.3.

Type	Cell constant
A	1.314
B	1.5854
C	1.3975

Table 6.3: Cell constant for different geometries.

Finally, it is possible to estimate the change in the resistance solution given by the cells using Eq. 6.9: results are reported in Table 6.4 for the three geometries analyzed. A frequency of 5 MHz has been supposed, so that the contribution of the double layer capacitance C_{dl} is negligible compared to the solution resistance (being two to three orders of magnitude lower than R_{sol}).

Electrode type	ΔR	$\Delta R\%$
A	1.1 kΩ	0.06
B	49 kΩ	0.46
C	122 kΩ	0.98

Table 6.4: R_{sol} variation due to a cell between the electrodes.

The $\Delta R\%$ means that a variation of less than 1% on the base R_{sol} value is caused by the presence of an *E. coli* cell between the electrodes. However, performance can be enhanced by changing the size of the sensing target: for example, insulating latex beads, which have lower conductivity ($10^{-5}\mathrm{S\,cm^{-1}}$) and come in different sizes, can be attached to flagella, thus the displacement caused by a larger volume will cause a

larger resistance change. Table 6.5 reports the R_{sol} changes calculated with a 1 µm radius latex bead (assuming a conductivity of $10^{-5}\mathrm{S\,cm^{-1}}$), which are significantly higher than the values calculated with the bacterium alone.

Electrode type	ΔR	$\Delta R\%$
A	35.3 kΩ	2
B	1.75 MΩ	16.6
C	5.03 MΩ	40.5

Table 6.5: R_{sol} variation due to a bead between the electrodes.

It should be recalled that all the calculations refer to the change in impedance caused by the presence of a cell/bead between the electrodes, with respect to a solution without any cells. The actual variation caused by the rotation of the cell (or bead) during chemotactic activity will definitely be smaller, because a tethered cell will always be present between the electrodes. However, it can be a good approximation, especially for the smaller electrodes: depending on where the cell is tethered and its size, during the rotation it could move inside and outside the electrode area, causing a resistance variation that is similar to the one described above. Due to the high variability of all the elements that can be taken into consideration, it has been decided to allow some degree of tuning to the electronic circuits (such as programmable gain and cut-off frequency), so that different scenarios can be accommodated.

6.4 Electronic front-end

The impedance variations obtained from the previous Section can be measured by monitoring the current flow between the electrodes. Due to the impedance magnitude, currents in the order of $\sim 10^{-9}$ ampere or less are expected; thus, as shown in Fig. 6.2.1, the electronic front-end has been designed in order to provide high gain and at the same time reduce the noise that comes from the environment and the electronics. The front-end circuits are analyzed in the following sections.

6.4.1 Transimpedance amplifier

The transimpedance amplifier is used to convert the current coming from the electrodes into a voltage, while also providing high gain. To further increase the overall gain, a current preamplifier has been designed according to the work presented by Ferrari et al. [105] and shown in Fig. 6.4.1. The matched NMOS-PMOS pairs work in the same operating point and by using N replicas at the output, an output current N times larger than the input current is generated. Two stages have been cascaded, each with a N value that ranges from 10 to 100. The number of instances N can be set by digital control signals to provide an overall gain ranging from 40 dB to 62 dB; the option to bypass the entire current preamplifier has also been included. The current consumption has been simulated at 6.2 mA.

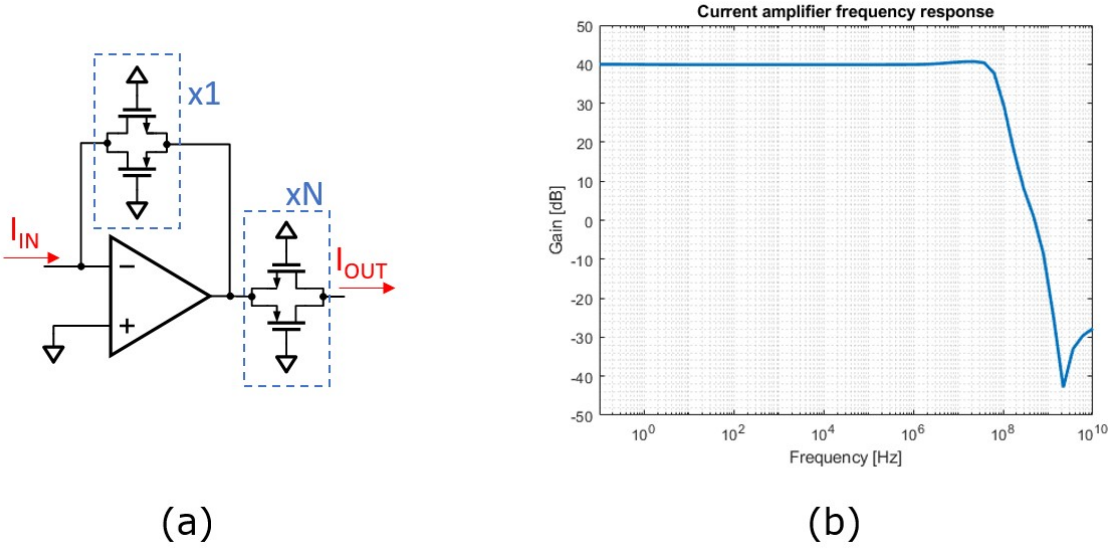

Figure 6.4.1: (a) Current amplifier schematic. (b) Frequency response of the current amplifier with a gain of 40 dB, over a 0.1 Hz to 10 GHz range. The 40 dB gain of the current amplifier is constant up to 50 MHz.

The next stage is composed of a two-stage transimpedance amplifier. The standard transimpedance architecture was not suitable for this application due to the high power requirement to keep a high gain at frequencies in the order of 1-10MHz. For this reason, the architecture proposed in [106] was used (reported in Fig. 6.4.2). By using capacitor C_1 as the feedback and considering the virtual short-circuit approximation at the input of the first stage, a gain A_{R1} can be obtained as:

$$A_{R1} = -\frac{1}{2\pi j f C_1} \tag{6.10}$$

By introducing a second stage with gain $A_{v2} = (-2\pi j f C_2 R)$, the gain results to be independent from frequency and is given by:

$$A_{R0} = A_{R1} A_{v2} = -\frac{1}{2\pi j f C_1} \cdot (-2\pi j f C_2 R) = \frac{C_2}{C_1} R \tag{6.11}$$

A high-value resistor R_1 is added in parallel to C_1 to allow a direct current flow at low frequencies to bias the inverting input of the first stage op-amp. Moreover, if a R_2 resistor is added such that $R_1 C_1 = R_2 C_2$, the gain in the frequency range in which the virtual short-circuit approximation still holds is unchanged.

If the ratio between C_2 and C_1 is large enough, the resistor R can be set smaller compared to the feedback resistor in a standard transimpedance amplifier while obtaining the same low-frequency gain and reduced noise. The value of R has been made programmable by digital logic, for a transimpedance gain of 120 dB to 132 dB. By taking into account the current amplifier gain, the overall gain ranges from 120 dB to 190 dB up to 10 MHz.

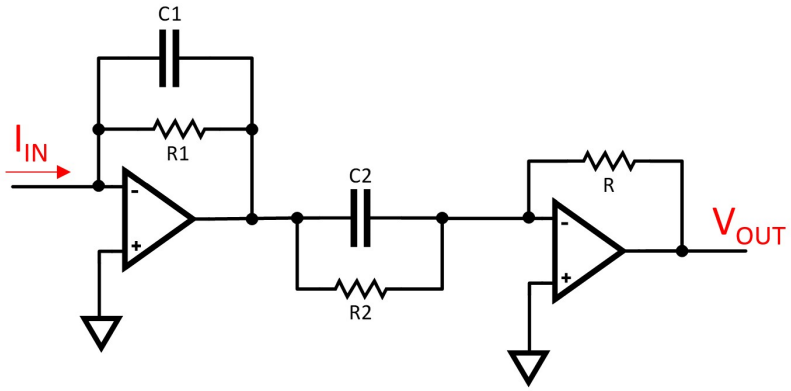

Figure 6.4.2: Two-stages transimpedance amplifier.

6.4.2 Lock-in amplifier

Lock-in amplifiers were invented in 1930s and 1940s [107, 108] and are used to extract small signals in a very noisy environment. The scheme of a lock-in amplifier is presented in Fig. 6.4.3. The input signal V_i is multiplied by a periodic reference signal V_r and then filtered by a low-pass filter. For example, assuming both signals as sinewaves such as $V_i = V_I \sin(\omega_i t + \theta_i)$ and $V_r = V_R \sin(\omega_r t + \theta_r)$, the resulting signal at the output of the multiplier is:

$$\begin{aligned} V_{out} &= V_I V_R \sin(\omega_i t + \theta_i) \sin(\omega_r t + \theta_r) \\ &= \frac{1}{2} V_I V_R cos([\omega_I - \omega_R]t + \theta_I - \theta_R) - \frac{1}{2} V_I V_R cos([\omega_I + \omega_R]t + \theta_I + \theta_R) \end{aligned} \tag{6.12}$$

So the output will always be two signals, one at the difference frequency $\omega_I - \omega_R$ and the other one at the sum frequency $\omega_I + \omega_R$. If the signals have the same frequency ω, the resulting signal will be:

$$V_{out} = \frac{1}{2} V_I V_R cos(\theta_I - \theta_R) - \frac{1}{2} V_I V_R cos(2\omega t + \theta_I + \theta_R) \tag{6.13}$$

If the output signal is then filtered with a low-pass filter to remove the 2ω component, only a DC signal is left, which is proportional to the amplitude of the input signals:

$$V_X = \frac{1}{2} V_I V_R cos(\theta_I - \theta_R) \tag{6.14}$$

Moreover, if two multipliers are used, one with a reference in phase with the input signal and the other one in quadrature with the input signal (90° phase difference), both the real and the imaginary part of the signal can be extracted (V_X and V_Y respectively in Fig. 6.4.3.

Multiplier

The multipliers for the lock-in amplifiers have been implemented as switching multipliers. The requirement on the reference signal is that it has to be a periodic

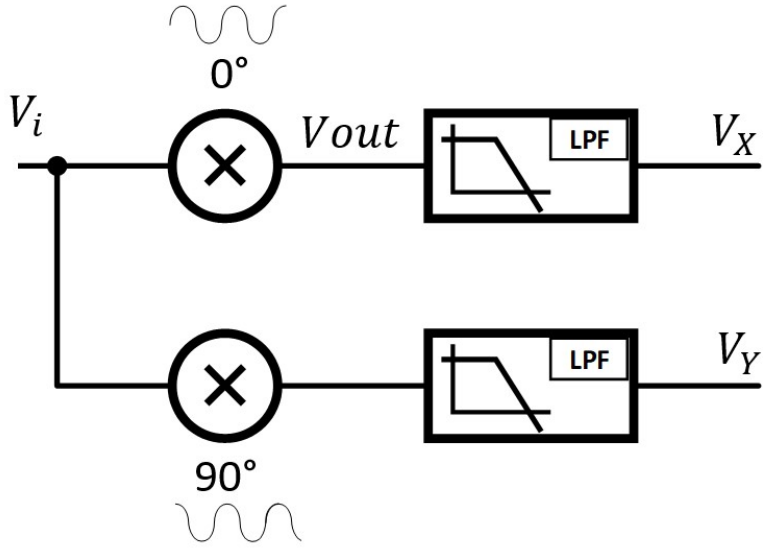

Figure 6.4.3: Lock-in amplifier schematic. The input signal, coming from the TIA amplifier, is multiplied by a in-phase reference signal and a quadrature signal, respectively, with the same frequency as the stimulus signal. The output of the multipliers are then low-pass filtered to extract the real and imaginary components V_X and V_Y.

signal with the same frequency as the measurement frequency. The simplest form of multiplication can be realized by multiplying the signal with a square wave at the same frequency; this operation can be obtained by feeding an operational amplifier with the signal and periodically change its gain from 1 to -1 V/V. The schematic of the mixer is shown in Fig. 6.4.4. The square wave signal is used to drive transmission gate switches which change the configuration of the amplifier from voltage buffer (gain $A_v = 1V/V$) to inverting amplifier (with two identical resistors, thus gain $A_v = -1V/V$).

Low-pass filter

The low-pass filter has been implemented with a $G_m - C$ architecture. $G_m - C$ filters are build by an operational transconductance amplifier (OTA) and a capacitor. The cut-off frequency of the filter is proportional to the transconductance G_m of the OTA and inversely proportional to the capacitance value.
A $G_m - C$ filter has been chosen for this application because a low cut-off frequency is necessary for the lock-in amplifier. A target frequency of 200 Hz has been chosen, which has been considered a good trade-off between the area occupation of the required capacitors and the frequency needed to detect bacteria rotation, which is in the tens of Hz. The cut-off frequency ω_t of a standard active low-pass filter is given by:

$$\omega_t = \frac{1}{2\pi RC} \tag{6.15}$$

so, to obtain a cut-off frequency of about 200 Hz, a 100 kΩ resistor and a 7 nF

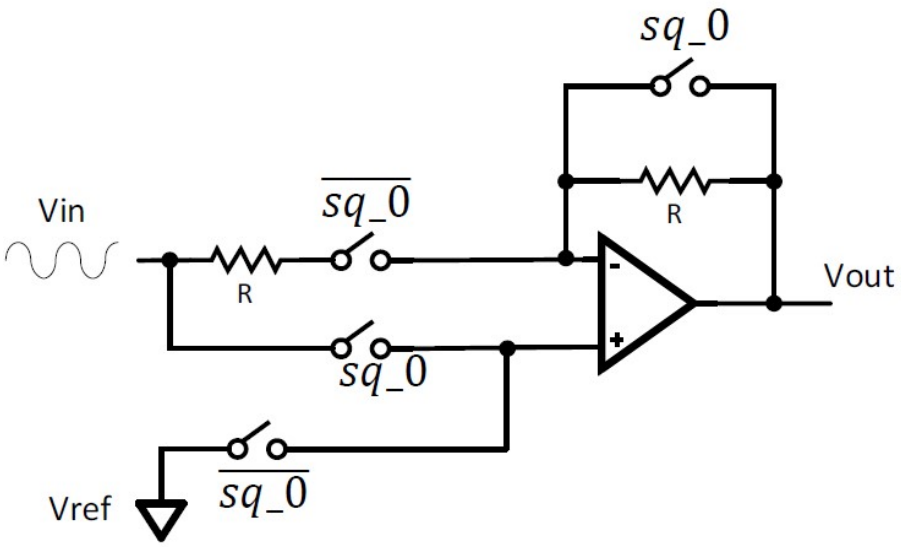

Figure 6.4.4: Switching mixer schematic.

capacitor are required (from Eq. 6.15), for example, which are not easily implementable in a chip with area constraints.

Equation 6.16 shows the expression for the cut-off frequency of the implemented $G_m - C$ filter, as presented in [109], and depicted in Fig. 6.4.5a. To obtain the same 200 Hz cut-off frequency the capacitance values can be greatly reduced while decreasing the G_m of the OTAs. For example, by using two 10 pF, a 200 Hz cut-off frequency can be obtained with a G_m of 2 µS. Hence, a low-G_m OTA has been designed, whose schematic is reported in Fig. 6.4.5b.

$$\omega_t = \frac{G_m}{\sqrt{C_1 C_2}} \tag{6.16}$$

The low G_m OTA is based on a standard P-type OTA in which transistors M4 and M7 act as the differential pair and M9, M10 make the active load. However, two modifications have been added to reduce the G_m of the OTA: transistors M5 and M6 are used as a source degeneration to decrease G_m while also improving linearity; moreover, transistors M3 and M8 are used to further reduce the current that flows into the M4, M7 differential pair, reducing the G_m. The frequency response of the filter is shown in Fig. 6.4.6: a cut-off frequency of about 225 Hz has been achieved. Finally, to accommodate different measurement setups such as the attachment of beads, which have a higher rotation frequency (in the order of 100 to 200 Hz), the cut-off frequency can be changed by changing the OTA G_m through the multiplicity of the transistor M_0, up to 15 kHz.

6.5 Results

The circuits described above have been designed in a TSMC 0.18 µm CMOS process. The complete layout of the chip is shown in Fig. 6.5.1, together with a photograph of the fabricated chip.

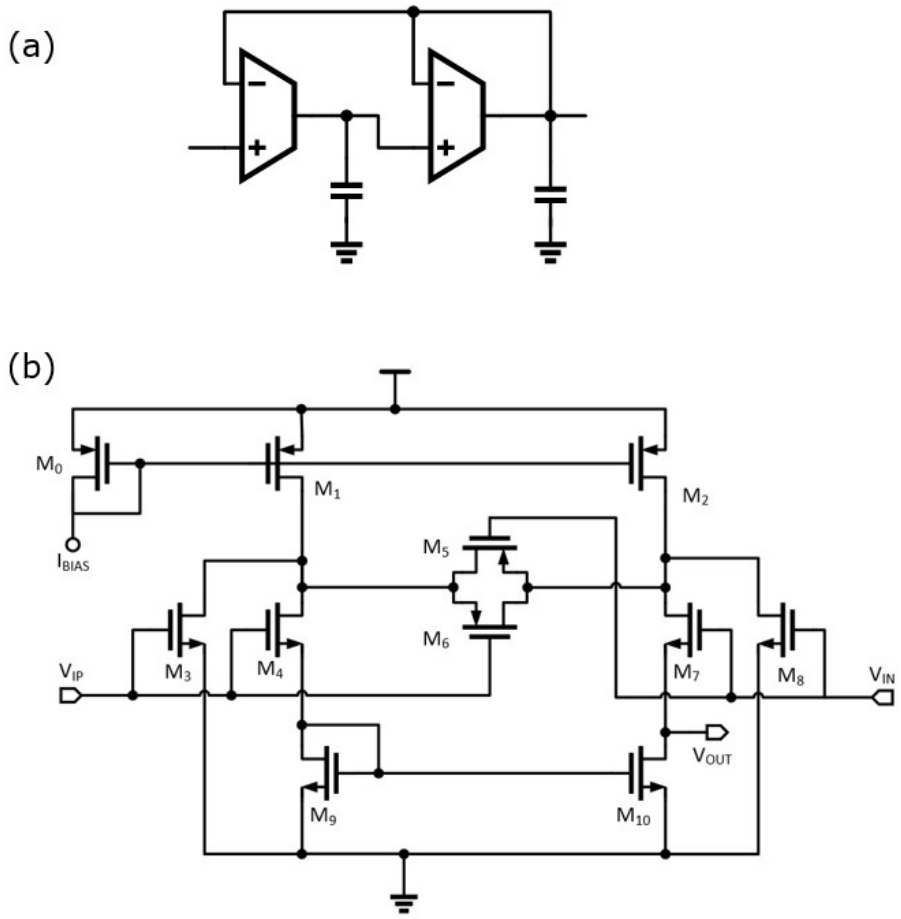

Figure 6.4.5: (a) $G_m - C$ filter block design. (b) Low G_m OTA schematic.

The sensitivity of the chip has been simulated in Cadence Virtuoso Analog Design Environment. For the simulation, the schematic in Fig. 6.5.2 has been used. The entire signal path has been included, and the electrodes have been modeled with their equivalent circuit. The R_{sol} value of one electrode pair has been swept over time and the outputs of the low-pass filter has been recorded.

For example, simulating the electrodes of type A (i.e. a size of $2\,\mu m \times 5\,\mu m$ and $2\,\mu m$ of spacing), the results reported in Fig. 6.5.3 have been obtained. The simulated resistance variation is plotted in orange and the V_X output voltage is plotted in blue. By appropriately setting the current amplifier and TIA gain, is it possible to measure different orders of magnitude of resistance variation. With the 190 dB configuration a variation of a few kΩ can be measured, so it should be possible to detect the activity of a single *E. coli* cell between the electrodes.

Basic functionalities of the fabricated chip have been tested: the outputs react to changes in the input voltages or impedances, but further characterization is currently in progress.

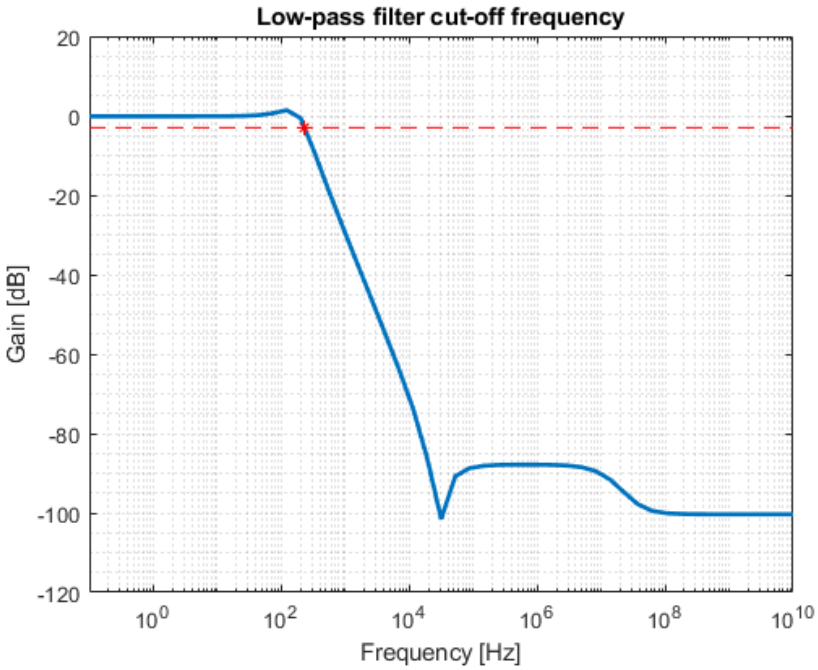

Figure 6.4.6: Low-pass filter frequency response.

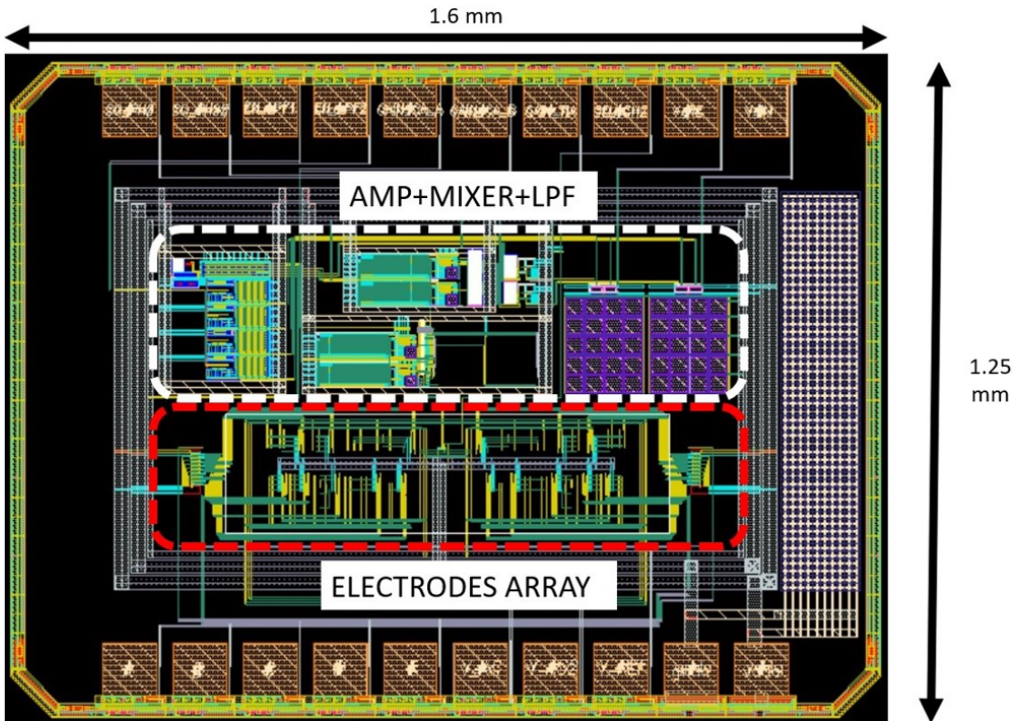

(a)

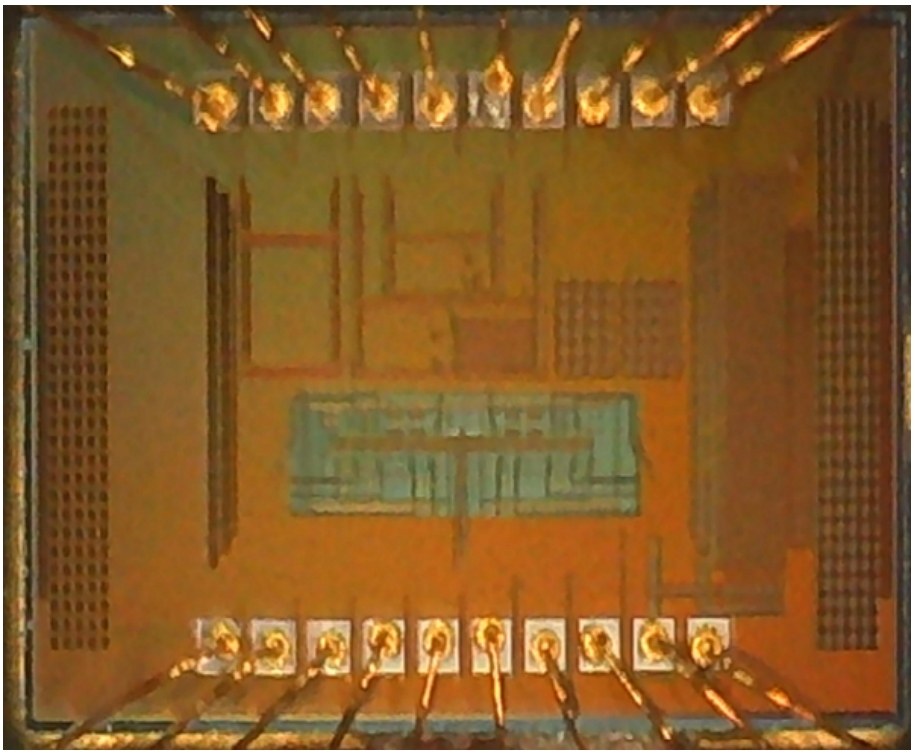

(b)

Figure 6.5.1: (a) Designed layout of the chip. (b) Photograph of the fabricated chip.

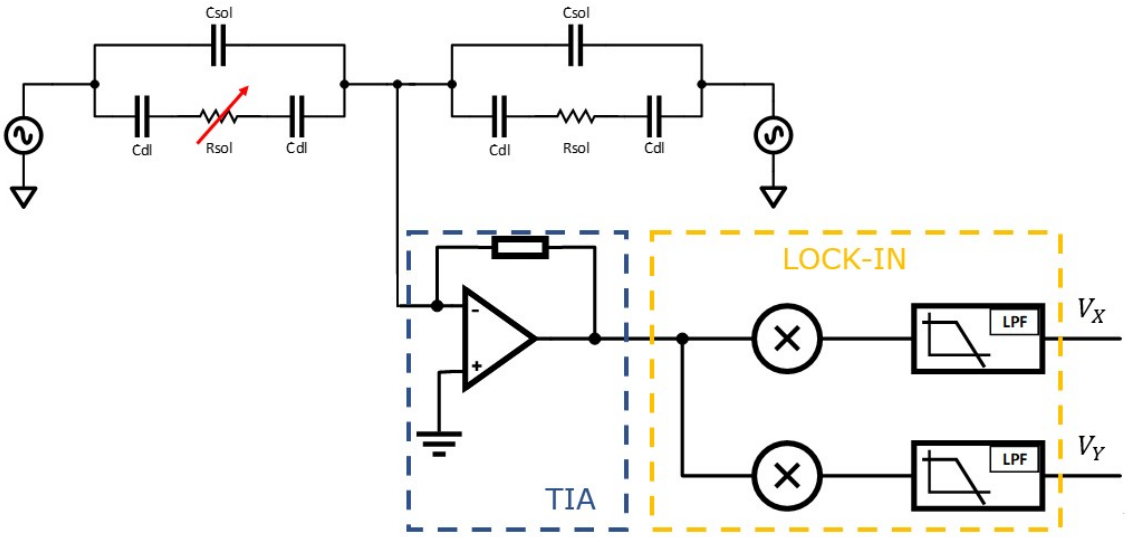

Figure 6.5.2: Simulation schematic. Two electrode pairs have been included, one of which is used as the measurement site, or Z_{DUT}, and has a variable resistance solution. The other electrode pair is used as the reference impedance, or Z_{REF}, to implement a differential measurement so that only the ΔR_{sol} is measured.

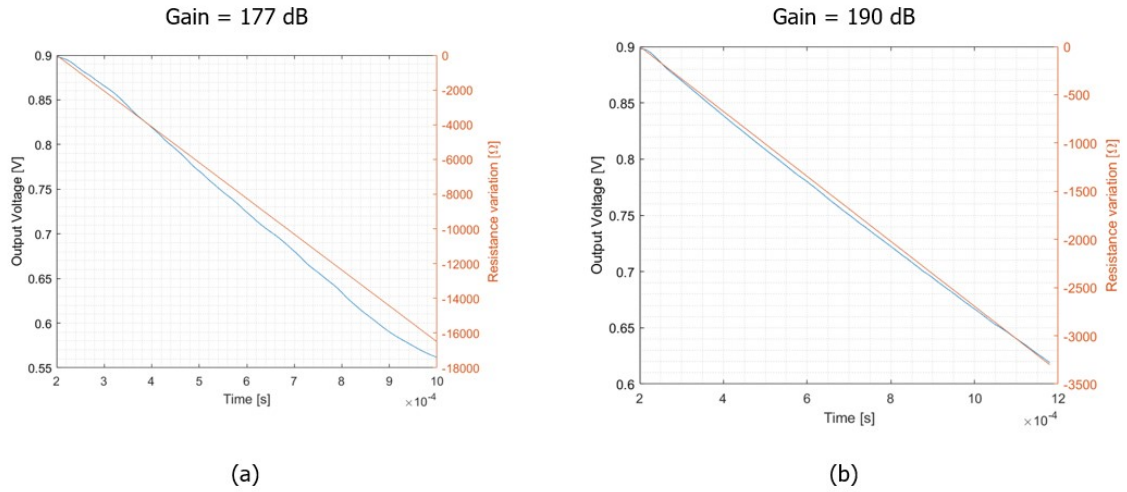

(a) (b)

Figure 6.5.3: (a) Output linear range with 177 dB gain. (b) Output linear range with 190 dB gain.

7 | Conclusions

This work of thesis focused on the development of two CMOS biosensors, one for the detection of telomerase activity and the other to perform bacterial biosensing.

Telomerase detection has demonstrated to be an effective diagnosis and screening method to detect malignant cells, so it is of fundamental importance to have a tool that allows a fast and easy detection of the enzyme. The state of the art of biosensors and telomerase detection presented different approaches that employed optical, electrochemical and electronic detecting methods. This last approach was selected as it offers many advantages over more traditional techniques. In particular, CMOS standard technology was chosen because of its capability to provide a solid, precise and portable biosensor implementation. Among all the FET-based biosensor, CMFET appeared as a promising structure to perform the detection of telomerase activity, thanks to its ability to sense charge variations on the active area. A complete LoC has been designed to detect telomerase presence and activity, which includes the actual biosensor (implemented through a CMFET device) and a set of different readout schemes and circuits that allow a complete measurement of the phenomenon. Post-layout simulations, performed at chip-level, showed that the complete signal path of the LoC, from the sensors to the output, is correctly working; moreover, given that the CMFET working principle has been validated in the past, they represent a good approximation of the expected behaviour. Future work concerns the demonstration of the correct operation by testing the fabricated LoC, to validate the results obtained through the simulations. Furthermore, the possibility to functionalize the sensing areas with electrochemical procedures with the integrated potentiostat can open the way to different applications which are worth looking into, such as performing liquid biopsy or record the electric activity of neural cells.

In the second part, the possibility to employ bacteria as biosensors has been addressed. Thanks to the chemotactic process, bacteria can sense chemicals in their environments with high sensitivity and selectivity, close to an ideal biosensor. Thus, by observing bacteria activity, information about the presence of specific chemicals can be inferred. In order to do this, an chip has been designed to monitor the bacterial flagellar motor rotation, which is related to the chemotactic activity. By tethering bacteria near an electrode pair, the chip can detect the changes in impedance caused by the rotation of the cell itself or a bead attached to the flagellum. A first proof-of-concept chip has been designed and fabricated, and at the time of writing it is being tested to provide an accurate characterization and validate

simulation results. The possibility to monitor the activity of many cells at the same time, with a single cell resolution and in real time, is very attractive; moreover, thanks to multiplexing capabilities and by employing the progresses in molecular biology and genetically engineered microorganisms, complex chemical compositions could be analyzed with a single integrated device.

Bibliography

[1] William R Heineman and William B Jensen. Leland c. clark jr.(1918–2005). *Biosensors and Bioelectronics*, 8(21):1403–1404, 2006.

[2] A. Wilkinson A. D. McNaught. Compendium of chemical terminology, 2nd ed. (the "gold book"). 1997.

[3] MI Pividori, A Merkoci, and S Alegret. Electrochemical genosensor design: immobilisation of oligonucleotides onto transducer surfaces and detection methods. *Biosensors and Bioelectronics*, 15(5-6):291–303, 2000.

[4] Mengsu Yang, Mark E McGovern, and Michael Thompson. Genosensor technology and the detention of interfacial nucleic acid chemistry. *Analytica Chimica Acta*, 346(3):259–275, 1997.

[5] Miri Yemini, Meital Reches, Ehud Gazit, and Judith Rishpon. Peptide nanotube-modified electrodes for enzyme- biosensor applications. *Analytical Chemistry*, 77(16):5155–5159, 2005.

[6] Aoife Morrin, Orawan Ngamna, Anthony J Killard, Simon E Moulton, Malcolm R Smyth, and Gordon G Wallace. An amperometric enzyme biosensor fabricated from polyaniline nanoparticles. *Electroanalysis: An International Journal Devoted to Fundamental and Practical Aspects of Electroanalysis*, 17(5-6):423–430, 2005.

[7] Kristian Helmerson, Rani Kishore, William D Phillips, and Howard H Weetall. Optical tweezers-based immunosensor detects femtomolar concentrations of antigens. *Clinical chemistry*, 43(2):379–383, 1997.

[8] Natalija Backmann, Christian Zahnd, Francois Huber, Alexander Bietsch, Andreas Plückthun, Hans-Peter Lang, Hans-Joachim Güntherodt, Martin Hegner, and Christoph Gerber. A label-free immunosensor array using single-chain antibody fragments. *Proceedings of the National Academy of Sciences*, 102(41):14587–14592, 2005.

[9] Jian-Zhong Sun, Gakai Peter Kingori, Rong-Wei Si, Dan-Dan Zhai, Zhi-Hong Liao, De-Zhen Sun, Tao Zheng, and Yang-Chun Yong. Microbial fuel cell-based biosensors for environmental monitoring: a review. *Water Science and Technology*, 71(6):801–809, 2015.

[10] Juan C Gutiérrez, Francisco Amaro, and Ana Martín-González. Heavy metal whole-cell biosensors using eukaryotic microorganisms: an updated critical review. *Frontiers in microbiology*, 6:48, 2015.

[11] Reiji Okazaki, Tuneko Okazaki, Kiwako Sakabe, Kazunori Sugimoto, and Akio Sugino. Mechanism of dna chain growth. i. possible discontinuity and unusual secondary structure of newly synthesized chains. *Proceedings of the National Academy of Sciences*, 59(2):598–605, 1968.

[12] Carol W Greider and Elizabeth H Blackburn. Identification of a specific telomere terminal transferase activity in tetrahymena extracts. *Cell*, 43(2):405–413, 1985.

[13] Carol W Greider and Elizabeth H Blackburn. A telomeric sequence in the rna of tetrahymena telomerase required for telomere repeat synthesis. *Nature*, 337(6205):331–337, 1989.

[14] Jack W Szostak and Elizabeth H Blackburn. Cloning yeast telomeres on linear plasmid vectors. *Cell*, 29(1):245–255, 1982.

[15] Leonard Hayflick. The limited in vitro lifetime of human diploid cell strains. *Experimental cell research*, 37(3):614–636, 1965.

[16] Scott B Cohen, Mark E Graham, George O Lovrecz, Nicolai Bache, Phillip J Robinson, and Roger R Reddel. Protein composition of catalytically active human telomerase from immortal cells. *Science*, 315(5820):1850–1853, 2007.

[17] Shawn E Holt, Woodring E Wright, and Jerry W Shay. Regulation of telomerase activity in immortal cell lines. *Molecular and cellular biology*, 16(6):2932–2939, 1996.

[18] JW Shay and S Bacchetti. A survey of telomerase activity in human cancer. *European journal of cancer*, 33(5):787–791, 1997.

[19] Nam W Kim, Mieczyslaw A Piatyszek, Karen R Prowse, Calvin B Harley, Michael D West, Peter LC Ho, Gina M Coviello, Woodring E Wright, Scott L Weinrich, and Jerry W Shay. Specific association of human telomerase activity with immortal cells and cancer. *Science*, pages 2011–2015, 1994.

[20] Mariela Jaskelioff, Florian L Muller, Ji-Hye Paik, Emily Thomas, Shan Jiang, Andrew C Adams, Ergun Sahin, Maria Kost-Alimova, Alexei Protopopov, Juan Cadinanos, et al. Telomerase reactivation reverses tissue degeneration in aged telomerase-deficient mice. *Nature*, 469(7328):102–106, 2011.

[21] Richard M Cawthon, Ken R Smith, Elizabeth O'Brien, Anna Sivatchenko, and Richard A Kerber. Association between telomere length in blood and mortality in people aged 60 years or older. *The Lancet*, 361(9355):393–395, 2003.

[22] Erez Eitan, Emmette R Hutchison, and Mark P Mattson. Telomere shortening in neurological disorders: an abundance of unanswered questions. *Trends in neurosciences*, 37(5):256–263, 2014.

[23] Alison Spilsbury, Satomi Miwa, Johannes Attems, and Gabriele Saretzki. The role of telomerase protein tert in alzheimer's disease and in tau-related pathology in vitro. *Journal of Neuroscience*, 35(4):1659–1674, 2015.

[24] Nam W Kim and Fred Wu. Advances in quantification and characterization of telomerase activity by the telomeric repeat amplification protocol (trap). *Nucleic acids research*, 25(13):2595–2597, 1997.

[25] Jiří Fajkus. Detection of telomerase activity by the trap assay and its variants and alternatives. *Clinica chimica acta*, 371(1):25–31, 2006.

[26] Hiroshi Uehara, Glenn Nardone, Irina Nazarenko, and Robert J Hohman. Detection of telomerase activity utilizing energy transfer primers: comparison with gel-and elisa-based detection. *Biotechniques*, 26:552–558, 1999.

[27] Peter T. Kissinger and William R. Heineman. Cyclic voltammetry. *Journal of Chemical Education*, 60(9):702, 1983.

[28] Kazuhiro Tominaga, Mana Hayakawa, Shinobu Sato, Masaaki Kodama, Manabu Habu, and Shigeori Takenaka. Electrochemical telomerase assay for oral cancer screening. In *World Automation Congress (WAC), 2014*, pages 38–42. IEEE, 2014.

[29] Janet G. Osteryoung and Robert A. Osteryoung. Square wave voltammetry. *Analytical Chemistry*, 57(1):101–110, 1985.

[30] Solution ionic strength effect on gold nanoparticle solution color transition. *Talanta*, 69(4):873–876, 2006.

[31] Mohammad Pourhassan-Moghaddam, Nosratollah Zarghami, Afshin Mohsenifar, Mohammad Rahmati-Yamchi, Hadis Daraee, Miguel de la Guardia, and Shahram Ahmadian. Gold nanoprobe-based detection of human telomerase reverse transcriptase (htert) gene expression. *IEEE transactions on nanobioscience*, 14(4):485–490, 2015.

[32] Gengfeng Zheng, Fernando Patolsky, Yi Cui, Wayne U Wang, and Charles M Lieber. Multiplexed electrical detection of cancer markers with nanowire sensor arrays. *Nature biotechnology*, 23(10):1294, 2005.

[33] Yi Cui, Qingqiao Wei, Hongkun Park, and Charles M Lieber. Nanowire nanosensors for highly sensitive and selective detection of biological and chemical species. *science*, 293(5533):1289–1292, 2001.

[34] Robert J Chen, Sarunya Bangsaruntip, Katerina A Drouvalakis, Nadine Wong Shi Kam, Moonsub Shim, Yiming Li, Woong Kim, Paul J Utz, and Hongjie Dai. Noncovalent functionalization of carbon nanotubes for highly

specific electronic biosensors. *Proceedings of the National Academy of Sciences*, 100(9):4984–4989, 2003.

[35] Mauro Ferrari. Cancer nanotechnology: opportunities and challenges. *Nature reviews cancer*, 5(3):161–171, 2005.

[36] Constance I Nugent and Victoria Lundblad. The telomerase reverse transcriptase: components and regulation. *Genes & development*, 12(8):1073–1085, 1998.

[37] Haig Norian, Ioannis Kymissis, and KL Shepard. Integrated cmos quantitative polymerase chain reaction lab-on-chip. In *2013 Symposium on VLSI Circuits*, pages C220–C221. IEEE, 2013.

[38] Junghoon Lee, Hyejin Moon, Jesse Fowler, Thomas Schoellhammer, and Chang-Jin Kim. Electrowetting and electrowetting-on-dielectric for microscale liquid handling. *Sensors and actuators a: Physical*, 95(2-3):259–268, 2002.

[39] Sergio Cova, Massimo Ghioni, Andrea Lacaita, Carlo Samori, and Franco Zappa. Avalanche photodiodes and quenching circuits for single-photon detection. *Applied optics*, 35(12):1956–1976, 1996.

[40] Sung-Yi Yang, Suz-Kai Hsiung, Yung-Ching Hung, Chen-Min Chang, Teh-Lu Liao, and Gwo-Bin Lee. A cell counting/sorting system incorporated with a microfabricated flow cytometer chip. *Measurement Science and Technology*, 17(7):2001, 2006.

[41] Sherrif F Ibrahim and Ger van den Engh. Flow cytometry and cell sorting. *Cell Separation*, pages 19–39, 2007.

[42] Craig A Gedye, Ali Hussain, Joshua Paterson, Alannah Smrke, Harleen Saini, Danylo Sirskyj, Keira Pereira, Nazleen Lobo, Jocelyn Stewart, Christopher Go, et al. Cell surface profiling using high-throughput flow cytometry: a platform for biomarker discovery and analysis of cellular heterogeneity. *PloS one*, 9(8):e105602, 2014.

[43] Marion G Macey and Marion G Macey. *Flow cytometry*. Springer, 2007.

[44] Lee Hartley, Karan VIS Kaler, and Orly Yadid-Pecht. Hybrid integration of an active pixel sensor and microfluidics for cytometry on a chip. *IEEE Transactions on Circuits and Systems I: Regular Papers*, 54(1):99–110, 2007.

[45] Hiroshi Handa, Takafumi Matsushima, Natsumi Nishimoto, Madoka Inoue, Takayuki Saitoh, Akihiko Yokohama, Norifumi Tsukamoto, Takeki Mitsui, Hirotaka Nakahashi, Kotaro Toyama, et al. Flow cytometric detection of human telomerase reverse transcriptase (htert) expression in a subpopulation of bone marrow cells. *Leukemia research*, 34(2):177–183, 2010.

[46] Nicoló Manaresi, Aldo Romani, Gianni Medoro, Luigi Altomare, Andrea Leonardi, Marco Tartagni, and Roberto Guerrieri. A cmos chip for individual

cell manipulation and detection. *IEEE Journal of Solid-State Circuits*, 38(12):2297–2305, 2003.

[47] Martina Viefhues and Ralf Eichhorn. Dna dielectrophoresis: Theory and applications a review. *Electrophoresis*, 2017.

[48] Piet Bergveld. Development of an ion-sensitive solid-state device for neurophysiological measurements. *IEEE Transactions on Biomedical Engineering*, (1):70–71, 1970.

[49] Etery Sharon, Ronit Freeman, Michael Riskin, Noa Gil, Yehuda Tzfati, and Itamar Willner. Optical, electrical and surface plasmon resonance methods for detecting telomerase activity. *Analytical chemistry*, 82(20):8390–8397, 2010.

[50] Massimo Barbaro, Annalisa Bonfiglio, and Luigi Raffo. A charge-modulated fet for detection of biomolecular processes: conception, modeling, and simulation. *IEEE Transactions on Electron Devices*, 53(1):158–166, 2006.

[51] Emil Palek and Miroslav Fojta. Peer reviewed: detecting dna hybridization and damage, 2001.

[52] Massimo Barbaro, Annalisa Bonfiglio, Luigi Raffo, Andrea Alessandrini, Paolo Facci, and Imrich Barák. Fully electronic dna hybridization detection by a standard cmos biochip. *Sensors and Actuators B: Chemical*, 118(1):41–46, 2006.

[53] Massimo Barbaro, Alessandra Caboni, and Daniela Loi. A cmos integrated dna-chip for hybridization detection with digital output. In *Advances in Sensors and Interface, 2007. IWASI 2007. 2nd International Workshop on*, pages 1–5. IEEE, 2007.

[54] Stefano Lai, Alessandra Caboni, Daniela Loi, and Massimo Barbaro. A cmos biocompatible charge detector for biosensing applications. *IEEE Transactions on Electron Devices*, 59(9):2512–2519, 2012.

[55] M Barbaro, A Caboni, D Loi, S Lai, A Homsy, PD Van Der Wal, and NF De Rooij. Label-free, direct dna detection by means of a standard cmos electronic chip. *Sensors and Actuators B: Chemical*, 171:148–154, 2012.

[56] Emily Crowley, Federica Di Nicolantonio, Fotios Loupakis, and Alberto Bardelli. Liquid biopsy: monitoring cancer-genetics in the blood. *Nature reviews Clinical oncology*, 10(8):472, 2013.

[57] Daekyu Sun, Christine C Lopez-Guajardo, James Quada, Laurence H Hurley, and Daniel D Von Hoff. Regulation of catalytic activity and processivity of human telomerase. *Biochemistry*, 38(13):4037–4044, 1999.

[58] Ying-Chuan Liu, Hung-Yu Wang, Yuan-Long Jeang, and Yu-Wei Huang. A cmos current mirror with enhanced input dynamic range. In *2008 3rd International Conference on Innovative Computing Information and Control*, pages 571–571. IEEE, 2008.

[59] H Traff. Novel approach to high speed cmos current comparators. *Electronics Letters*, 28(3):310–312, 1992.

[60] Liang Su, Wenzhao Jia, Changjun Hou, and Yu Lei. Microbial biosensors: a review. *Biosensors and bioelectronics*, 26(5):1788–1799, 2011.

[61] Miso Park, Shen-Long Tsai, and Wilfred Chen. Microbial biosensors: engineered microorganisms as the sensing machinery. *Sensors*, 13(5):5777–5795, 2013.

[62] Ji Won Lim, Dogyeong Ha, Jongwan Lee, Sung Kuk Lee, and Taesung Kim. Review of micro/nanotechnologies for microbial biosensors. *Frontiers in bioengineering and biotechnology*, 3:61, 2015.

[63] Maya Shamir, Yinon Bar-On, Rob Phillips, and Ron Milo. Snapshot: timescales in cell biology. *Cell*, 164(6):1302–1302, 2016.

[64] Da Wang and Carol A Fierke. The baesr regulon is involved in defense against zinc toxicity in e. coli. *Metallomics*, 5(4):372–383, 2013.

[65] Caryn E Outten and Thomas V O'Halloran. Femtomolar sensitivity of metalloregulatory proteins controlling zinc homeostasis. *Science*, 292(5526):2488–2492, 2001.

[66] Judith P Armitage. Three hundred years of bacterial motility. *Foundations of Modern Biochemistry*, 3:107–171, 1997.

[67] Takashi Sagawa, Yu Kikuchi, Yuichi Inoue, Hiroto Takahashi, Takahiro Muraoka, Kazushi Kinbara, Akihiko Ishijima, and Hajime Fukuoka. Single-cell e. coli response to an instantaneously applied chemotactic signal. *Biophysical journal*, 107(3):730–739, 2014.

[68] Hanbin Mao, Paul S Cremer, and Michael D Manson. A sensitive, versatile microfluidic assay for bacterial chemotaxis. *Proceedings of the National Academy of Sciences*, 100(9):5449–5454, 2003.

[69] Howard C Berg and Edward M Purcell. Physics of chemoreception. *Biophysical journal*, 20(2):193–219, 1977.

[70] Howard C Berg. The rotary motor of bacterial flagella. *Annual review of biochemistry*, 72, 2003.

[71] Tohru Minamino and Katsumi Imada. The bacterial flagellar motor and its structural diversity. *Trends in microbiology*, 23(5):267–274, 2015.

[72] Stuart W Reid, Mark C Leake, Jennifer H Chandler, Chien-Jung Lo, Judith P Armitage, and Richard M Berry. The maximum number of torque-generating units in the flagellar motor of escherichia coli is at least 11. *Proceedings of the National Academy of Sciences*, 103(21):8066–8071, 2006.

[73] Yoshiyuki Sowa and Richard M Berry. Bacterial flagellar motor. *Quarterly reviews of biophysics*, 41(2):103–132, 2008.

[74] Patrick J Mears, Santosh Koirala, Chris V Rao, Ido Golding, and Yann R Chemla. Escherichia coli swimming is robust against variations in flagellar number. *Elife*, 3:e01916, 2014.

[75] Steven M Block, Jeffrey E Segall, and Howard C Berg. Impulse responses in bacterial chemotaxis. *Cell*, 31(1):215–226, 1982.

[76] Thorsten W Grebe and Jeff Stock. Bacterial chemotaxis: the five sensors of a bacterium. *Current Biology*, 8(5):R154–R157, 1998.

[77] Robert M Macnab and Daniel E Koshland. The gradient-sensing mechanism in bacterial chemotaxis. *Proceedings of the National Academy of Sciences*, 69(9):2509–2512, 1972.

[78] Martin S Springer, Michael F Goy, and Julius Adler. Protein methylation in behavioural control mechanisms and in signal transduction. *Nature*, 280(5720):279–284, 1979.

[79] Gerald L Hazelbauer, Joseph J Falke, and John S Parkinson. Bacterial chemoreceptors: high-performance signaling in networked arrays. *Trends in biochemical sciences*, 33(1):9–19, 2008.

[80] Julius Adler. A method for measuring chemotaxis and use of the method to determine optimum conditions for chemotaxis by escherichia coli. *Microbiology*, 74(1):77–91, 1973.

[81] Th W Engelmann. Neue methode zur untersuchung der sauerstoffausscheidung pflanzlicher und thierischer organismen. *Archiv für die gesamte Physiologie des Menschen und der Tiere*, 25(1):285–292, 1881.

[82] Gerald L Hazelbauer, Robert E Mesibov, and Julius Adler. Escherichia coli mutants defective in chemotaxis toward specific chemicals. *Proceedings of the National Academy of Sciences*, 64(4):1300–1307, 1969.

[83] Russell Bainer, Heungwon Park, and Philippe Cluzel. A high-throughput capillary assay for bacterial chemotaxis. *Journal of microbiological methods*, 55(1):315–319, 2003.

[84] Yevgeniy Kalinin, Silke Neumann, Victor Sourjik, and Mingming Wu. Responses of escherichia coli bacteria to two opposing chemoattractant gradients depend on the chemoreceptor ratio. *Journal of Bacteriology*, 192(7):1796–1800, 2010.

[85] Michael Silverman and Melvin Simon. Flagellar rotation and the mechanism of bacterial motility. *Nature*, 249(5452):73–74, 1974.

[86] Goro Kuwajima. Construction of a minimum-size functional flagellin of escherichia coli. *Journal of bacteriology*, 170(7):3305–3309, 1988.

[87] Michael Eisenbach, Amnon Wolf, Martin Welch, S Roy Caplan, I Richard Lapidus, Robert M Macnab, Hamutal Aloni, and Ora Asher. Pausing, switching and speed fluctuation of the bacterial flagellar motor and their relation to motility and chemotaxis. *Journal of molecular biology*, 211(3):551–563, 1990.

[88] Tom J Zajdel, Andrew Nam, Jove Yuan, Vikram R Shirsat, Behzad Rad, and Michel M Maharbiz. Applying machine learning to the flagellar motor for biosensing. In *2018 40th Annual International Conference of the IEEE Engineering in Medicine and Biology Society (EMBC)*, pages 1–4. IEEE, 2018.

[89] Diana Clausznitzer, Gabriele Micali, Silke Neumann, Victor Sourjik, and Robert G Endres. Predicting chemical environments of bacteria from receptor signaling. *PLoS Comput Biol*, 10(10):e1003870, 2014.

[90] Jean-Baptiste Masson, Guillaume Voisinne, Jerome Wong-Ng, Antonio Celani, and Massimo Vergassola. Noninvasive inference of the molecular chemotactic response using bacterial trajectories. *Proceedings of the National Academy of Sciences*, 109(5):1802–1807, 2012.

[91] Tom J Zajdel, Alexander N Walczak, Debleena Sengupta, Victor Tieu, Behzad Rad, and Michel M Maharbiz. Towards a biohybrid sensing platform built on impedance-based bacterial flagellar motor tachometry. In *2017 IEEE Biomedical Circuits and Systems Conference (BioCAS)*, pages 1–4. IEEE, 2017.

[92] H Helmholtz. Ueber einige gesetze der verteilung elektrischer ströme in körperlichen leitern, mit anwendung auf die thierisch elektrischen versuche. *Ann. phys. Chem.*, 3(29):353–377, 1853.

[93] M Gouy. Sur la constitution de la charge électrique à la surface d'un électrolyte. 1910.

[94] David Leonard Chapman. Li. a contribution to the theory of electrocapillarity. *The London, Edinburgh, and Dublin philosophical magazine and journal of science*, 25(148):475–481, 1913.

[95] Shady Gawad, Laurent Schild, and PH Renaud. Micromachined impedance spectroscopy flow cytometer for cell analysis and particle sizing. *Lab on a Chip*, 1(1):76–82, 2001.

[96] Jongin Hong, Dae Sung Yoon, Sung Kwan Kim, Tae Song Kim, Sanghyo Kim, Eugene Y Pak, and Kwangsoo No. Ac frequency characteristics of coplanar impedance sensors as design parameters. *Lab on a Chip*, 5(3):270–279, 2005.

[97] Keysight Technologies. Impedance measurement handbook, Jul 2020.

[98] Herman P Schwan. Electrical properties of tissue and cell suspensions. In *Advances in biological and medical physics*, volume 5, pages 147–209. Elsevier, 1957.

[99] Wei Bai, KS Zhao, and K Asami. Dielectric properties of e. coli cell as simulated by the three-shell spheroidal model. *Biophysical chemistry*, 122(2):136–142, 2006.

[100] von H Pauly and HP Schwan. Über die impedanz einer suspension von kugelförmigen teilchen mit einer schale: Ein modell für das dielektrische verhalten von zellsuspensionen und von proteinlösungen. *Zeitschrift für Naturforschung B*, 14(2):125–131, 1959.

[101] RA Hoffman and WB Britt. Flow-system measurement of cell impedance properties. *Journal of Histochemistry & Cytochemistry*, 27(1):234–240, 1979.

[102] Koji Asami, Tetsuya Hanai, and Naokazu Koizumi. Dielectric analysis of escherichia coli suspensions in the light of the theory of interfacial polarization. *Biophysical journal*, 31(2):215–228, 1980.

[103] Pontus Linderholm, Thomas Braschler, Jeanne Vannod, Yann Barrandon, Michel Brouard, and Philippe Renaud. Two-dimensional impedance imaging of cell migration and epithelial stratification. *Lab on a Chip*, 6(9):1155–1162, 2006.

[104] Pontus Linderholm and Philippe Renaud. Comment on "ac frequency characteristics of coplanar impedance sensors as design parameters" by jongin hong, dae sung yoon, sung kwan kim, tae song kim, sanghyo kim, eugene y. pak and kwangsoo no, lab chip, 2005, 5, 270. *Lab on a Chip*, 5(12):1416–1417, 2005.

[105] Giorgio Ferrari, Marco Farina, Filippo Guagliardo, Marco Carminati, and Marco Sampietro. Ultra-low-noise cmos current preamplifier from dc to 1 mhz. *Electronics letters*, 45(25):1278–1280, 2009.

[106] Carmine Ciofi, Felice Crupi, Calogero Pace, and Graziella Scandurra. How to enlarge the bandwidth without increasing the noise in op-amp-based transimpedance amplifier. *IEEE transactions on instrumentation and measurement*, 55(3):814–819, 2006.

[107] CR Cosens. A balance-detector for alternating-current bridges. *Proceedings of the physical society*, 46(6):818, 1934.

[108] Walter C Michels and Norma L Curtis. A pentode lock-in amplifier of high frequency selectivity. *Review of Scientific Instruments*, 12(9):444–447, 1941.

[109] Haidong Liu, Xiaohong Peng, and Wuchen Wu. Design of a gm-c low pass filter with low cutoff frequency. In *2009 Asia Pacific Conference on Postgraduate Research in Microelectronics & Electronics (PrimeAsia)*, pages 125–128. IEEE, 2009.